Ab-initio calculations of the vanadium ladder structures NaV_2O_5, CaV_2O_5, and MgV_2O_5

Jürgen Spitaler

Januar 2006
Institut für Physik, Karl–Franzens–Universität Graz

Doktorarbeit
zur Erlangung des akademischen Grades eines Doktors
an der Naturwissenschaftlichen Fakultät der
Karl–Franzens–Universität Graz
betreut von
Prof. Dr. Claudia Ambrosch-Draxl

To Elisabeth

Contents

1. Introduction

1.1. Overview

Vanadium ladder compounds have been a subject of great interest in the past ten years of solid state physics. They belong to the very active research area of complex materials with low-dimensional features, where charge, spin and lattice degrees of freedom strongly interact and lead to extraordinary physical properties [1, 2, 3, 4, 5]. In the following, the main features of sodium, calcium and magnesium vanadate will be presented.

The common structural element of NaV_2O_5, CaV_2O_5, and MgV_2O_5 are two-dimensional planes of V–O ladders. The rungs and legs of these ladders provide the possibility for a hopping of electrons, while the hopping probability between two different ladders is smaller. The upper valence bands of the three compounds are formed by vanadium d_{xy} states, with a small admixture of oxygen $2p$ orbitals.

Let us first focus on NaV_2O_5. In this material, one V d_{xy} electron is shared by the two V atoms of one rung, such that it has quarter-filled character. Nevertheless, NaV_2O_5 turns out to be a dielectric, since the formation of a doubly occupied and an empty rung, which would be the consequence of a hopping along the ladder, costs more energy than it is provided by the related hopping matrix element. NaV_2O_5 attracted special attention after the discovery of the transition to a spin-gapped state at $T_c \approx 35$ K. This phase transition was first detected in magnetic susceptibility measurements [6] and Raman spectra [7]. It is in some aspects analogous to the spin-Peierls transition in $CuGeO_3$ at $T_{SP} = 13.5$ K [8], but differs from the latter by the fact that, in addition to spin and lattice, also the charge distribution of the system is affected. In the low-temperature phase, ions are displaced from their original positions by distances of the order of 0.05 Å. These displacements have been observed in x-ray diffraction [9, 10, 11, 12, 13, 14] and can be estimated from infrared [15] and Raman spectroscopy [16]. They stabilize a phase containing zig-zag charge-ordering patterns ([17, 18] and [10, 12, 13, 14, 19, 20]). Simultaneously, near T_c strong charge fluctuations occur which are induced by dynamical phonons. As a consequence, the spin-spin exchange J is altered [21]. Moreover, electron spin-resonance experiments [22] reveal that the ordering—even at low T—is not static, but influenced by lattice vibrations.

Surprisingly, the dielectric function changes only little when passing T_c [23], while the Raman spectra exhibit large alterations in the electronic background [16]

and show many new peaks, which have either magnetic or phononic origin. The same situation is found in infrared measurements for $T<T_c$. However, a full understanding of these modes is still lacking.

The second vanadium compound, CaV_2O_5, has the same crystal structure as NaV_2O_5 [24], but differs from the sodium structure due to its electronic configuration. The calcium ion contributes one additional electron to the valence bands, such that each vanadium site carries spin 1/2. This implicates that CaV_2O_5 can be described by the generalized Heisenberg model of the spin-spin interaction. One remarkable feature of CaV_2O_5 is the fact that it appears in a spin singlet state with a gap of 500 K (0.05 eV) [25]. The reason for the large gap is the difference in the exchange along the legs and the rungs, respectively, which makes CaV_2O_5 a system of weakly coupled dimers, with strong interaction inside the dimer [26, 27]. The on-site energies and the hopping matrix elements influence the band structure and, thus, indirectly determine the spin-spin exchange parameters. Consequently, they also affect the strength of the spin-phonon coupling.

The third considered material is MgV_2O_5, which is chemically equivalent to CaV_2O_5, but slightly differs from a structural point of view [28]: The x-y planes formed by the V–O ladders are the same as in NaV_2O_5 and CaV_2O_5, but going from one layer to the next in z direction, the ladders are shifted by $b/2$. Thus, a different stacking of the ladder plane results. As in CaV_2O_5, a spin singlet state is found in the magnesium compound. But in contrast to the former, the gap is much smaller, namely 15 K [29, 30], which is due to the fact that in MgV_2O_5 the exchange coupling along the leg and along one rung are of comparable strength [26].

A variety of experimental techniques has been used to study the vanadium ladder compounds. They include magnetic susceptibility measurements [6, 31], x-ray diffraction [9, 11, 13, 24, 28, 32], neutron scattering [33, 34, 35], Raman and infrared measurements [16, 36, 37, 38, 39], optical absorption and reflection [23, 40, 41, 42, 43, 44, 45], V NMR [46, 47, 48, 49] and Na NMR [48, 49, 50, 51], electron-spin resonance [22, 52, 53, 54], electron-paramagnetic resonance [55] and thermal conductivity measurements [56].

1.2. Aims

A first aim of this thesis is to provide a comprehensive insight into the physical nature of NaV_2O_5, CaV_2O_5, and MgV_2O_5 by calculating a large variety of structural, electronic, phononic and optical properties *ab initio*. The lattice geometry, electronic structure and optical properties of all three vanadates are studied in detail, taking into account effects due to the theoretical relaxation of the atomic positions. The results for the three cases are compared to each other.

A second aim is to investigate the effects of lattice distortions. To do so, the complete number of Γ point phonons is calculated and each eigenmode is carefully

analyzed in terms of frequency and eigenvectors. In a second step, phonons and optical calculations are combined to obtain theoretical Raman spectra, which facilitate the understanding of measured results and contain information about the interplay of electrons and phonons.

The third task is to study the interplay of the lattice with electrons and spins. This is achieved by determining the change in the electronic structure for atomic distortions according to the obtained phonon eigenmodes, which lead to changes in the charge transfer gap and in the hopping matrix elements.

The last goal is to tackle some of the open questions with regard to the low-temperature phase of NaV_2O_5. In this context, the electric field gradients for several candidates of the low-temperature structure are calculated ab initio and compared to experimental data. Moreover, the atomic positions for the two low-temperature space groups proposed in literature are relaxed, and the calculated total energies of several structures are compared to each other.

2. Crystal Structures and Symmetry

2.1. CaV_2O_5 and NaV_2O_5 ($T > T_c$)

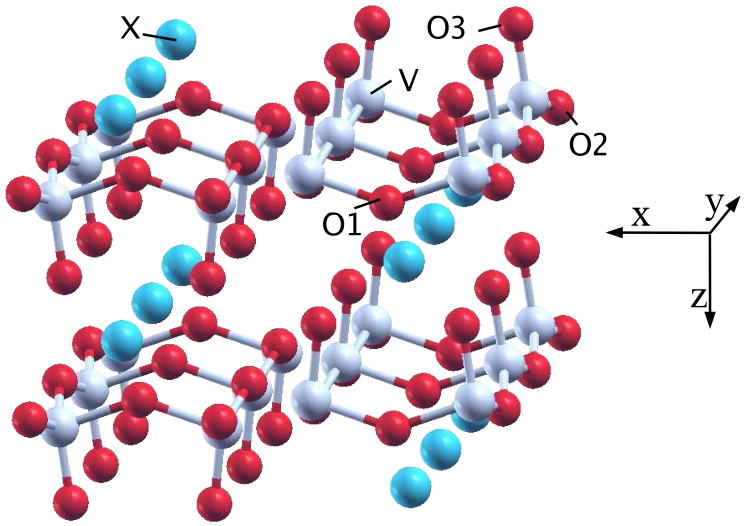

Figure 2.1.: Crystal structure of NaV_2O_5 (high temperature phase) and CaV_2O_5 from a slant perspective. The figure displays four V–O ladders in two different ladder planes. X denotes the metal atom (Na/Ca).

The crystal structure of NaV_2O_5[1] and CaV_2O_5 is presented in Fig. 2.1 from a slant perspective and in Fig. 2.2 as a projection onto the x–z and x–y plane, respectively. Structural data obtained from X-ray scattering are found in Refs. [32, 57, 58] for NaV_2O_5 and in Ref. [24] for CaV_2O_5. In order to be consistent with the nomenclature of NaV_2O_5 used in Ref. [32], we label the in-rung oxygen as "O1" and the apex oxygen as "O3", thus swapping the labeling used for CaV_2O_5 in Ref. [24]. Both compounds crystallize in the orthorhombic space group $Pmmn$ (no. 59), and in both cases, the unit cell contains 16 atoms, where 5 of them are non-equivalent. Also the size of both unit cells is very similar, but slightly larger in CaV_2O_5 (200.2 Å^3 compared to 196.0 Å^3 in NaV_2O_5). The increased unit-cell volume of the Ca compound compared to the Na structure is mainly due to the

[1] Throughout the thesis, if not specially mentioned otherwise, "NaV_2O_5" will always refer to the room temperature structure of sodium vanadate

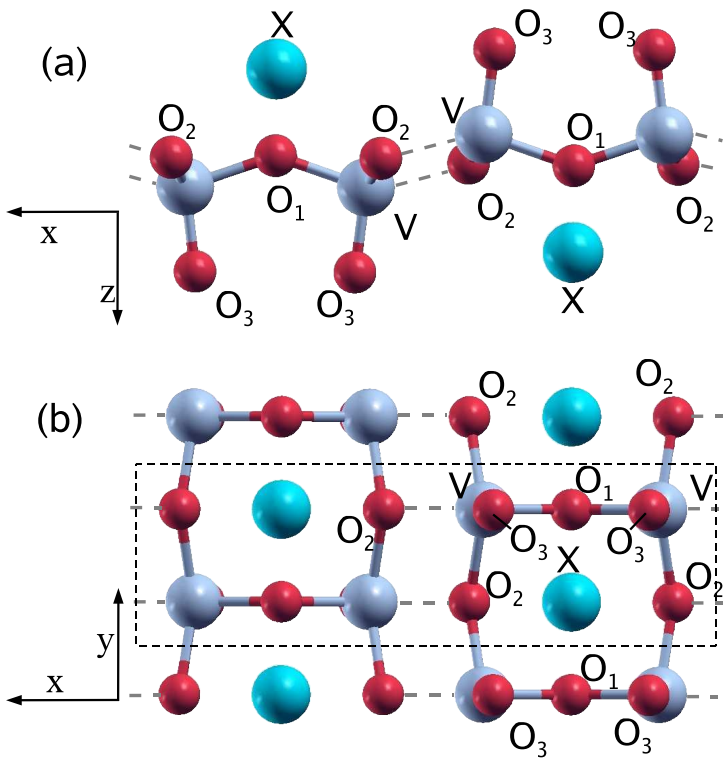

Figure 2.2.: Crystal structure of NaV_2O_5 (high temperature phase) and CaV_2O_5 in the x–z plane (a) and the x–y plane (b). X denotes the metal atoms (Na/Ca). Panel (a) shows exactly one unit cell, while the unit cell in panel (b) is marked by a dashed rectangle. In panel (a), the position of the apex oxygen vertically above/below the V sites, and also the slight kink of the V–O1–V rungs, can clearly be seen. Moreover, it shows the "detached" location of the metal ion, situated away from the ladder plane. Panel (b), in turn, highlights the ladder-like arrangement of V, O1, and O2.

larger size of c, the lattice constant in stacking direction, while a hardly differs and b is even slightly smaller. There is only one kind of V sites, which has Wyckoff position $4f$, and consequently there are four equivalent sites. The same site symmetry is found for the in-leg oxygen O2 and the apex oxygen O3. The metal atom (Na/Ca) and the in-rung oxygen O1 have the twofold Wyckoff position $2b$ and $2a$, respectively, and accordingly appear only twice in each unit cell.

As can be seen in panel (b) of Fig. 2.2, V, O1 and O2 are arranged in the forms of ladders in the x–y plane, where the rungs are built up by V–O1–V bonds ($\parallel x$) and the legs by V-O2 chains ($\parallel y$). The oxygen atom closest to V, however, is the apex oxygen O3, which is located right above (below) the vanadium site. The vanadium atoms can also be considered as being included in pyramids of oxygen atoms, where the two neighboring O2 atoms on the same leg, the next nearest

O2 from the adjacent leg, and the in-rung oxygen O1 form the basal plane, and O3 represents the apex. The metal atom Na (Ca), on the other hand, is centered between two rungs of one ladder, but is situated away from the ladder plane in z direction (panels (b,c)). As rods indicate in the figures, the strongest bonds are found between V and O3, along the V–O1–V rungs and along the legs of the ladders, while the interaction between the vanadium atoms V and the in-leg oxygens O2 from neighboring ladders (indicated by a dashed grey line) is considerably weaker. The metal ions, in turn, which are located in between two ladder planes, are rather loosely bound to the rest of the crystal.

The strength of the bonds is also reflected in the bond lengths between the different atoms. The shortest interatomic distance is found between V and the the apex oxygen O3 (1.614 Å in NaV_2O_5 and 1.645 Å in CaV_2O_5). The next larger distance is encountered between V and the in-rung oxygen O3, which is 1.826 Å in the sodium and 1.905 Å in the calcium compound. The larger V–O1 distance in CaV_2O_5 is due to the smaller angle between the two O1–V bonds in the latter. In detail, the V–O1–V angle is 133° in CaV_2O_5, but 142° in NaV_2O_5. Since this implies a shift of O1 in z direction, the distance between O1 and Ca is smaller than the one between O1 and Na in the other compound. Also the inter-ladder distance, i.e. the distance between the V atom on the leg of one ladder and the O2 with the same y coordinate on the leg of the neighboring ladder (indicated by grey dashed lines in Fig. 2.2), is smaller in CaV_2O_5. A selection of interatomic distances together with the lattice constants is presented in Table 2.1.

2.2. MgV_2O_5

In order to be consistent with the nomenclature used for NaV_2O_5, we refer to the in-rung oxygen as O1 and to the apex oxygen as O3, thus again swapping the labels with respect to the reference providing the structural data (Ref. [28]). Moreover, the coordinate system is chosen to agree with the one used for the other vanadium structures, which deviates from the orientation in Ref. [28], where x refers to the direction parallel to the legs, y to the stacking direction and z is parallel to the rungs of the ladders.

The crystal structure of MgV_2O_5 (Ref. [28]) is very similar to the one of CaV_2O_5 and NaV_2O_5. Actually, considering one V–O oxygen layer of MgV_2O_5 together with the Mg atom in between the rungs, exactly the same geometry as in the other two vanadates is found. But contrary to the other two compounds, in z direction the crystal does not only contain one ladder plane, but has a period twice as large, i.e. c is about two times larger than in NaV_2O_5 and CaV_2O_5 (Tab. 2.1). This is due to the fact that, going from one x–y plane to the next in z direction, the ladders of the next plane are shifted by $b/2$ with respect to the ladders of the original plane (see Fig. 2.4). As a consequence, the Mg atom located in the center of two rungs with respect to one ladder lies in the same x–z

Lattice constants

	NaV_2O_5	CaV_2O_5	MgV_2O_5
a	11.32	11.35	11.02
b	3.61	3.60	3.692
c	4.78	4.89	9.97 ($= 2 \times 4.99$)
vol (Å^3)	196.0	200.2	405.60 ($= 2 \times 202.8$)

Atomic positions

	NaV_2O_5	CaV_2O_5	MgV_2O_5
	(x (a) , y (b) , z (c))	(x (a) , y (b) , z (c))	(x (a) , y (b) , z (c))
V	(0.0979, 0.25, 0.3929)	(0.0961, 0.25, 0.3906)	(0.0970, 0.25, 0.2019)
Na,Ca,Mg	(0.25 , 0.75, 0.1407)	(0.25 , 0.75, 0.1559)	(0.25 , 0.75, 0.1132)
O1	(0.25 , 0.25, 0.5193)	(0.25 , 0.25, 0.5461)	(0.25 , 0.25, 0.3044)
O2	(0.0731, 0.75, 0.5123)	(0.0755, 0.75, 0.5344)	(0.0795, 0.25, 0.7642)
O3	(0.1146, 0.25, 0.0578)	(0.1228, 0.25, 0.0602)	(0.1275, 0.25, 0.0432)

Bond lengths and angles

	NaV_2O_5	CaV_2O_5	MgV_2O_5
V–O3	1.62	1.64	1.62
V–O1	1.82	1.91	1.97
V–O2 ($\|$y)	1.91	1.95	1.96
V–O2 ($\|$x)	2.01	1.98	1.97
O1–X	2.43	2.32	2.02
O2–X	2.60	2.49	2.24
O3–X	2.55	2.54	2.06
$\angle$ (V,O1,V)	142 $^\circ$	133 $^\circ$	118 $^\circ$

Table 2.1.: Structural data for NaV_2O_5 ($T>T_c$), CaV_2O_5 and MgV_2O_5 corresponding to the experimental data of Refs. [32], [24], and [28], respectively. The atomic positions are given in terms of the lattice constants a,b, and c, where c of MgV_2O_5 is about two times larger than the one of NaV_2O_5 and CaV_2O_5, and refer to the atom of each species with the smallest x coordinate. X denotes the metal ion Na, Ca, or Mg, respectively.

plane as the apex oxygens of the neighboring ladder, as it is indicated by the dashed triangle in Fig. 2.3.

Due to the changed stacking, the space group of MgV_2O_5 is not *Pmmn* anymore, but *Cmcm* (no. 63). The symmetry operations of this new space group include the same rotations, while the corresponding shifts are different. Moreover, an additional translation by (0, 1/2, 1/2) is found. The altered space group

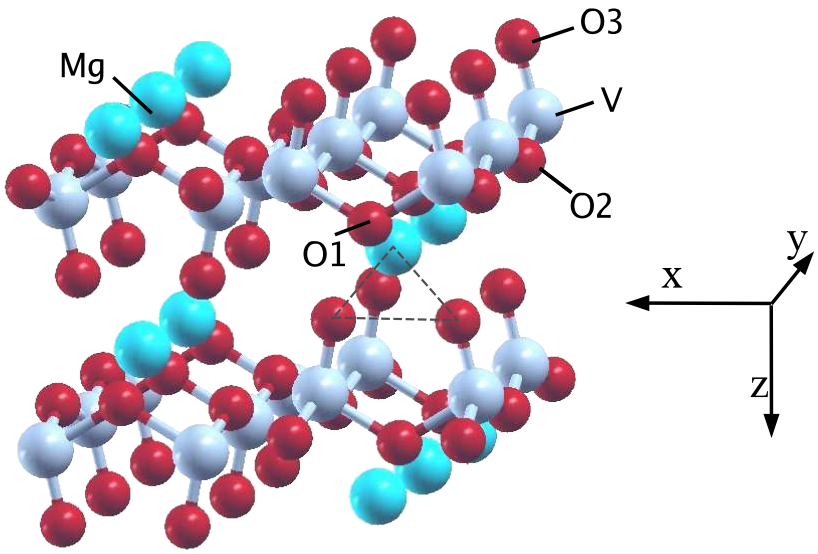

Figure 2.3.: Crystal structure of MgV_2O_5 from a slant perspective. The triangle indicates the x–z plane that includes both the Mg atom of the upper layer and the two apex oxygens O3 of the lower layer. The arrangement of atoms within one ladder plane is the same as in NaV_2O_5 and CaV_2O_5 (Fig. 2.2).

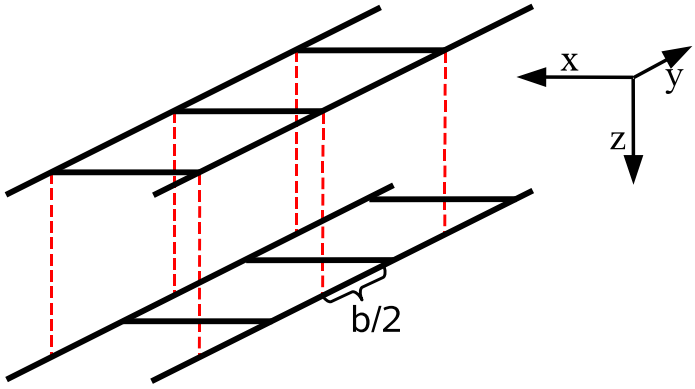

Figure 2.4.: Sketch of the stacking of MgV_2O_5 in z direction. The dashed lines indicate the shift by b/2 going from one ladder plane to the next in z direction.

is also reflected in terms of the Wyckoff positions: While V, O2, and O3 have site symmetry $8f$ in the magnesium compound, both, Mg and the in-rung oxygen O2, have site symmetry $4c$. In space group $Cmcm$ the primitive cell does not coincide with the conventional cell, which comprises 32 atoms, but it contains only half of them, which is the same number of atoms as found in the unit cell of NaV_2O_5 and CaV_2O_5.

Since Mg and the apex oxygens O3 of the next layer are located in the same $y = const$ plane, the distance between them (2.06 Å) is drastically reduced, i.e. it is about 20% shorter than in NaV_2O_5 and CaV_2O_5. In fact it hardly differs from the distance between Mg and its nearest neighbor, the in-leg oxygen O1, which is 2.02 Å. Comparing the geometry within *one layer* with the one found in NaV_2O_5 (CaV_2O_5), the most striking difference is found in the smaller V–O1–V angle due to a larger difference in the z components of V and O1, which leads to a noticeably increased V–O1 distance. On the other hand, Mg is closer to the ladder plane in MgV_2O_5, thus leading to a *decreased* distance between the metal ion and O2 (2.24 Å) compared to the other to vanadates (≈2.55 Å). Comparing the two different V–O2 distances and the distance from V to the apex oxygen, finally, they are quite similar to the ones in NaV_2O_5 and CaV_2O_5: While V–O3 coincides with the one in NaV_2O_5, the V–O2 distances along the leg and to the O2 of the neighboring ladder, respectively, are the same as in CaV_2O_5.

2.3. Structure relaxation

Atom	NaV_2O_5, T>T_c			CaV_2O_5			MgV_2O_5		
	Δx	Δy	Δz	Δx	Δy	Δz	Δx	Δy	Δz
V	0.006	0.000	-0.003	0.020	0.000	-0.008	-0.075	0.000	0.179
X	0.000	0.000	0.004	0.000	0.000	0.016	0.000	0.000	0.174
O1	0.000	0.000	-0.013	0.000	0.000	-0.100	0.000	0.000	0.158
O2	0.008	0.000	-0.024	-0.028	0.000	-0.043	0.086	0.000	0.167
O3	0.022	0.000	-0.005	0.024	0.000	-0.036	-0.006	0.000	0.185

Table 2.2.: Shifts (Å) of the atoms from the experimental to the relaxed structure due to relaxation of the atomic position. X refers to the metal ion Na, Ca, or Mg, respectively. For each species of atoms, the shift refers to the position presented in Tab 2.1

For all three structures a relaxation of the atomic positions, starting from the experimental ones, has been performed. The relaxation procedure works the following way: Using the force acting on each atom obtained for the starting structure, the atoms are shifted in direction of this force and thus a new structure is obtained. Computing the electron distribution of this second system new forces result, which—together with the first forces and coordinates—are used to move the atoms to a third position, etc. This way, the atoms are moved until the forces on all atoms are smaller than a certain convergence limit, thereby minimizing the total energy of the system. Details of the procedure can be found in Ref. [59].

Table 2.2 shows the shifts of the atoms due to relaxation of the atomic positions starting from the experimental structures. For each species of atoms, the

reported shift refers to the position presented in Tab. 2.1. In NaV_2O_5 rather small displacements are found. While the shifts for V and Na are even less than 0.01 Å, the in-rung oxygen O1 is slightly shifted in -z direction thus making the V–O1–V angle somewhat more flat. Also the in-leg oxygen O2 is shifted in -z direction, such that the kinks of the legs are flattened out to some extent. The two apex oxygens O3 of one rung, on their part, get closer to each other by changing their x coordinate.

The atom shifts found in CaV_2O_5 are in general larger than the ones of the sodium compound. The V atom is shifted in x direction by 0.02 Å, which results in a smaller length of the rungs. Moreover, the in-rung oxygen O1 is noticeably shifted in $-z$ direction, which means that the originally rather small V–O1–V angle is considerably increased, namely from 133° to 137°. A comparably pronounced shift in $-z$ direction is also exhibited by the in-leg oxygen O2, which moreover is moved away from the center of the ladder. This has the effect, that the kink of the leg is rotated from the z direction to the x direction. As for NaV_2O_5, in each pair of apex oxygens the two atoms again approach each other, while the V–O3 bonds are additionally stretched in $-z$ direction by about 0.03 Å.

The most dramatic changes are, however, encountered in MgV_2O_5. In general, all atoms listed in Table 2.2 are moved in $+z$ direction by more than 0.15 Å, which implies that both ladders of one unit cell are moved towards the center of the cell. As a consequence, the distance between the legs of the neighboring ladders (V–O2 $\parallel x$) is reduced by 0.02 Å. The z shift of the in-rung oxygen O1 is 0.02 Å smaller compared to the displacements of the V atoms, which has the consequence that also in this compound the V–O1–V angle gets more flat. On the other hand, the V atoms are considerably moved away from the center of the ladder in $-x$ direction ($\Delta x = -0.075$ Å), such that the V–O1 distance is increased by 0.06 Å. In other words, the rungs of the ladders are stretched. Concerning the legs of the ladder, O2 moves in opposite direction parallel to a compared to V, while the difference of V and O2 in terms of the z coordinate is reduced. Hence, the kinks of the legs are another time flattened out, and consequently the V–O2 distanced is reduced by about 0.02 Å.

2.4. Factor group analysis

A factor group analysis for the Wyckoff positions $4f$ (V, O2, O3), $2b$ (Na/Ca) and $2a$ at $\vec{q} = 0$ (Γ point phonons) yields the symmetry coordinates contributing for each irreducible representation. Since there are 16 atoms in one unit cell, there must be 45 optical phonons. The three acoustical phonons, one in B_{1u}, one in B_{2u}, and one in B_{3u} symmetry, at the Γ point represent translations of the whole crystal.

The space group of MgV_2O_5 (no. 63, *Cmcm*) is different from the one of NaV_2O_5 and CaV_2O_5. Nevertheless both, the number of symmetry operations

Irrep	Wyckoff position	symmetry coordinate
A_g modes:	$4f$ $(8f)$	$Q_1 = x(F_1) - x(F_2) - x(F_3) + x(F_4)$
		$Q_2 = z(F_1) + z(F_2) - z(F_3) - z(F_4)$
	$2a, 2b$ $(4c)$	$Q_3 = z(A_1) - z(A_2)$
B_{1g} modes:	$4f$ $(8f)$	$Q_1 = y(F_1) - y(F_2) - y(F_3) + y(F_4)$
	$2a, 2b$ $(4c)$	—
B_{2g} modes:	$4f$ $(8f)$	$Q_1 = x(F_1) + x(F_2) - x(F_3) - x(F_4)$
		$Q_2 = z(F_1) - z(F_2) - z(F_3) + z(F_4)$
	$2a, 2b$ $(4c)$	$Q_3 = x(A_1) - x(A_2)$
B_{3g} modes:	$4f$ $(8f)$	$Q_1 = y(F_1) + y(F_2) - y(F_3) - y(F_4)$
	$2a, 2b$ $(4c)$	$Q_2 = y(A_1) - y(A_2)$
A_u modes:	$4f$ $(8f)$	$Q_1 = y(F_1) - y(F_2) + y(F_3) - y(F4)$
	$2a, 2b$ $(4c)$	—
B_{1u} modes:	$4f$ $(8f)$	$Q_1 = x(F_1) - x(F_2) + x(F_3) - x(F_4)$
		$Q_2 = z(F_1) + z(F_2) + z(F_3) + z(F_4)$
	$2a, 2b$ $(4c)$	$Q_3 = z(A_1) + z(A_2)$
B_{2u} modes:	$4f$ $(8f)$	$Q_1 = y(F_1) + y(F_2) + y(F_3) + y(F_4)$
	$2a, 2b$ $(4c)$	$Q_2 = y(A_1) + y(A_2)$
B_{3u} modes:	$4f$ $(8f)$	$Q_1 = x(F_1) + x(F_2) + x(F_3) + x(F_4)$
		$Q_2 = z(F_1) - z(F_2) + z(F_3) - z(F_4)$
	$2a, 2b$ $(4c)$	$Q_3 = x(A_1) + x(A_2)$

Table 2.3.: Symmetry coordinates for all Γ point phonons of NaV_2O_5 and CaV_2O_5 (MgV_2O_5), labeled according to the irreducible representation (Irrep), as resulting from factor group analysis. F_{1-4} refers to equivalent atoms belonging to the one site with Wyckoff position $4f$ $(8f)$, while $A_{1,2}$ refers to the atoms of the $2b$ and $2a$ sites ($2c$ sites), respectively.

as well as the rotations they include, are the same as for the other two vanadates. Moreover, the number of atoms in the primitive cell is the same, such that MgV_2O_5 has the same number of vibrations in each irreducible representation and the same symmetry coordinates as the other two compounds. In detail, the symmetry coordinates for the $8f$ sites (V,O2, O3) of space group *Cmcm* correspond to the ones of the $4f$ sites in the space group *Pmmn*, while the $4c$ sites (Mg, O1) have the same symmetry as the $2a$ and $2b$ sites in NaV_2O_5 and CaV_2O_5.

The factor group analysis (FGA)[2] yields for NaV_2O_5, CaV_2O_5, and MgV_2O_5

[2]Mathematical and technical details about the FGA can be found, e.g., in Ref. [60],

$$\Gamma = 8\ A_g + 3\ B_{1g} + 8B_{2g} + 5\ B_{3g} + 3\ A_u + 7\ B_{1u} + 4\ B_{2u} + 7\ B_{3u}.$$

In this context, the subscript "g" means "gerade" (even), which indicates that the related lattice distortions keep the inversion symmetry, while the subscript "u" ("ungerade" = odd) indicates that inversion symmetry is destroyed.

The explicit symmetry coordinates of the individual irreducible representations as obtained by FGA are presented in Tab. 2.3. In addition, they are visualized in Fig. 2.5. The arrows in this figure do not represent real displacements, but indicate the degrees of freedom and the symmetries involved in the phonons of each irreducible representation. As it can be seen in this figure, the A_g, B_{2g}, B_{1u}, and B_{3u} vibrations are restricted to the x–z plane. In these phonon modes V, O2, and O3 are allowed to move in both, x and z direction. In contrast, the metal ion (Na,Ca,Mg) and the in-rung oxygen O1 in the A_g and B_{1u} modes move only in z direction, while in B_{2g} and B_{3u} symmetry only displacements along z are allowed.

The B_{1g}, B_{3g}, A_u, and B_{2u} oscillations only affect the y coordinates of the atoms, where in the case of B_{1g} and A_u phonons Na (Ca,Mg) and O1 do not contribute.

2.5. Low-temperature structure of NaV_2O_5

Since Isobe *et al.* (Ref. [6]) discovered a spin-Peierls-like phase transition at $T_c = 34$ K in 1996, numerous experiments, applying different techniques, have been aiming at understanding the low-temperature structure of NaV_2O_5. Isobe *et al.* revealed the phase transition by measuring magnetic susceptibilities, and proposed a low-temperature structure containing two kinds of V sites, V^{4+} and V^{5+}, respectively, where V^{4+}/V^{5+} chains in y direction are arranged alternatingly in the x–y plane.

While subsequent ^{23}Na NMR [50], ^{51}V NMR [47], and X-ray/neutron scattering experiments [33] seemed to confirm this charge order for $T<T_c$, a multiplicity of later measurements including X-ray diffraction [9, 10, 11, 12, 13, 14, 20, 61], ^{51}V NMR and ^{23}Na NMR measurements [48, 49, 51], neutron scattering [35] and Raman spectra [19] lead to a controversial discussion about the true nature of NaV_2O_5 at low temperature. This discussion comprises several topics:

- the space group of the low-temperature structure, where one candidate is a orthorhombic $2a \times 2b \times 4c$ supercell with space group $Fmm2$ (no. 42), and the other candidate is a monoclinic $(a-b) \times 2b \times 4c$ cell with space group $A112$ (no. 5);

- the number of V sites, i.e. whether there are two ore three inequivalent vanadium positions;

Ref.	Exp.	Spacegroup	V sites	valences	stacking order
[6]	suscept.	–	2 (chains‖b)	2	–
[33]	X-ray/neutr.	–	2 (chains‖b)	2	–
[50]	Na NMR	–	2	2	–
[47]	V NMR	–	2	2	–
[9]	X-ray	Fmm2 (42)	?	?	A–B–B'–A'
[19]	Raman	B2/b (15)	2 (zig-zag)	2	–
[48]	V/Na NMR	–	2	2	–
[61]	X-ray	Fmm2 (42)	3 (zig-zag+unord.)	3	A–A–A'–A'
[10]	X-ray	*not* Fmm2	2 (zig-zag)	2	–
[51]	Na NMR	*not* Fmm2	2	2	–
[35]	neutron	–	2 (zig-zag)	2	–
[11]	X-ray	Fmm2 (42)	3 (zig-zag+unord.)	2	A–B ?
[12]	X-ray	Fmm2 (42)	2 (zig-zag)		⟨X⟩⟨X⟩⟨Y⟩⟨Y⟩
[13]	X-ray	A112 (5)	2 (zig-zag)	2	A^+–B^+–A^-–B^-
[20]	X-ray	(monoclinic)	2 (zig-zag)	2	AABB+ACBD
[49]	V/Na NMR	–	3	3	–
[14]	X-ray	A112 (5)	2 (zig-zag)	2	A–A–A'–A'

Table 2.4.: Structure variants for the low T phase of NaV_2O_5 as proposed in literature (chronological order). Column 2 indicates the kind of experiment performed, while Cols. 3–6 show the discussed features, i.e. the space group, the number of geometrically distinct V sites, the number of different V valences, and the stacking order in z direction.

- the number of different V valences: variants with two valences (V^{4+}, V^{5+}), three valences ($V^{4.5+}$, V^{4+} and V^{5+}), and other models have been presented.
- the stacking order of the V–O layers along c;

Table 2.4 presents a chronological overview of experimental findings concerning the low-temperature structure, while in the following, the mentioned topics will be discussed in more detail.

2.5.1. Space group and unit cell

Ref. [9] represents the first publication proposing a space group for the low-temperature structure of NaV_2O_5. On the basis of synchrotron radiation X-ray diffraction data, the authors of this reference report an orthorhombic $2a \times 2b \times 4c$ supercell with space group $Fmm2$ (no. 42). This space group is compatible with up to six inequivalent V and Na sites, respectively. Consistent findings in terms of crystal symmetry are also reported in Refs. [61] and [12], which also present X-ray diffraction measurements.

In contrast, the X-ray data of Ref. [10] and ^{23}Na NMR measurements in Ref. [51], where eight different sodium sites are detected, disagree with space group $Fmm2$. Furthermore, a X-ray anomalous scattering experiment presented in Ref. [20] leads to the conclusion that the supercell for T<T_c is monoclinic, which is supported by X-ray diffraction measurements presented in Ref. [13]. Moreover, the latter reference proposes $A112$ (no. 5) as new space group, which implies a $(a-b)\times 2b\times 4c$ supercell (Fig. 2.6) and is compatible with eight inequivalent V and Na positions, respectively. This symmetry of the low temperature phase was also confirmed by X-ray experiments published by Ohwada *et al.* [14].

2.5.2. Geometrical order patterns

The first references discussing the different types of V sites for low temperatures (Refs. [6, 33]) assumed two different kinds of V atoms arranged in chains along the legs of the V–O oxygen ladders (Fig. 2.7 C). In contrast, Raman spectra presented in Ref. [19] contradict to a unit cell with inversion symmetry, as it is the case in a in-line ordered system, and indicate a zig-zag charge ordering instead (Fig. 2.7 B). The X-ray diffraction results discussed in Ref. [61] confirm this symmetry properties, but propose three kinds of V sites, i.e. in addition to V^{5+} and V^{4+} also $V^{4.5+}$ ions . The same number of geometrically different V sites is reported in Ref. [11], where, however, only two different V valences, i.e. $V^{4.5+\delta}$ and $V^{4.5-3\delta}$, are suggested (see Sect. 2.5.3).

Nevertheless, the X-ray experiments published after 2001 [12, 13, 14, 20] consistently suggest that the low-temperature phase of NaV_2O_5 has only two different V sites arranged in a zig-zag like manner.

2.5.3. Charge ordering

The discussion of the charge ordering in NaV_2O_5 at T<T_c is even more controversial than the one regarding its geometrical properties. The first order pattern, which suggested chains of V^{4+}/V^{5+} ions along b (Ref. [6] 1996,Ref. [33] 1997), was refused already quite early. After Konstantinovic *et al.* [19] proposed a zig-zag like charge ordering in 1999, all models based on subsequent results include this pattern, while some of them suggest ladders without ordering in addition. Accordingly, Ref. [61] reports an alternation of zig-zag ordered ladders formed by V^{4+} and V^{5+} ions, and unordered ladders composed of $V^{4.5+}$ sites in the x–y plane, latter representing the same configuration as the high temperature phase. On the other hand, Ref. [11]—while agreeing with Ref. [61] regarding the number of inequivalent V sites—proposes only two significantly different V valences.

However, later references presenting X-ray experiments [12, 13, 20, 14] support the model proposed by Nakao *et al.* [10], which only consists of ladders containing V^{4+} and V^{5+} ions in a zig-zag like arrangement.

2.5.4. Stacking in z direction

In addition to the individual charge ordering patterns, for each of these patterns different stackings in c direction are possible. Lüdecke *et al.* [9] were the first to propose a concrete stacking of V–O planes in z direction, presuming the orthorhombic space group $Fmm2$ (no. 42) with six inequivalent V sites. They suggested two types of layers with different atomic displacements A and B, respectively, which are arranged alternatingly with layers B' and A', where each atom is displaced in the inverse way with respect to its counterpart in layer A or B, respectively, thus giving a stacking of the form A–B–B'–A'.

Boer *et al.* [61], on the other hand, concluded from low temperature X-ray scattering measurements that the low-temperature structure has two crystallographically independent a-b planes exhibiting almost identical displacements, which—together with the F centering—makes them assume a stacking of the kind A–A–A'–A'. In this stacking, V ions are arranged as 4+ 4+ 5+ 5+ along z direction, while each layer contains as well undistorted ladders with $V^{4.5+}$ ions. In contrast to these findings, Sawa *et al.* [13] reported X-ray diffraction results implying another space group than the one suggested by Refs. [9, 11], namely the monoclinic space group $A112$ (no. 5). Only V^{4+} and V^{5+} sites were found, which are always arranged in a zig-zag like manner. They suggested a stacking of the type A^+–B^+–A^-–B^-, where in the layers A (A') continuous chains of V^{4+} (V^{5+}) ions are present in (x,y) direction, while B and B' are build up by pairs of V^{4+} or V^{5+} ions, respectively. As an example, layer A is displayed in Fig. 2.6. Despite of these differences, the arrangement of V ions as presented by Sawa *et al.* is in agreement with Ref. [61], i.e. a sequence 4+ 4+ 5+ 5+ along the z axis.

In this context, it should be mentioned that Smaalen *et al.* [12] at the same time reported high-resolution X-ray results suggesting that possible monoclinic distortions must be smaller than 0.01 Å, thus implying that the unit cell is rather the orthorhombic one proposed by Lüdecke ($Fmm2$). On the other hand, they find that NaV_2O_5 is completely zig-zag ordered. However, this is only compatible with space group $Fmm2$ if the stacking along z is disordered and comprises stacking faults. They suggest a stacking of the type ⟨X⟩⟨X⟩⟨Y⟩⟨Y⟩. Here, ⟨X⟩= ⟨A,D⟩=⟨D,A⟩, and ⟨Y⟩= ⟨B,C⟩=⟨C,B⟩, where e.g. ⟨D,A⟩ denotes a structure which is the average of the structures with layers A and D.

However, few months after Sawa, Grenier *et al.* [20] reported anomalous X-ray diffraction experiments, which suggested again that NaV_2O_5 in its low-temperature phase is not compatible with the orthorhombic $Fmm2$ space group, but should exhibit a monoclinic unit cell. Moreover, they proposed two models for the stacking in z direction, i.e. A–A–B–B and A–C–B–D, respectively. They stated that their experimental data are well reproduced if the two patterns appear simultaneously. This implies that in the low-temperature phase either both domains coexist, or one of the configurations contains stacking faults of the other one.

Finally, the monoclinic nature of the low-temperature unit cell was confirmed

by Ohwada *et al.* [14] in 2005. Their resonant X-ray scattering measurements support the findings of Sawa *et al.*, but suggest a stacking of the form A–A–A'–A', which is still compatible with the results reported by the latter.

2.5.5. Electric Field Gradients and Nuclear Magnetic Resonance – definitions and relations

One important characteristic of a solid, which is helpful to distinguish the number of different sites occupied by a certain element from the periodic table, is provided by the Electric Field Gradients (EFG), which is the second spatial derivative of the Coulomb potential at the nuclear position. When EFGs, the coordinate system is conveniently chosen in such a way that V_{zz} corresponds to the largest component, and

$$|V_{zz}| \geq |V_{yy}| \geq |V_{xx}|.$$

Simultaneously, the relation

$$V_{zz} + V_{yy} + V_{xx} = 0$$

holds, such that V_{xx} and V_{yy} must necessarily have the opposite sign of V_{zz}. Throughout this chapter, for both, theoretical and experimental results, V_{zz} is taken to be positive, such that V_{xx} and V_{yy} will have a negative sign. In addition to the components of the EFG, the asymmetry parameter η may be considered, which is defined as

$$\eta = \frac{V_{xx} - V_{yy}}{V_{zz}}$$

and can vary between zero and one. This implies, that the following relations hold:

$$V_{yy} = -\tfrac{1}{2}V_{zz}(1+\eta) \text{ and } V_{xx} = -\tfrac{1}{2}V_{zz}(1-\eta).$$

Experimentally, the EFG can be detected via its interaction with the quadrupolar moment of the nucleus. Thus, for elements that have a quadrupole moment it can be measured by spectroscopic methods which determine the quadrupolar frequency, such as Nuclear Magnetic Resonance (NMR), Nuclear Quadrupole Resonance (NQR), Moessbauer or Perturbed Angular Correlation (PAC). The relation between the quadrupolar frequency of a nucleus, $\nu_{\alpha\alpha}$, and the EFG $V_{\alpha\alpha}$, is

$$V_{\alpha\alpha}[V/m^2] = \frac{h}{eQ}\frac{2I(2I-1)}{3} \times 10^6\, \nu_{\alpha\alpha}[MHz],$$

where h is the Planck constant ($6.626075 * 10^{-34}\, J\, s$), $e = 1.60210^{-19}\, C$ is the elementary charge, Q is the nuclear quadrupolar moment in Barn ($1\, b = 10^{-28}\, m^2$), and I is the nuclear spin (Q and I for all elements can be found, for example, in Ref. [62]). For vanadium, $I_V = 7/2$ and $Q_V = -0.052$, while for sodium one finds $I_{Na} = 3/2$ and $Q_{Na} = 0.104$.

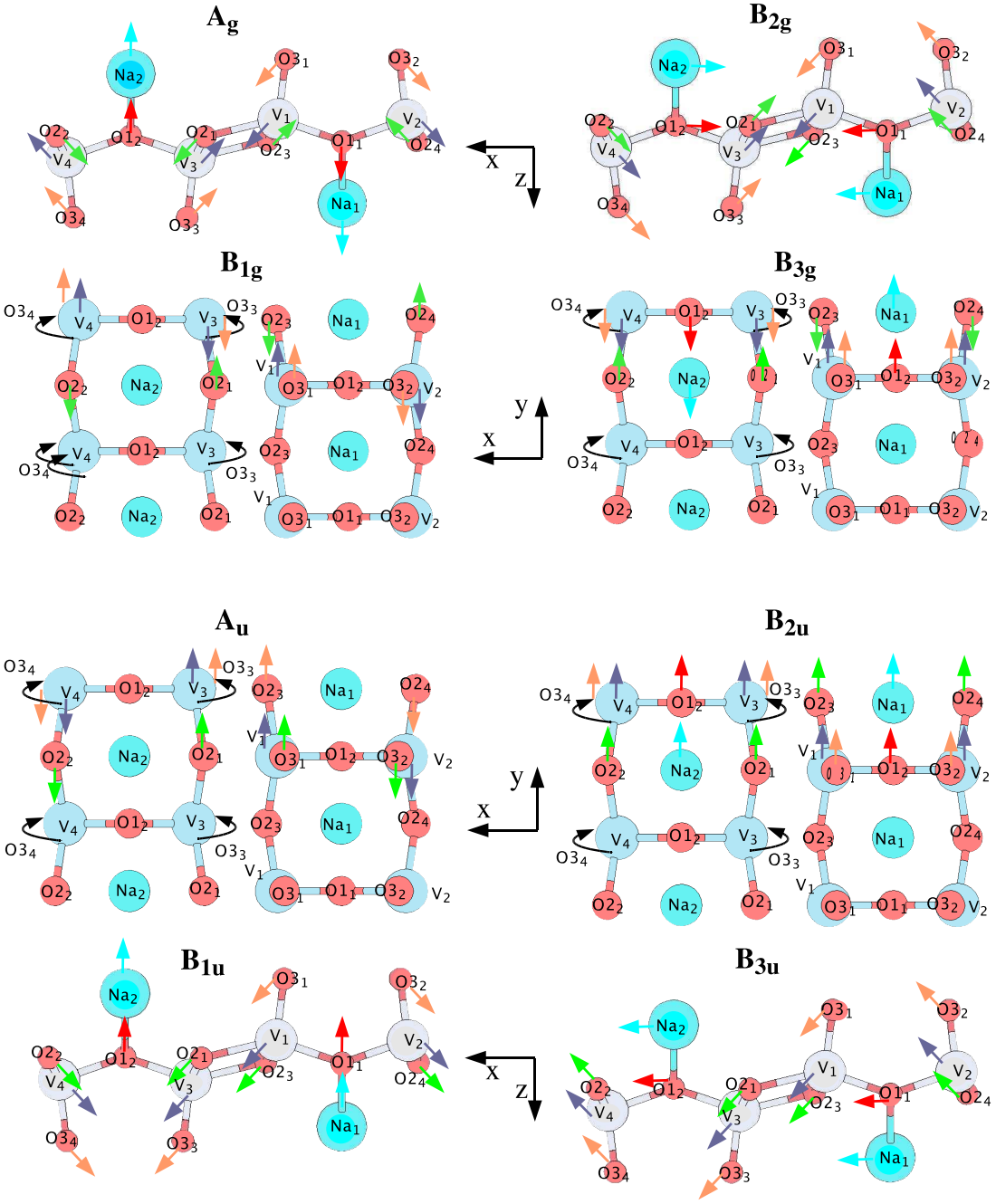

Figure 2.5.: Symmetry coordinates for *gerade* (upper panel) and *ungerade* modes (lower panel) of NaV_2O_5 (CaV_2O_5) as resulting from a factor group analysis. The subscripts indicate the numbering of the equivalent atoms for each type of atoms. The arrows do not correspond to real displacements. Instead, they symbolize the degrees of freedom participating in each irreducible presentation and show the symmetry of the displacements.

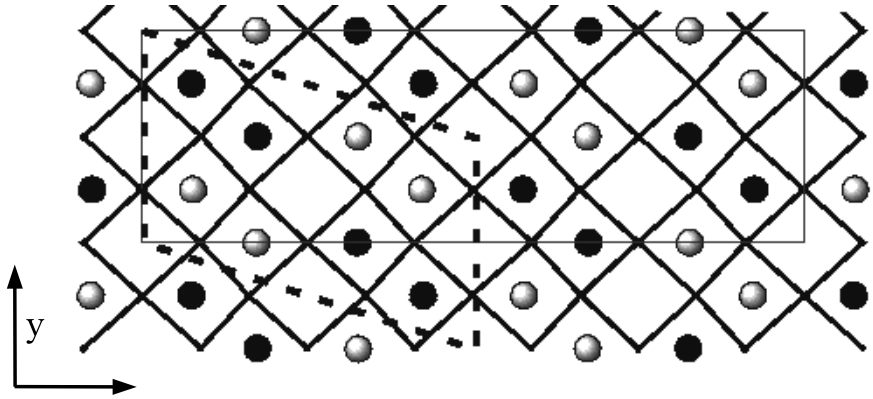

Figure 2.6.: Unit cell choices (x–y plane) for the low-temperature structure of NaV_2O_5 as presented in Ref. [13]. The thin continuous line shows the orthorhombic unit cell, while the dashed line refers to the monoclinic one. Solid and open circles represent V^{4+} and V^{5+} sites, respectively. The displayed charge-order corresponds to layer A^+ of the cited reference.

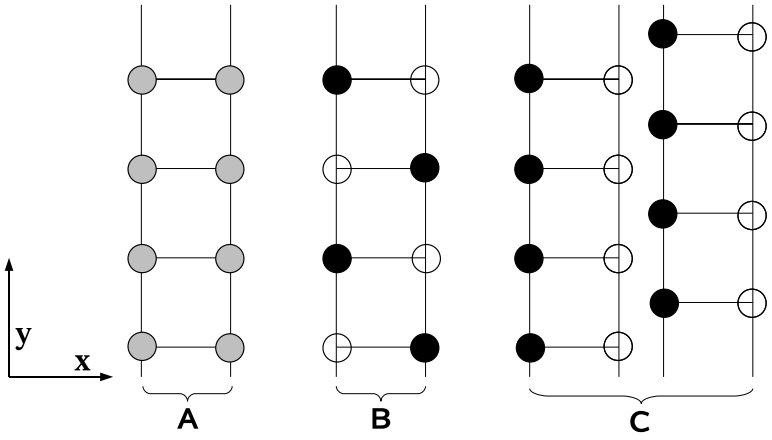

Figure 2.7.: Candidates for ordering patterns of the V sites in NaV_2O_5 ($T<T_c$). Empty circles correspond to V^{5+}, grey circles to $V^{4.5+}$, and black circles to V^{4+} ions. (A) represents the ladder without ordering (as in the high T structure), (B) the zig-zag charge ordering, and (C) a structure with V^{+4} (V^{+5}) chains in y direction.

Part I.

Theory

3. DFT and the Family of APW Methods

3.1. Density Functional Theory

3.1.1. Introduction

Traditionally, a quantum mechanical system of interacting particles is described by the many-body wave function comprising all particles of the system. In case of a solid, this would mean that the many-body wave function includes all electrons and nuclei of the material under consideration. However, in most cases in solids nuclear and electronic degrees of freedom are separable (Born-Oppenheimer approximation, see Sect. 4.1) and, therefore, the Coulomb energy of the electrons with respect to the nuclei can be treated as external potential [1]. Thus, the electronic system is described by the many-particle wave-function of all electrons $\Psi(\vec{r}_1, \vec{r}_2, \vec{r}_3, ..., \vec{r}_N)$, where $\vec{r}_1..\vec{r}_N$ denote the electronic coordinates including the spin, and N is the total number of electrons.

As an alternative, Thomas [63] and Fermi [64] proposed already in the years 1926–1928 a scheme to describe a solid based on the electron density of the system. This, however, presumed uncorrelated electrons and that the kinetic energy can be described by a local approximation using the respective free-electron result. Even though the success of the Thomas-Fermi approach in the description of real systems was rather limited, it represented a first attempt to describe a solid as functional of its electron density. The so called *density functional* approach has two big advantages: First, that the electron density is much easier to obtain than the precise details of the many-body wave function Ψ. Second, the scaling behavior is much better, such that presently systems with a number of atoms in the range of hundreds to several thousands can be calculated. In contrast, the computational effort of calculations describing a system by its many-electron wave function, which can be done, e.g., by means of Slater determinants, increases exponentially with $\mathcal{N}$ and is therefore feasible only for systems with little more than ten atoms [65].

[1] Throughout this chapter, the validity of this approximation will be assumed

3.1.2. The Hohenberg-Kohn theorem

The Hohenberg and Kohn theorem formulated in 1964 [66] marks the starting point of modern density functional theory (DFT). The basic Hohenberg-Kohn lemma states that for a system of interacting electrons in some external potential $v_{ext}(\vec{r})$ a unique relation between the ground state electron density $n(\vec{r})$ and $v_{ext}(\vec{r})$ exists, since the electron density determines the external potential *uniquely* (up to an additive constant). Thus, the total energy E of the system may be written as

$$E = \left\langle \Psi | \hat{H} | \Psi \right\rangle = \int v_{ext}(\vec{r}) n(\vec{r}) d^3r + \left\langle \Psi | \hat{T} + \hat{U} | \Psi \right\rangle = \int v_{ext}(\vec{r}) n(\vec{r}) d^3r + F[n(\vec{r})] \tag{3.1}$$

where $\hat{T}$ and $\hat{V}$ represent the kinetic and interaction energy operators, respectively.

While the original proof still assumed a non-degenerate ground state, this restriction was later on lifted by Kohn [67]. Another question involved is, whether there are well-behaved positive function $n(\vec{r})$, integrating up to the number of electrons N, where *no* corresponding ground state potential $v(\vec{r})$ *exists* (problem of the v-representability). In fact, Levy [68] and Lieb have shown that this is actually the case, which, however, does not appear to limit the applicability of DFT to real physical systems. An important consequence of the Hohenberg-Kohn lemma is that also the many-body wave function Ψ is a functional of $n(\vec{r})$. Moreover, this implies that the full Hamiltonian $\hat{H}$ of the electronic system is given be the density, and that $n(\vec{r})$ implicitly contains all properties derivable from $\hat{H}$ through solution of the Schrödinger equation.

In a second step, Hohenberg and Kohn show—using a minimum principle with respect to trial densities $\tilde{n}(\vec{r})$—that the total energy E is a functional of the electron density, $E = E[n(\vec{r})]$, and that the ground state density minimizes $E[n(\vec{r})]$:

$$E = \min_{\tilde{n}(\vec{r})} E_v[\tilde{n}(\vec{r})] = \min_{\tilde{n}(\vec{r})} \left\{ \int v_{ext}(\vec{r}) \tilde{n}(\vec{r}) d^3r + F[\tilde{n}(\vec{r})] \right\}. \tag{3.2}$$

The functional $F[\tilde{n}(\vec{r})]$ is defined as

$$F[\tilde{n}(\vec{r})] = \min_{\alpha} \left\langle \Psi^{\alpha}_{\tilde{n}} | \hat{T} + \hat{U} | \Psi^{\alpha}_{\tilde{n}} \right\rangle, \tag{3.3}$$

where the minimization is done with respect to all $\Psi^{\alpha}_{\tilde{n}}$ giving the correct electron density $\tilde{n}(\vec{r})$. An important point is that $F[\tilde{n}(\vec{r})]$ is *independent* of the external potential $v_{ext}(\vec{r})$. Equation 3.2 is also known as the *Hohenberg-Kohn minimum principle*. An alternative formulation of the minimum principle was presented by Levy [68], who used a constrained search method.

3.1.3. The self-consistent Kohn-Sham equations

The Hohenberg-Kohn formulation of the DFT is a strict formulation, but it does not provide expressions for $F(\tilde{n}(\vec{r}))$. In order to obtain such explicit expressions, it is useful to rewrite $F(\tilde{n}(\vec{r}))$ in the form

$$F[\tilde{n}(\vec{r})] = T_s[\tilde{n}(\vec{r})] + \underbrace{\frac{1}{2}\int \frac{\tilde{n}(\vec{r})\tilde{n}(\vec{r'})}{|\vec{r}-\vec{r'}|} d^3r d^3r'}_{E_H} + E_{xc}[\tilde{n}(\vec{r})]. \tag{3.4}$$

Here, $T_s[\tilde{n}(\vec{r})]$ represents the kinetic energy of the non-interacting electron system, while the exchange-correlation functional $E_{xc}[\tilde{n}(\vec{r})]$ is *defined* by Equations 3.3 and 3.4, i.e. it comprises all contributions left after subtraction of T_s and the Hartree energy E_H.

Now we apply the Hohenberg-Kohn minimum principle in order to obtain the Euler-Lagrange equations for $F(\tilde{n}(\vec{r}))$. We perform a variation of the total energy E with respect to the density $\tilde{n}(\vec{r})$, keeping the total number of electrons constant, and get

$$\delta E_v[\tilde{n}(\vec{r})] = \int \delta\tilde{n}(\vec{r}) \left\{ v_{eff}(\vec{r}) + \frac{\delta}{\delta\tilde{n}(\vec{r})} T_s[\tilde{n}(\vec{r})]\Big|_{\tilde{n}(\vec{r})=n(\vec{r})} - \varepsilon \right\} d^3r = 0. \tag{3.5}$$

Here, $v_{eff}(\vec{r})$ is defined as the sum of the external, the Hartree, and the exchange-correlation potential,

$$v_{eff}(\vec{r}) = v_{ext}(\vec{r}) + \int \frac{n(\vec{r'})}{|\vec{r}-\vec{r'}|} d^3r' + v_{xc}(\vec{r}), \tag{3.6}$$

where the exchange-correlation potential $v_{xc}(\vec{r})$ represents the functional derivative of the exchange-correlation energy with respect to the electron density

$$v_{xc}(\vec{r}) = \frac{\delta}{\delta\tilde{n}(\vec{r})} E_{xc}[\tilde{n}(\vec{r})]\Big|_{\tilde{n}(\vec{r})=n(\vec{r})} \tag{3.7}$$

The Lagrangian multiplier ε assures the conservation of the number of electrons in the variational procedure. Formally, Eq. 3.5 is identical with the result for non-interacting particles in an external potential $v_{eff}(\vec{r})$. Consequently, Kohn and Sham [69] concluded that the minimizing density $n(\vec{r})$ can be calculated by solving the single-particle Schrödinger equation

$$\left[-\frac{1}{2}\nabla^2 + v_{eff}(\vec{r}) - \varepsilon_j \right] \varphi_j(\vec{r}) = 0, \tag{3.8}$$

where the density is obtained from the single particle orbital $\varphi_j(\vec{r})$ through

$$n(\vec{r}) = \sum_{j=1}^{N} |\varphi_j(\vec{r})|^2. \tag{3.9}$$

The equations 3.8 for different indexes j are known as the *Kohn-Sham equations*.

In order to solve these equations, a self-consistent procedure can be performed. Starting from an initial guess for the effective potential v_{eff}, the Kohn-Sham equations are diagonalized yielding the Kohn-Sham energy ε_j and orbitals φ_j, which give the density $n(\vec{r})$. The density, in turn, determines a new Kohn-Sham potential v_{eff} by applying relations 3.6 and 3.7. This procedure can be repeated until the ground state density is converged. Then, the total energy of the system E can be calculated as

$$E = \sum_{j=1}^{N} \varepsilon_j + E_{xc}[n(\vec{r})] - \int v_{xc}(\vec{r}) n(\vec{r}) d^3r - \frac{1}{2} \int \frac{n(\vec{r}) n(\vec{r'})}{|\vec{r} - \vec{r'}|} d^3r d^3r'. \tag{3.10}$$

In principle, this procedure does not involve any approximations and would lead to exact ground state properties, if $E_{xc}[n(\vec{r})]$ and v_{xc} would be exact and would include all many-body effects. In real life, approximations for $E_{xc}[n(\vec{r})]$ have to be used, and actually it is the effectiveness and accuracy of the functional $E_{xc}[n(\vec{r})]$ that determines how useful the Kohn-Sham equations are when they are applied to concrete physical systems. In the following, the two most common approximations will be introduced.

3.1.4. Approximations for E_{xc}

Local Density Approximation

In the Local Density approximation, the value of $E_{xc}[n(\vec{r})]$ from the homogeneous electron gas with density $n(\vec{r})$ is used:

$$E_{xc}^{LDA} = \int n(\vec{r}) \varepsilon_{xc}^{LDA}(n(\vec{r})) d^3r. \tag{3.11}$$

$E_{xc}[n(\vec{r})]$ can be further split up into exchange and correlation part

$$E_{xc}^{LDA}[n(\vec{r})] = E_x^{LDA}[n(\vec{r})] + E_c^{LDA}[n(\vec{r})], \tag{3.12}$$

where the exchange part E_x^{LDA}, is replaced by the corresponding analytic expression

$$E_x^{LDA}[n(\vec{r})] \propto n(\vec{r})^{4/3}. \tag{3.13}$$

Consequently, one obtains $v_{xc} \propto n(\vec{r})^{1/3}$.

For $E_c^{LDA}[n(\vec{r})]$, different parameterizations exist, which are all based on the results of Ceperley and Alder [70], who obtained $E_c^{LDA}[n(\vec{r})]$ from quantum Monte Carlo simulations for the homogeneous electron gas. One of the expressions most widely used in solid state calculations is the one suggested suggested by Perdew and Wang [71]. Despite its simplicity, LDA is capable to describe a relatively large number of systems with satisfying accuracy. This is also due to the fact that, in real systems, the error in the exchange part (underestimated by typically

$\mathcal{O}(10\%)$) and in the correlation part (overestimated up to a factor of 2) tend to compensate each other [67]. Regarding the geometry of crystals and molecules, LDA usually underestimates the bond lengths by 1% – 5%, which is the known over-binding effect of LDA. Special care has to be taken with regard to the band gap of insulators and semi-conductors when working with LDA. It is well-known that the gap obtained from LDA is approximately 50% smaller than the actual gap (see e.g. Ref. [72]).

Generalized Gradient Approximation

Some of the shortcomings of LDA can be overcome by using a modified ansatz for $E_{xc}[n(\vec{r})]$, where it does not only depend on the local electron density $n(\vec{r})$, but also on gradient terms:

$$E_{xc}[n(\vec{r})] = \int f(n(\vec{r}), |\nabla n(\vec{r})|) n(\vec{r}) d^3r. \tag{3.14}$$

Historically, already Hohenberg and Kohn proposed in 1965 [69] a relatively simple approach for E_{xc}, where they expanded the exchange-correlation energy in terms of the charge density and included the second order terms $|\nabla n(\vec{r})|^2$, called gradient expansion approximation (GEA). However, this method was not rigorously able to improve over LDA. In the following years, new attempts to improve E_{xc} using density gradients were made. First-principles numerical Generalized Gradient Approximations (GGA), starting from the second order gradient expansion of GEA, were performed for systems with slowly varying density, where spurious long-range parts were cut off. This way, unphysical contributions of the GEA could be removed. Perdew and Wang included an analytic fit to this numerical GGA in the GGA-PW91 functional [71], while a further improvement by Perdew, Burke and Ernzerhof 1996 lead to the GGA-PBE functional published in Ref. [73]. The latter functional has proven to be very successful for systems with slowly varying charge density and often considerably improves the results in terms of bond-lengths as well as atomization energies [67].

3.2. Augmented Plane Wave methods

3.2.1. The LAPW Method

After introducing DFT as a framework to tackle the theoretical many-body problem of electrons in a solid in an effective way, we are now interested in finding a suitable method for solving the Kohn-Sham equations 3.8 in a solid. Such a method is found in the linearized augmented plane–wave (LAPW) method [74, 75]. The principle idea of the LAPW method is to use different basis functions for different regions in the unit cell, such that the basis set is well suited for

the problem to be studied. When looking for a complete and orthogonal basis for all functions having lattice periodicity, plane waves are a good candidate. Thus they can be used for describing the one–electron wave functions. Wave functions of this type are then exact solutions of the Schrödinger equation involving a constant potential. Therefore such a basis gives a good description in the region in between the atoms, where the potential does not vary very much.

In contrast, near the atoms the potential is governed by the Coulomb interaction with the nuclei and changes strongly, as visualized in Fig. 3.1. Therefore, plane–waves are no suitable basis set for this region of the a solid, since one would need very many of them to describe the wave function appropriately. Instead, the solution of the Schrödinger equation in this region will be similar to wave functions of free atoms.

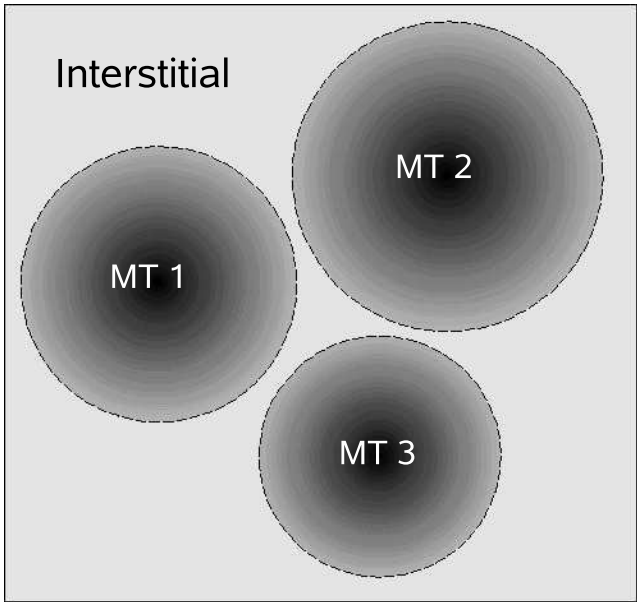

Figure 3.1.: Splitting of the space into the "muffin tin" regions around the atomic nuclei (MT1,MT2,MT3) and the interstitial. The gray-scale-gradient inside the muffin-tins symbolizes the change of potential in the atomic region.

The LAPW method now combines these two properties. The unit cell is split into two different regions (Fig. 3.1). Around the nuclear positions, atom–like wave functions are used as basis. This region is called the *atomic spheres* or the *muffin–tin* region. In between these spheres is the so called *interstitial*, where a plane-wave expansion is used.

Due to these different descriptions of basis functions certain boundary conditions have to be fulfilled: The wave function and its slope have to be continuous on the spheres' surfaces. This can be ensured by constructing the basis set in such a way that the basis itself fulfills these requirements. The fact that the

plane waves in the interstitial are continued by atom–like basis functions in the muffin–tin spheres, leads to the term *augmented plane waves*, which gives the name for this method.

It is common to abbreviate the terms interstitial and muffin tin with I and MT, respectively. In principle there is no restriction for choosing the sphere radii other than making the spheres non-overlapping. In practice, however, it is useful to choose the radii as big as possible. This makes it easier to treat the leaking wave function with a plane–wave basis set.

The basis functions ϕ are now chosen individually for the spheres and the interstitial:

$$\phi_{\vec{k}+\vec{K}}(\vec{r}) = \begin{cases} \frac{1}{\sqrt{\Omega}} e^{i(\vec{k}+\vec{K})\vec{r}} & \vec{r} \in \text{interstitial} \\ \sum_{l=0}^{l_{\max}} \sum_{m=-l}^{l} \left(a_{lm}^a u_l + b_{lm}^a \dot{u}_l\right) Y_{lm}(\hat{r}_a) & |\vec{r} - \vec{r}_a| \leq R_a \end{cases} \tag{3.15}$$

Here, Ω stands for the volume of the unit cell, $\vec{k}$ is a vector within the first Brillouin zone, and $\vec{K}$ is a reciprocal lattice vector. The parameters $a_{lm}^a(\vec{k}+\vec{K})$ and $b_{lm}^a(\vec{k}+\vec{K})$ ensure the desired continuity of the wave function mentioned above. $\vec{r}_a$ is the center of the sphere around atom a, and R_a is its radius. The sum over the angular momentum quantum numbers l, m is restricted by a certain maximum $l_{\max}$. The functions u_l and $\dot{u}_l$ are some radial functions, which need to be explained in some more detail. They are calculated as the solutions of a Schrödinger equation, involving just the spherical part of the potential.[2] This simplification leads to the desired atom–like eigenfunctions and the result can be written as products of radial functions $u_l(r)$ and angle–dependent spherical harmonics $Y_{lm}(\hat{r})$. The radial functions $u_l(r)$ are the solutions of the radial Schrödinger equation (regular at the origin):

$$\Big[-\frac{d^2}{dr^2} + \frac{l(l+1)}{r^2} + V(r)^{\text{sph}} - E_l \Big] r u_l(r) = 0 \tag{3.16}$$

The functions $\dot{u}_l(r)$ satisfy the equation

$$\Big[-\frac{d^2}{dr^2} + \frac{l(l+1)}{r^2} + V(r)^{\text{sph}} - E_l \Big] r \dot{u}_l(r) = r u_l(r) \, . \tag{3.17}$$

However, there is one important difference between the solution of free atoms and the solution of equation (3.16). Due to the fact that the volume of the muffin–tin spheres is restricted, it can no longer be required that the functions $u_l(r)$ vanish for $r \to \infty$. A conclusion of this is that for any arbitrary energy E_l there is a solution $u_l(r)$, which will therefore be classified as $u_l(r, E_l)$ or simply u_l. But if the basis functions are energy dependent, the secular equation will be

[2] In a relativistic approach the Dirac equation is solved instead of the Schrödinger equation. In this case the framework stays the same, just the radial functions become spinors then.

energy dependent as well. In this case the energy expectation value E_l cannot be calculated by diagonalization. The only way to solve the secular equation is to choose energy values and calculate the determinant of the secular matrix until it vanishes (this is for example done in the APW method). As one would expect, this is very expensive.

The LAPW method bypasses this problem by choosing certain values E_l and solving the Schrödinger equation with these values. However, the solutions u_l now have a little drawback. The radial functions for fixed E_l are not able to describe the wave function over a wide energy region. This problem can be solved by including the energy derivative of u_l, i.e. $\dot{u}_l$. The result is a linear approximation for the energy dependence, which leads to the name *linearized* augmented plane wave method.

The following normalization integrals are fulfilled:

$$\int_0^{R_a} r^2 u_l(r)\, u_l(r) dr = 1 \tag{3.18a}$$

$$\int_0^{R_a} r^2 u_l(r)\, \dot{u}_l(r) dr = 0 \tag{3.18b}$$

$$\tag{3.18c}$$

Moreover, we define:

$$\int_0^{R_a} r^2 \dot{u}_l(r)\, \dot{u}_l(r) dr \equiv N_l \ . \tag{3.19}$$

Note that the u_l are not orthogonal, which is a consequence of choosing the energies E_l instead of taking the exact solutions.

The required properties of the basis functions concerning continuous value and slope at the sphere boundaries are guaranteed, if the coefficients a_{lm} and b_{lm} take the following form,

$$a^a_{lm}(\vec{k}+\vec{K}) = \frac{4\pi}{\sqrt{\Omega}} i^l Y^*_{lm}(\vec{k}+\vec{K}) a_l(\vec{k}+\vec{K}) R_a^2 e^{i(\vec{k}+\vec{K})\vec{r}_a} \tag{3.20a}$$

$$b^a_{lm}(\vec{k}+\vec{K}) = \frac{4\pi}{\sqrt{\Omega}} i^l Y^*_{lm}(\vec{k}+\vec{K}) b_l(\vec{k}+\vec{K}) R_a^2 e^{i(\vec{k}+\vec{K})\vec{r}_a} \tag{3.20b}$$

$$a_l(\vec{k}+\vec{K}) = j_l'(|\vec{k}+\vec{K}|R_a)\dot{u}_l(R_a) - j_l(|\vec{k}+\vec{K}|R_a)\dot{u}_l'(R_a) \tag{3.20c}$$

$$b_l(\vec{k}+\vec{K}) = j_l(|\vec{k}+\vec{K}|R_a)u_l'(R_a) - j_l'(|\vec{k}+\vec{K}|R_a)u_l(R_a)\ , \tag{3.20d}$$

with j_l denoting the spherical Bessel functions. The prime indicates the derivative with respect to r and terms like $j_l'(|\vec{k}+\vec{K}|R_a)$ should be read as $\frac{d}{dr} j_l(|\vec{k}+\vec{K}|r)|_{r=R_a}$.

In order to improve upon the linearization and to make it possible to treat semi-core and valence states within the same energy window, additional functions at different energies can be added. This idea was introduced by D. Singh in

Reference [76]. The so called *local orbitals* are linear combinations of two radial functions at different energies and one energy derivative, and they correspond to a given angular momentum l_{lo}. They are local in the sense they are completely confined within the MT spheres, and that they vanish at the sphere boundary.

The wave function with index i can now be written as

$$\psi^i_{\vec{k}}(\vec{r}) = \sum_{\vec{K}}^{K_{\max}} C^i_{\vec{k}+\vec{K}}\ \phi_{\vec{k}+\vec{K}}(\vec{r})\ , \tag{3.21}$$

where $C^i_{\vec{k}+\vec{K}}$ are coefficients obtained from a variation calculation. In general, these coefficients are complex numbers, i.e. $C^i \in$ C. For crystals with inversion symmetry, however, the systems origin can always be moved to the center of inversion, what leads to the fact that $C^i \in$ R. The sum over all $\vec{K}$ is in principle not limited. However, in order to do numerical calculations on a computer, some cut–off parameter $K_{\max}$ has to be introduced.

The wave functions $\psi^i_{\vec{k}}(\vec{r})$ build up the charge density $\rho(\vec{r})$,

$$\rho(\vec{r}) = \sum_{i,\vec{k}} n^i_k |\psi^i_{\vec{k}}(\vec{r})|^2\ , \tag{3.22}$$

with $n^i_{\vec{k}}$ being the occupation numbers.

The ability of accurately treating valence as well as core electrons leads to the expression *all electron calculation*. The *valence* electrons can perfectly be treated with the method described above. They "feel" the potential of the whole unit cell and their quantum mechanical states are delocalized. The *core* electrons, however, are very deep lying levels in energy and it would not be easy to treat them within the same picture. They are most influenced by the spherical Coulomb potential of the nucleus. Their states are strongly localized and show no dispersion in reciprocal space. An atomic calculation gives a satisfying approximation here and allows to treat them in a relativistic scheme, i.e. by solving the Dirac equation. The core wave functions vanish outside the spheres, if the radii are chosen big enough. The states higher in energy, the so-called semi-core states, are typically described by local orbitals, as described above.

Also the potential $V(\vec{r})$ and the charge density $\rho(\vec{r})$ have to be expanded, where an analogous dual representation is used:

$$\rho(\vec{r}) = \begin{cases} \sum\limits_{\vec{G}} \rho_{\vec{G}}\ e^{i\vec{G}\vec{r}} & \vec{r} \in \text{I} \\ \sum\limits_{lm} \rho_{lm}(r) Y_{lm}(\hat{r}) & \vec{r} \in \text{MT} \end{cases} \tag{3.23}$$

$$V(\vec{r}) = \begin{cases} \sum\limits_{\vec{G}} V_{\vec{G}}\ e^{i\vec{G}\vec{r}} & \vec{r} \in \text{I} \\ \sum\limits_{lm} V_{lm}(r) Y_{lm}(\hat{r}) & \vec{r} \in \text{MT}. \end{cases} \tag{3.24}$$

Advantages - disadvantages:

Due to its rather sophisticated basis set, the LAPW method is not easy to handle. The splitting of the unit cell into the interstitial and muffin–tin region complicates the solution of integrals, i.e. matrix elements. This means, that integrals often cannot be evaluated as easily as within other methods, which is also reflected in the computer time and memory needed for complex materials.

On the other hand, this method provides a most powerful tool. Due to its high accuracy it is often used as a reference for other methods. While in a plane–wave method it is necessary to substitute the original potential by a "pseudorized" one, the LAPW method takes the *full potential* into account. This means that in comparison to the pseudo–potential method, all electrons of a material can be treated and therefore LAPW is a real ab-initio method. As a result of that, the physics of the core region can be examined. Also the treatment of compounds with heavy atoms can be done straightforwardly, such that all elements of the periodic table can be handled on the same footing.

3.2.2. The APW+lo method

Comparing LAPW to its predecessor, the APW method, which was first introduced by Slater [77], two important differences are found:

- Within the APW method, no linearization of the eigenvalue problem can be achieved. This is a major disadvantage: Since the basis functions are energy-dependent, instead of obtaining all eigenvalues in one step by diagonalizing the Hamiltonian (as in the LAPW method), one has to find the zeros of the Hamiltonian matrix as a function of energy, which is computationally very challenging.

- Within the APW method, only the basis functions themselves have to be continuous at the muffin-tin sphere boundaries. This point actually represents an advantage of APW, since a smaller plane-wave cut-off can be used to describe the wave functions appropriately.

Fortunately, a recently proposed method by Sjöstedt *et al.* [78] combines the advantages of both, the APW and the LAPW method. It uses an energy-independent basis, but adds local orbitals to improve the variational freedom and to enable a linearization of the eigenvalue problem. Thus, the so-called APW+lo consists of APW functions with fixed linearization energies

$$\phi_{\vec{k}+\vec{K}}(\vec{r}) = \begin{cases} \frac{1}{\sqrt{\Omega}} e^{i(\vec{k}+\vec{K})\vec{r}} & \vec{r} \in \text{interstitial} \\ \sum_{l=0}^{l_{\max}} \sum_{m=-l}^{l} \left(A_{lm}(\vec{k}+\vec{K}) u_l(r, E_l) Y_{lm}(\hat{r}_a) \right. & |\vec{r} - \vec{r}_a| \leq R_a \end{cases} \tag{3.25}$$

plus local orbitals analogous to the ones described in Sect. 3.2.1, which are taken at the same linearization energy E_l. In fact, as already shown in Ref. [78], e.g. the total energies of molecular O_2 or bulk Cu converge faster with respect to the plane-wave cut-off when using an APW+lo basis instead of LAPW.

4. The Dynamics of the Crystal Lattice - Theoretical Background

4.1. The Born-Oppenheimer approximation

The total Hamiltonian of a solid is composed by the following terms:

$$\hat{H} = \hat{H}_{el}(\vec{r}) + \hat{H}_{lat}(\vec{R}) + \hat{H}_{el,lat}(\vec{r}, \vec{R}). \tag{4.1}$$

Here, $\vec{r}$ and $\vec{R}$ denote the positions of all electrons and nuclei, respectively. In this expression, $\hat{H}_{el}$ and $\hat{H}_{lat}$ contain the respective kinetic and potential energies, whereas $\hat{H}_{el,lat}$ describes the interaction between of the electrons and the nuclei. In order to solve this many-body problem for a real compound, several approximations have to be done.

In a first step, we consider the masses of electrons and nuclei, which differ by a factor of 10^4 to 10^6. Correspondingly, the electrons have a much higher velocity than the nuclei, such that they are able to follow changes of the atomic positions virtually instantaneously. Therefore the electrons may be treated as moving in the static field of the nuclei located at fixed atomic positions described by the coordinates $\vec{R}$,

$$\left[\hat{H}_{el}(\vec{r}) + \hat{H}_{el,lat}(\vec{r}, \vec{R})\right] \psi_{el} = E_{el}(\vec{R})\psi_{el}(\vec{r}, \vec{R}). \tag{4.2}$$

This approximation is known as the Born-Oppenheimer approximation (Refs.[79, 80]). Using Eq. 4.2, the total energies (or forces acting on each atom) for several configurations of "frozen" atomic coordinates can be calculated and used for the setup of the dynamical matrix as shown in the subsequent section. Therefore this method of calculating phonon eigenmodes is also called the "Frozen Phonon Approximation". In the following we assume that for the systems under consideration the requirements of the Born-Oppenheimer approximation are fulfilled.

4.2. Equations of motion

In this section, the equations of motion for a perfect crystal with periodic boundary conditions at T = 0 K are derived. For a more detailed introduction to the topic see also Refs. [81, 82]. Introducing $\vec{R}_\alpha$ as the position of atom α *within* an

arbitrary unit cell and $\vec{R}_n$ as the position vector *of* this unit cell, the equilibrium position of an atom can be written as $\vec{R}_{n\alpha} = \vec{R}_n + \vec{R}_\alpha$. If we define $s_{n\alpha i}$ as the i^{th} Cartesian component (i.e. $i \in \{x, y, z\}$) of the displacement vector of atom α in unit cell n, the kinetic energy of this atom reads

$$T = \sum_{n=1}^{N} \sum_{\alpha=1}^{r} \sum_{i=1}^{3} \frac{M_\alpha}{2} \left(\frac{ds_{n\alpha i}(t)}{dt} \right). \tag{4.3}$$

Here, M_α is represents the mass of atom α, N is the total number of unit cells, and r the number of atoms in one unit cell, such that total number of degrees of freedom equals $3rN$.

In a next step, the potential energy W, which is a function of the coordinates of the atomic position $\vec{x}$, can be written in terms of a Taylor series:

$$W = W(\vec{R}_{n\alpha}) + \sum_{n\alpha i} \underbrace{\left[\frac{\partial W(\vec{x})}{\partial s_{n\alpha i}} \right]_{\vec{x}=\vec{R}_{n\alpha}}}_{=0} s_{n\alpha i} + \tag{4.4}$$

$$+ \sum_{n\alpha i} \sum_{n'\alpha' i'} \underbrace{\left[\frac{\partial^2 W(\vec{x})}{\partial s_{n\alpha i} \partial s_{n'\alpha' i'}} \right]_{\vec{x}=\vec{R}_{n\alpha}}}_{=\Phi_{n\alpha i}^{n'\alpha' i'}} s_{n\alpha i} s_{n'\alpha' i'} + \mathcal{O}(s^3) \tag{4.5}$$

In this equation, the force constants $\Phi_{n\alpha i}^{n'\alpha' i'}$ represent the change of the i'^{th} component of the force acting on atom α' in unit cell n', if the atom α in the unit cell n is displaced in direction i. It can alternatively be written as

$$\Phi_{n\alpha i}^{n'\alpha' i'} = \frac{\partial F_{n'\alpha' i'}}{\partial s_{n\alpha i}} = \frac{\partial F_{n\alpha i}}{\partial s_{n'\alpha' i'}}. \tag{4.6}$$

Since the expansion is done around the equilibrium position, where the first derivative of W with respect to x must be zero, the linear term in Eq. 4.4 vanishes.

In order to formulate the equations of motion we define the Lagrange function for our problem, $\mathcal{L} = T - W$, and obtain the Euler-Lagrange equations

$$\frac{d}{dt} \frac{\partial \mathcal{L}}{\partial \dot{s}_{n\alpha i}} - \frac{\partial \mathcal{L}}{\partial s_{n\alpha i}}. \tag{4.7}$$

Inserting the expressions for T (Eq. 4.3) and the expansion of W (Eq. 4.4) up to second order in s into the Euler-Lagrange equations (Eq. 4.7) yields

$$M_\alpha \frac{d^2 s_{n\alpha i}}{dt^2} = - \sum_{n'\alpha' i'} \Phi_{n\alpha i}^{n'\alpha' i'} s_{n'\alpha' i'}, \tag{4.8}$$

where we make use of the symmetry relation $\Phi_{n\alpha i}^{n'\alpha' i'} = \Phi_{n'\alpha' i'}^{n\alpha i}$. The ansatz

$$s_{n\alpha i}(t) = \frac{1}{\sqrt{M_\alpha}} u_{n\alpha i} e^{-i\omega t} \tag{4.9}$$

leads to

$$\omega^2 u_{n\alpha i} = \sum_{n'\alpha' i'} \frac{\Phi_{n\alpha i}^{n'\alpha' i'}}{\sqrt{M_\alpha M_{\alpha'}}} u_{n'\alpha' i'}, \tag{4.10}$$

which represents an eigenvalue equation for the $3rN$ eigenfrequencies ω. The translational symmetry is accounted for by the ansatz $u_{n\alpha i} = c_{\alpha i} e^{i\vec{q}\vec{R}_n}$ and consequently we obtain

$$\omega^2 c_{\alpha i} = \sum_{\alpha' i'} \underbrace{\left[\sum_{n'} \frac{\Phi_{\alpha i}^{\alpha' i'}(n')}{\sqrt{M_\alpha M_{\alpha'}}} e^{i\vec{q}\vec{R}_{n'}} \right]}_{D_{\alpha' i'}^{\alpha i}(\vec{q})} c_{\alpha' i'}. \tag{4.11}$$

This is a formulation of the equations of motion in terms of an eigenvalue problem with eigenfrequencies ω in $3r$ dimensions, where the dynamical matrix $D_{\alpha' i'}^{\alpha i}(\vec{q})$ is a function of vector $\vec{q}$.

4.3. Calculation of Γ point phonons

For the Γ point phonons ($\vec{q} = 0$) the dynamical matrix writes

$$D_{\alpha' i'}^{\alpha i} = \sum_{n'} \frac{\Phi_{\alpha i}^{\alpha' i'}(n')}{\sqrt{M_\alpha M_{\alpha'}}}. \tag{4.12}$$

Since for $\vec{q} = 0$ the displacements $s_{n\alpha i}$ are the same for all unit cells, the equation of motion becomes

$$M_\alpha \frac{d^2 s_{n\alpha i}}{dt^2} = -\sum_{\alpha' i'} \left[\sum_{n'} \Phi_{\alpha i}^{\alpha' i'}(n') \right] s_{\alpha' i'} = -\sum_{\alpha' i'} \sqrt{M_\alpha M_{\alpha'}} D_{\alpha' i'}^{\alpha i}(0) s_{\alpha' i'} \tag{4.13}$$

The phonon frequencies are now given as the square root of the eigenvalues d of $D_{\alpha' i'}^{\alpha i}$, $\omega_\zeta = \sqrt{d_\zeta}$, where ζ is the index of the eigenmode. The eigenvectors $\vec{e_\zeta}$, in turn, represent the displacement u_α of each atom in an eigenmode in the form $\vec{e}_{\alpha\zeta} = \sqrt{M_\alpha} u_\alpha^\zeta$.

In terms of the ab-initio calculations, the force constants $\Phi_{\alpha' i'}^{\alpha i}$ and consequently also the dynamical matrices $D_{\alpha' i'}^{\alpha i}$ can be determined by calculating the forces acting on all atoms due to the displacement of one atom in one direction. The results can be improved by calculating several displacements for each degree of freedom and fitting $\frac{\partial F_{\alpha i}}{\partial s_{\alpha' i'}}$. Details of the fitting procedure can be found in Ref. [81].

4.4. Theory of raman Scattering

The aim of this section is to describe a method how to calculate Raman spectra from observables which can be directly obtained from frozen phonon ab-initio band structure calculations. More concretely, the calculated quantities are the total energies per unit cell and the complex dielectric tensor, which both change as a function of atomic displacements in the unit cell. A theoretical background of phononic Raman scattering in solids is given e.g. in references [83, 84, 85], while the derivation of the expression for the Raman intensity as derived here is based on Refs. [86, 87, 88].

4.4.1. General remarks on Raman spectroscopy

Raman scattering involves the interaction of light with the atoms of a molecule or solid where the light is inelastically scattered and thus its frequency is changed. In the case of phonon Raman scattering, the difference in energy is due to the interaction with a phonon, i.e. a vibrational degree of freedom. In detail, the interaction of the light with the solid is due to a change of polarizability induced by phononic distortions. In principle, three types of scattered light are measured:

- One part of the light that is elastically scattered and keeps its frequency.
- A part of the photons will excite phononic degrees of freedom and give rise to atomic vibrations (Stokes scattering), thus losing part of their energy resulting in a lower frequency.
- Some of the incoming photons will *absorb* the energy of a phonon and experience an increase of their frequency (anti-Stokes scattering).

Among these three possibilities, the first one has by far the highest probability, which means that the intensity of the inelastically scattered light is very small compared to the initial beam. Since approximately only 1 in 10^7 photons is scattered and thus the intensity of the scattered photons may be as low as 10 to 100 photons per second, often a phonon counting system is used in experiment. On the other hand, in most of the cases a Stokes process is more probable than an anti-Stokes scattering, because an anti-Stokes process requires atoms to occupy excited states, and under normal conditions the number of atoms occupying an excited vibrational state is by far smaller than the number of atoms in the ground state. However, the absolute value of the change in energy is the same for Stokes and anti-Stokes processes, and therefore the Raman spectrum is symmetric relative to the Rayleigh band.

In terms of the possible $\vec{q}$ vectors, which are defined as the difference in $\vec{k}$ between the incoming and the scattered light, $\vec{q} = \vec{k_i} - \vec{k_s}$, only very small absolute values of $|\vec{q}|$ are possible in a Raman process. In Raman experiments $\vec{k_i}$ of the

order 10^5 cm^{-1}, which is very small compared to the Brillouin zone size of about $\frac{2\pi}{a} \approx 10^9$ cm^{-1}. The maximal value of q is found for back scattering with a scattering angle of 180°, $q_{max} = 2k_i$. For this reason, Raman scattering mostly involves the phonons at the center of the Brillouin zone, the Γ point phonons.

4.4.2. Formalism

Quantum-mechanically, the theoretical determination of the Raman efficiency S is based on the calculation of the expectation value of the fluctuations in the dielectric function, caused by transitions between the eigenstates $|i\rangle$ and $|f\rangle$, i.e.

$$\left\langle \delta\varepsilon^{\eta\xi}, \delta\varepsilon^{\eta\xi *} \right\rangle = \left| \left[\varepsilon^{\eta\xi}_{i\to f} \right] \right|_{\omega_s = \omega_L - \omega_{if}} . \tag{4.14}$$

Here, $\varepsilon^{\eta\xi}$ denotes the complex dielectric tensor, ω_S the frequency of the scattered light, ω_L the incoming laser frequency, and ω_{if} the frequency of the phonon that absorbed/emitted the considered energy difference. In order to evaluate this expression, an expansion of the dielectric tensor with respect to phonon displacements $Q_{\omega_{\vec{k}}}$ (see Eq. .5.12) is needed:

$$\varepsilon^{\eta\xi}_{\omega_L}(Q_{\omega_{\vec{k}}}) = \varepsilon^{\eta\xi}_{\omega_L}\big|_0 + \sum_{\omega(\vec{k})} \frac{\partial \varepsilon^{\eta\xi}_{\omega_L}}{\partial Q_{\omega_{\vec{k}}}}\bigg|_0 Q_{\omega_{\vec{k}}} + \frac{1}{2}\sum_{\omega(\vec{k})}\sum_{\omega'(\vec{k'})} \frac{\partial^2 \varepsilon^{\eta\xi}_{\omega_L}}{\partial Q_{\omega_{\vec{k}}} \partial Q_{\omega'_{\vec{k'}}}}\bigg|_0 Q_{\omega_{\vec{k}}} Q_{\omega'_{\vec{k'}}} + \ldots \tag{4.15}$$

Now we assume that the transition between the many-body eigenstates $|i\rangle$ and $|f\rangle$ affects only the phononic subsystem, presuming that the system can be split into states $|\mu\rangle$ and $|\nu\rangle$ depending on eigenvector displacements Q, whereas the state $|g\rangle$ does not dependent on phononic distortions (Condon approximation). Although the Condon approximation does not really require the Born-Oppenheimer approximation, Born-Oppenheimer naturally satisfies it. Thus we obtain

$$\begin{aligned}
&\left[\varepsilon^{\eta\xi}_{i\to f}\right]_{\omega_s} = \left\langle f \left| \hat{\varepsilon}^{\eta\xi}_{\omega_L} \right| i \right\rangle \\
&= \sum_n \frac{1}{n} \sum_{\omega(\vec{k})} \ldots \sum_{\omega^{(n)}_{\vec{k}}(\vec{k}^{(n)})} \left\langle g\mu \left| \frac{\partial^n \hat{\varepsilon}^{\eta\xi}_{\omega_L}}{\partial Q_{\omega_{\vec{k}}} \ldots Q_{\omega^{(n)}_{\vec{k}^{(n)}}}} \hat{Q}_{\omega_{\vec{k}}} \ldots \hat{Q}_{\omega^{(n)}_{\vec{k}^{(n)}}} \right| g\nu \right\rangle_{\omega_S = \omega_L - \omega_{\mu\nu}} \\
&\sim \sum_n \frac{1}{n} \sum_{\omega(\vec{k})} \ldots \sum_{\omega^{(n)}_{\vec{k}}(\vec{k}^{(n)})} \left\langle g \left| \frac{\partial^n \hat{\varepsilon}^{\eta\xi}_{\omega_L}}{\partial Q_{\omega_{\vec{k}}} \ldots Q_{\omega^{(n)}_{\vec{k}^{(n)}}}} \right| g \right\rangle \left\langle \mu \left| \hat{Q}_{\omega_{\vec{k}}} \ldots \hat{Q}_{\omega^{(n)}_{\vec{k}^{(n)}}} \right| \nu \right\rangle_{\omega_S = \omega_L - \omega_{\mu\nu}} \\
&\sim \sum_n \frac{1}{n} \sum_{\omega(\vec{k})} \ldots \sum_{\omega^{(n)}_{\vec{k}}(\vec{k}^{(n)})} \frac{\partial^n \varepsilon^{\eta\xi}_{\omega_L}}{\partial Q_{\omega_{\vec{k}}} \ldots Q_{\omega^{(n)}_{\vec{k}^{(n)}}}} \left\langle \mu \left| \hat{Q}_{\omega_{\vec{k}}} \ldots \hat{Q}_{\omega^{(n)}_{\vec{k}^{(n)}}} \right| \nu \right\rangle_{\omega_S = \omega_L - \omega_{\mu\nu}} .
\end{aligned} \tag{4.16}$$

In this expression, the phononic part ($|\mu\rangle$, $|\nu\rangle$) and the electronic part ($|g\rangle$) of the matrix element can be calculated separately.

Considering only one phononic branch $\omega(\vec{k})$, Eq. 4.16 can be further split into one-, two-, three-, four-phononic contributions, etc. All of them must fulfill the condition of the moment transfer to be zero ($\Delta\vec{k} = 0$), as needed for light scattering in solids:

$$\begin{aligned}
\left[\varepsilon_{i\to f}^{\eta\xi}\right]_{\omega_s}^{(1)} &= \frac{\partial\varepsilon_{\omega_L}^{\eta\xi}}{\partial Q_0}\langle\mu|\hat{Q}_0|\nu\rangle + \frac{1}{2}\frac{\partial^2\varepsilon_{\omega_L}^{\eta\xi}}{\partial Q_0^2}\langle\mu|\hat{Q}_0^2|\nu\rangle + \frac{1}{6}\frac{\partial^3\varepsilon_{\omega_L}^{\eta\xi}}{\partial Q_0^3}\langle\mu|\hat{Q}_0^3|\nu\rangle + \ ... \\
\left[\varepsilon_{i\to f}^{\eta\xi}\right]_{\omega_s}^{(2)} &= \sum_{\vec{k}\neq 0}\{\frac{1}{2}\frac{\partial^2\varepsilon_{\omega_L}^{\eta\xi}}{\partial Q_{\vec{k}}\partial Q_{-\vec{k}}}\langle\mu|\hat{Q}_{\vec{k}}\hat{Q}_{-\vec{k}}|\nu\rangle + \frac{1}{24}\frac{\partial^4\varepsilon_{\omega_L}^{\eta\xi}}{\partial^2 Q_{\vec{k}}\partial^2 Q_{-\vec{k}}}\langle\mu|\hat{Q}_{\vec{k}}^2\hat{Q}_{-\vec{k}}^2|\nu\rangle + ...\} \\
..... &\quad etc.
\end{aligned} \tag{4.17}$$

In our calculations, the derivatives of the dielectric function have been obtained by a fit of the change of $\varepsilon_{\omega_L}^{\eta\xi}$ for displacements along the phonon eigenvectors, where ω_L was in an energy range between 0 and 5 eV.

The total Raman efficiency is obtained by the thermal average of intensity contributions of all possible transitions:

$$S_{\omega_s}^{\alpha\beta} = \frac{NV_E\omega_L\omega_S^3\sum_\mu e^{-E_\mu/kT}\sum_\nu\sum_n\left|\left[\varepsilon_{\mu\to\nu}^{\alpha\beta}\right]^{(n)}\right|^2}{(4\pi^2)c^4\sum_\mu e^{-E_\mu/kT}} \tag{4.18}$$

Eq. 4.18 represents the integrated line intensity of the observed Raman spectrum. In order to obtain an expression directly comparable to experiment, the life-time broadening has to be taken into account, which can be realized by introducing a Lorentzian term $L^{(n)}$. This way one obtains the spectral density

$$\frac{\partial S_{\omega_s=\omega_L-\omega}^{\alpha\beta}}{\partial\omega}(\omega) = \frac{NV_E(\omega_L-\omega)^3\sum_\mu e^{-E_\mu/kT}\sum_\nu\sum_n\left|\left[\varepsilon_{\mu\to\nu}^{\alpha\beta}\right]^{(n)}\right|^2 L^{(n)}(\omega,\omega_{\mu\nu},\gamma)}{(4\pi^2)c^4\sum_\mu e^{-E_\mu/kT}} \tag{4.19}$$

5. Model parameters

In the first section of the present chapter, the determination of electron-phonon and spin-phonon coupling parameters is explained. Since this method involves the mapping of the theoretical band structure onto a tight-binding model, in the first part of the corresponding section this mapping procedure will be described. In the second section, the formalism for the calculation of Raman spectra based on ab-initio calculations will be presented.

5.1. Hopping parameters

In order to extract hopping parameters from the theoretical band structure, the bonding and anti-bonding pair of the V $3d_{xy}$ bands at the Fermi level and the two highest lying valence bands with O $2p$ character are mapped onto a tight-binding model. It takes into account:

- $t_{\parallel}$, the hopping along to the ladder
- $t_{\perp}$, the hopping perpendicular to the ladder (in-rung)
- t_i, which represents the inter-ladder hopping, i.e. the hopping between the V atoms of two neighboring ladders

In this context, we restrict ourselves to the direction in $\vec{k}$ space corresponding to this model, i.e. $\vec{k} \parallel y$. Idealizing the situation, one can assume that both, the bands VB1 and VB2 (Fig. 5.1) and the conduction bands next higher in energy, CB1 and CB2, are exclusively formed by d_{xy} orbitals. This is true in very good approximation for VB1 and VB2, the two bands around E_F, while in CB1 and CB2 some contribution from V $3d_{yz}$ states together with some O1 and O3 $2p_y$ character is present (see Sect. 8.1).

In this scenario, the dispersion of the bands at E_F is given by

$$\varepsilon_{1,2}(k) = \varepsilon_V - t_{\perp} + 2t_{\parallel} \cos k \pm t_i \cos \frac{k}{2}. \tag{5.1}$$

Here ε_V represents the site energy of the d_{xy} states, $t_{\parallel}$ is the hopping along the ladder, $t_{\perp}$ is the in-rung hopping perpendicular to the ladder (in-rung), and t_i is the inter-ladder hopping. In this formula, the lattice constant is assumed to be 1. The different phase related to t_i is due to the fact that the electron of one

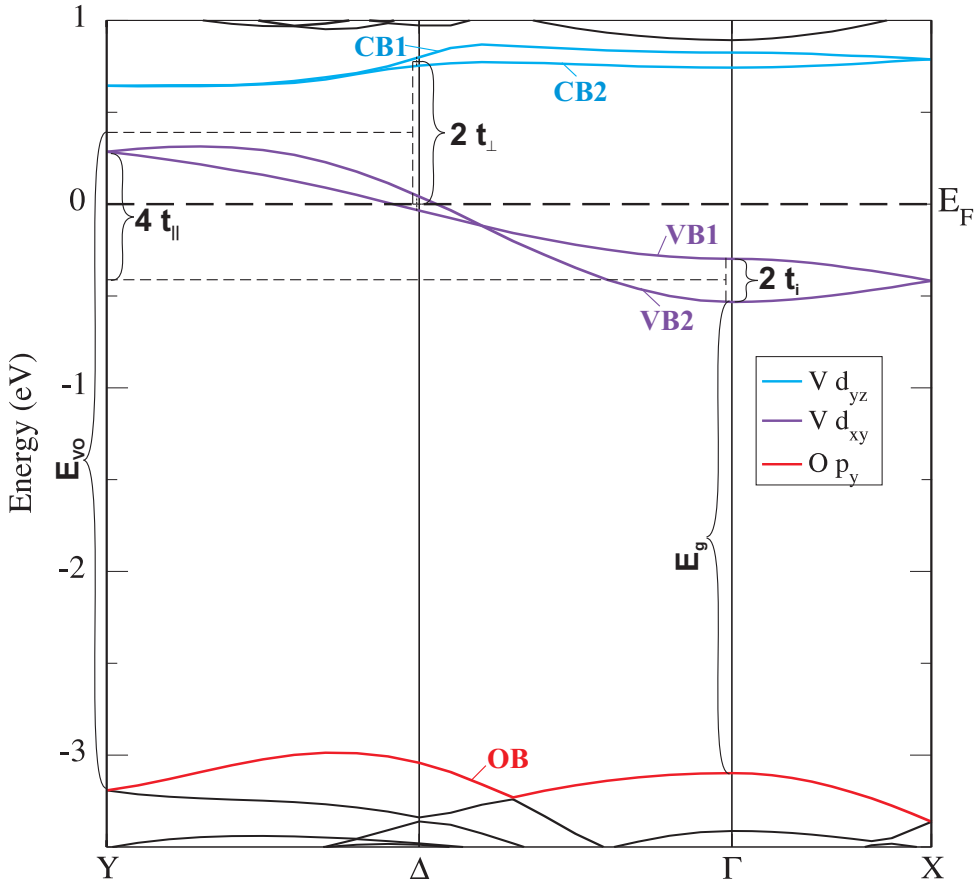

Figure 5.1.: Schematic representation of the hopping matrix elements, the charge transfer gap E_g, and E_{VO}, the difference in energy between the O $2p$ valence bands and the V d_{xy} states around E_F. Exemplarily, the band structure of NaV_2O_5 is used for this figure. The details are explained in the text.

rung interacts with one rung from its present unit cell at, $y = +1/2$, and with one rung of the previous unit cell, at $y = -1/2$. Adding the two corresponding terms, $e^{ik(+1/2)} + e^{ik(-1/2)}$, the result is proportional to $\cos(k/2)$.

Setting $k = 0$ and adding the expressions for ε_1 and ε_2, respectively, one readily obtains

$$t_i = \frac{1}{2}\left(\varepsilon_1(0) - \varepsilon_2(0)\right). \tag{5.2}$$

Furthermore we expect that $t_\perp > t_\parallel \gg t_i$. Making use of the second part of this inequality, $t_\parallel \gg t_i$, and subtracting the expressions for $k = 0$ and $k = \pi$, one obtains

$$t_\parallel = \frac{1}{4}\left(\varepsilon_1(0) - \varepsilon_1(\pi)\right), \tag{5.3}$$

as it is shown in Fig. 5.1.

The same relation holds when substituting ε_1 by ε_2, such that we take the average of the two values at Γ, while at the Y point the two bands are degenerate anyway. This gives

$$t_{\parallel} = \frac{1}{4}\left(\frac{1}{2}\left[\varepsilon_1(0) + \varepsilon_2(0)\right] - \varepsilon_1(\pi)\right), \tag{5.4}$$

as it is again visualized in Fig. 5.1.

In a similar way, it can be demonstrated that

$$\varepsilon_V - t_{\perp} = \frac{1}{2}\left[\varepsilon_1(\pi/2) + \varepsilon_2(\pi/2)\right]. \tag{5.5}$$

Now let us turn to the conduction bands called CB1 and CB2. Even though these bands have a non-vanishing admixture of other states, we will apply the same model. where we label quantities referring to these conduction bands using the superscript C:

$$\varepsilon^C_{1,2}(k) = \varepsilon_V + t_{\perp} + 2t^C_{\parallel}\cos k \pm t^C_i \cos\frac{k}{2} \tag{5.6}$$

If we take the $k = \Delta = \pi/2$ point, the $t^C_{\parallel}$ -related term vanishes, and we obtain

$$\varepsilon_V + t_{\perp} = \frac{1}{2}\left(\varepsilon^C_1(\pi/2) + \varepsilon^C_2(\pi/2)\right) \tag{5.7}$$

Therefore,

$$\varepsilon_V = \frac{1}{4}\left[\varepsilon^C_1(\pi/2) + \varepsilon^C_2(\pi/2) + \varepsilon_1(\pi/2) + \varepsilon_2(\pi/2)\right], \tag{5.8}$$

and consequently we obtain (see Fig. 5.1)

$$t_{\perp} = \frac{1}{2}\left[\varepsilon^C_1(\pi/2) + \varepsilon^C_2(\pi/2) - (\varepsilon_1(\pi/2) + \varepsilon_2(\pi/2))\right] \tag{5.9}$$

Therefore, the energy difference E_{VO} between O and V orbitals should be determined at the $k = \pi/2$ point, but one can use E_g for this purpose also.

5.2. Exchange matrix elements

Now we want to determine the exchange parameters $J_{\perp}$ and $J_{\parallel}$ [89], where $J_{\parallel}$ is the interaction between the spins on the nearest-neighbor rungs and $J_{\perp}$ represents the exchange along *one* rung. First we will consider $J_{\parallel}$. In order to be able to interact, the spins of the neighboring rungs must be brought to the same orbital, which in this case is the orbital of the in-leg oxygen O2. Since the process is virtual, one has to bring them back to their original V orbitals again. Thus, the considered process corresponds to a fourth-order perturbation. Due to the Pauli

principle this process is only allowed if the two electrons form a singlet, while for the triplet state it is forbidden. The respective correction to the energy that selects the spin-singlet and spin-triplet states energies is of the order of t_{VO}^4/E_{VO}^3, where t_{VO} is the hopping matrix element between V and the O2 in the same leg, and E_{VO} is the energy separating the V states from the oxygen states about 3 eV below E_F (labeled as OB in Fig. 5.1). To be consistent with the result for $t_\parallel$, E_{VO} is taken at the Y point, $k = \pi/2$.

Let us now have a closer look at $t_\parallel$. The hopping matrix element $t_\parallel$ brings an electron from one rung to the nearest-neighbor rung via an in-leg oxygen orbital, which is realized in two hopping steps. This is the second-order process giving $t_\parallel \sim t_{VO}^2/E_{VO}$, and therefore

$$J_\parallel \propto t_\parallel^2/E_{VO}. \tag{5.10}$$

Here, alternatively E_{VO} may be substituted by E_g, the gap between the V $3d_{xy}$ bands and the O $2p$ bands at the Γ point.

The derivation of $J_\perp$ can be accomplished in an analogous way, giving

$$J_\perp \propto t_\perp^2/E_{VO}. \tag{5.11}$$

5.3. Electron-phonon and spin-phonon coupling parameters

In order to obtain electron-phonon and spin-phonon coupling parameters the electronic bands for structures with the atoms displacement along the eigenvector of a phonon mode is computed. Comparing the hopping parameters $t_\parallel$, $t_\perp$, and t_i extracted from this band structure to the ones obtained from the undistorted system, the coupling of each matrix element to the lattice may be determined by calculating $\delta t_\sigma/\delta Q$ ($t_\sigma \in \{t_\parallel, t_\perp, t_i\}$). In this context, Q represents a dimensionless displacement factor related to the atomic displacements along a certain phonon eigenvector $\vec{e}_\zeta$. It is defined through the relation

$$Q\sqrt{\frac{\hbar}{M_\alpha \omega_\zeta}}\vec{e}_{\alpha\zeta} = \vec{u}_\zeta^{\,\alpha}, \tag{5.12}$$

where α denotes an atom involved in the eigenmode, M_α is its mass, ζ is the index of the eigenmode, $\vec{e}_{\alpha\zeta}$ the corresponding eigenvector and $\vec{u}_\zeta^{\,\alpha}$ the related displacement. Since $\vec{u}_\zeta^{\,\alpha}$ is proportional to $\vec{e}_{\alpha\zeta}/\sqrt{M_\alpha}$, Q is the same for all α, i.e. it is independent from the choice of the atom.

For the exchange integrals $J_\parallel$ and $J_\perp$, instead of $\delta J_\sigma/\delta Q$ ($J_\sigma \in \{J_\parallel, J_\perp\}$), the quantity $\delta J_\sigma/J_\sigma/\delta Q$ is considered. Since $J_\sigma \propto t_\sigma^2/E_{VO}$ (Eq. 5.10) one finds

$$\frac{\delta J_\sigma}{J_\sigma} \propto \frac{\delta\left(t_\sigma^2/E_{VO}\right)}{t_\sigma^2/E_{VO}} = \frac{E_{VO}}{t_\sigma^2}\left(\frac{2t_\sigma \delta t_\sigma}{E_{VO}} - \frac{t_\sigma^2 \delta E_{VO}}{E_{VO}^2}\right) = \frac{2\delta t_\sigma}{t_\sigma} - \frac{\delta E_{VO}}{E_{VO}}. \tag{5.13}$$

5.4. Hubbard U

The Hubbard parameters U, representing the on-site Coulomb repulsion, can be estimated from the band structure considering the change in the V bands due to adding a small amount of positive charge to the system. More precisely, the change in the difference between the energy of the lower bonding V $3d_{xy}$ band just below the Fermi energy (VB2 in Fig. 5.1), and the highest of the O $2p$ valence bands (OB) is considered. The additional charge can either be added to the site of the metal ion (Na, Ca), as described in Ref. [32], or it can be provided in the form of a uniform positive background. In both cases the change in the gap between VB1 and OB also depends on the point in *veck* space, where for the second case, in our experience, a more uniform change of the gap throughout the Brillouin zone is found.

Part II.

Results

6. Raman–active Phonon Modes

6.1. A_g modes

6.1.1. NaV_2O_5

Theory	Experiment							
	Ref. [90]	Ref. [7]	Ref. [91]	Ref. [37]	Ref. [36]	Ref. [19]	Ref. [16]	Ref. [92]
996	970	971	969	969	970	969	970	969
512	531	530	536	534	533	535	530	533
467	449	449	452	448	447	450	450	445
414	421	420	424	423	420	420	422	422
308	300	304	306	304	301	305	304	300
232	231	230	234	233	233	231	230	234
176	175	178	179	179	177	179	178	177
111	89	88	90	90	90	89	90	–

ω	Eigenvector								Assignment	
	V_x	V_z	Na_z	$O1_z$	$O2_x$	$O2_z$	$O3_x$	$O3_z$	Refs. [37]	This work
996	0.04	0.25	-0.01	0.01	0.01	-0.00	-0.05	-0.43	V-O3 stretch.	V-O3 stretch.
512	0.16	-0.07	0.01	0.16	0.45	0.06	-0.05	-0.01	V-O2 stretch.	V-O2 stretch.
467	0.42	-0.06	0.01	0.15	-0.21	-0.05	-0.11	0.01	V-O1-V bend.	V-O1-V bend.
414	-0.19	-0.17	0.00	0.44	-0.08	-0.18	0.18	-0.14	O-V-O bend.	$O1_z$+O3-V-O2 bend.
308	0.02	0.19	-0.04	0.18	-0.07	0.39	0.19	0.09	O-V-O bend.	O3-V-O2 bend.
232	0.17	0.06	0.03	-0.13	0.06	-0.16	0.42	0.00	O-V-O bend.	O3-V-O2 bend.
176	-0.02	0.28	-0.40	0.10	0.04	-0.22	-0.06	0.18	Na‖c	Na‖c
111	-0.04	0.30	0.42	0.13	0.03	-0.16	-0.08	0.18	chain rot.	chain rot.

Table 6.1.: Upper table: Calculated eigenfrequencies (cm^{-1}) of the A_g phonon modes of NaV_2O_5 compared to experimental results from literature. Lower table: Theoretical eigenvector components and assignment of the phonon modes compared to the assignment of Ref. [37].

The eigenfrequencies and eigenvectors of the A_g phonon modes of NaV_2O_5 are presented in Table 6.1. Figure 6.1 displays the eigenvectors in terms of arrows, i.e. the length of the arrows is proportional to the real displacement multiplied by the square root of the related atomic mass, $|\vec{e}_{\alpha\zeta}| = \sqrt{M_\alpha}\,|u^\zeta_\alpha|$. Let us first focus on the experimental assignment. In Ref. [90], published in 1997, the Raman spectra were interpreted in terms of the space group $P2_1mn$. Accordingly a total of 15 Raman active modes in parallel polarization were expected, and

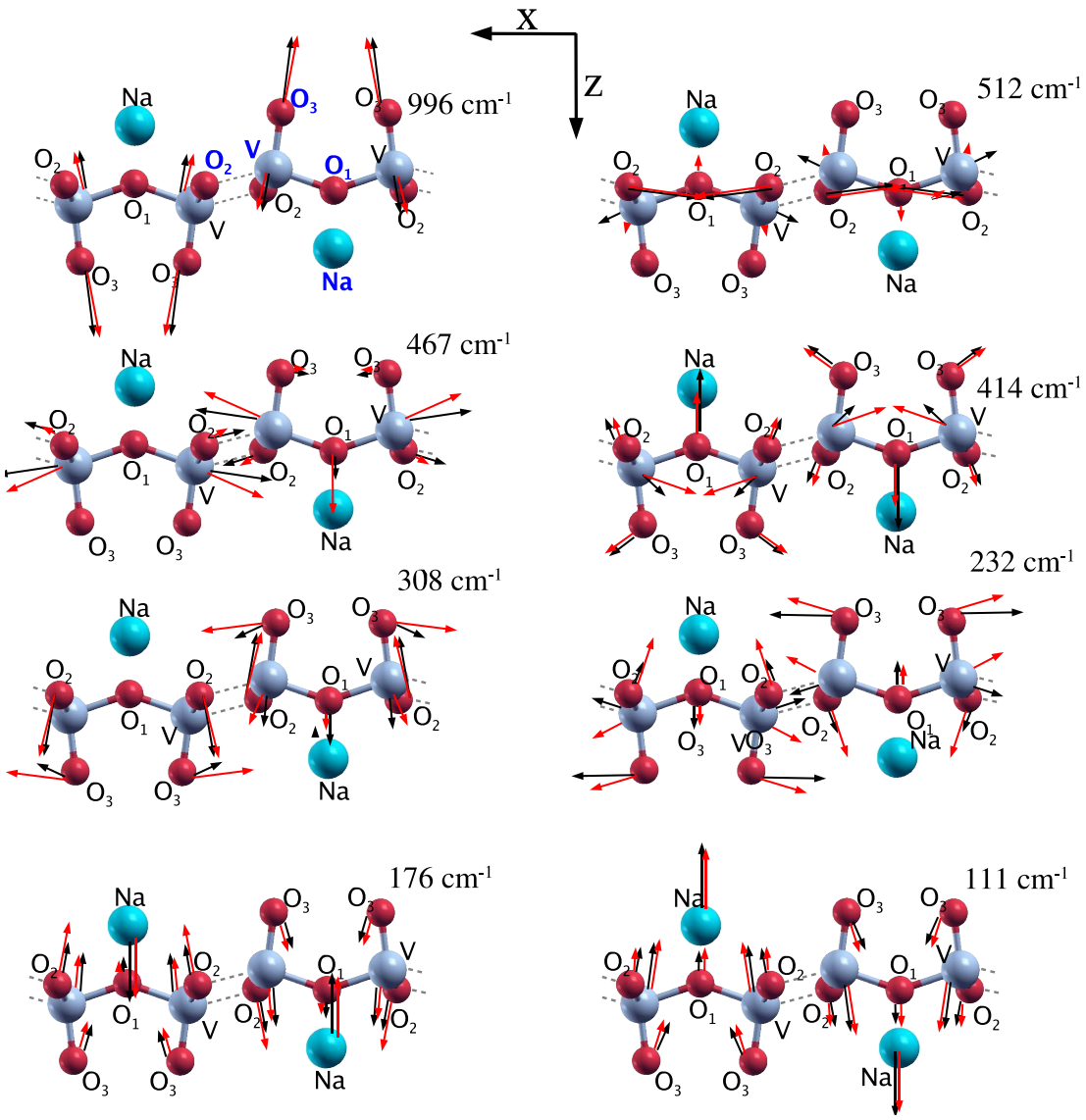

Figure 6.1.: A_g phonons of NaV_2O_5 (black arrows) and CaV_2O_5 (red arrows), respectively. The frequencies correspond to the ones of NaV_2O_5. The arrows show the direction and magnitude of the atomic displacements for each eigenmode.

in fact 12 different frequencies were reported. Since 1998 literature data have consistently been discussed within space group *Pmmn* (no. 59), were Raman measurements (Ref. [91]) have contributed to clarify the situation. Thus, the frequencies presented in Table 6.1 assume the latter space group, where a selection of eight frequencies from Ref. [90]) is based on the comparison with more recent experimental results.

The theoretically obtained frequencies agree very well with their experimental counterparts with overall deviations between 0.5 and 3.5%. Only for the eigen-

mode lowest in frequency the discrepancy is greater. Conforming with Ref. [37] the eigenvector of the 996 cm^{-1} mode represents a stretching of the distance between V and the apical oxygen, which is visualized by the black arrows in Fig. 6.1. In the 512 cm^{-1} mode[1] the O2 atoms of the two legs of one ladder oscillate symmetrically with respect to the ladder's center, while the neighboring V atoms on the same leg move against the former with considerably smaller amplitude. Thus the experimental assignment of Ref. [37], identifying this mode as V–O2 stretching is verified, apart from an additional $O1_z$ motion found in theory. In the same way, the assignment of the 467 cm^{-1} mode, interpreted as a V–O1–V bending in Ref. [37], is verified, where we, however, also find admixtures of an $O2_x$ movement. In the eigenvector of the 414 cm^{-1} vibration, the z-displacement of the in-rung oxygen O1 is dominating, while this mode is described as pure O3–V–O2 bending in Ref. [37]. At the same time, our theoretical frequency is much closer to experiment (2% deviation) than the one calculated in Ref. [39] (9% difference). For the 308 cm^{-1}, the 232 cm^{-1}, the 176 cm^{-1} and the 111 cm^{-1} modes, the agreement of our results with the assignment of Popovic *et al.* [37] is good. However, in most of these modes we find a more pronounced involvement of O1.

6.1.2. CaV_2O_5

Table 6.2 shows the A_g eigenmodes of CaV_2O_5, while the displacement patterns are included in Fig. 6.1. The experimental situation turns out to be rather confusing and to some extent contradictory regarding the classification of modes with respect to their symmetry. The first publication about Raman spectra of CaV_2O_5 (Ref. [93]) presents polarized spectra for a *polycrystalline* sample, which where measured in three different geometries, labeled as HH, VV, and HV. Taking into account the details of the experiment as given in this reference, the presented assignment has to be considered as a tentative one, since the polarization of the applied laser with respect to the orientation of the crystal axes is not known. This means, that e.g. the HH polarization does not correspond to xx, yy, or zz polarization, but instead it is oriented in an arbitrary direction with respect to the crystal axes. Thus, B_{ng} peaks appear in the HH or VV spectra, while contributions of A_g modes are found in the HV results. Theoretically obtained Raman results allow a more precise interpretation of the experimental spectra. They will be presented in Chap. 9, but some results will be used throughout the present chapter whenever they are helpful for the assignment of modes. They show, that the intensity of the A_g peaks is one order of magnitude larger than the one of the B_{ng} spectra, which implies that in the spectra in Ref. [93] obtained with parallel polarization (HH and VV, respectively), the contribution of A_g modes must be dominant. This means that the A_g modes can be distinguished rather clearly in

[1] If not explicitly mentioned, in the following sections frequencies refer to the *theoretical* results

Theory	Experiment			
	Ref. [93]	Ref. [94]*	Ref. [39]*	Ref. [39]
900	935	932	932	932
516	542	539	539	539
446	472	470	470	470
412	421	418	422	422
307	337	335	334	?
265	282	281	280	235.6
201	238	236	235.6	138.6
106	91	90	90	90

ω	Eigenvector								Assignment	
	V_x	V_z	Ca_z	$O1_z$	$O2_x$	$O2_z$	$O3_x$	$O3_z$	Ref. [39]	This work
900	0.06	0.24	-0.01	0.02	0.02	-0.02	-0.08	-0.42	V-O3 stretch.	V-O3 stretch.
516	-0.01	-0.05	0.01	0.11	0.49	0.07	-0.02	0.00	V-O2 stretch.	V-O2 stretch.
446	0.36	-0.16	-0.00	0.39	-0.09	-0.05	-0.08	-0.00	V-O1-V bend.	V-O1-V bend.
412	-0.34	-0.12	-0.02	0.27	-0.05	-0.17	0.18	-0.13	O-V-O bend.	$O1_z$+O3-V-O2 bend.
307	0.09	0.20	-0.07	0.10	-0.01	0.20	0.39	0.05	O-V-O bend.	O3-V-O2 bend.
265	0.19	-0.10	0.14	-0.18	0.09	-0.31	0.25	-0.08	O-V-O bend.	O3-V-O2 bend.
201	0.02	0.21	-0.39	0.03	0.06	-0.31	-0.05	0.17	Ca‖c	Ca‖ c
106	-0.05	0.32	0.39	0.15	0.01	-0.15	-0.06	0.19	chain rot.	chain rot.

Table 6.2.: Upper table: Calculated eigenfrequencies (cm^{-1}) of the A_g phonon modes of CaV_2O_5 compared to experimental results from literature. Lower table: Theoretical eigenvector components and assignment of the phonon modes compared to the assignment of Ref. [39]. Details are explained in the text.

experiment, even if detailed classification into xx, yy, and zz polarization is not possible. At the same time, the results obtained from HV polarization can not uniquely be assigned to B_{1g}, B_{2g}, or B_{3g} symmetry.

The frequencies of columns two and three marked with * were chosen from the unpolarized spectra in Refs. [39] and [94] due to the comparison with the polarized spectra of Ref. [93] and the theoretical Raman spectra. In contrast, column four corresponds to the original assignment, which was done by comparing the unpolarized spectra exclusively with the polarized results for NaV_2O_5.

For the eigenfrequencies above 400 cm^{-1}, the agreement between theory and experiment [39] is very good. For these vibrations, the experimental assignment with respect to their symmetry is unambiguous. The lower frequency of the apical oxygen vibration in CaV_2O_5 compared to NaV_2O_5 is due to larger interionic distances, and hence, smaller force constants. A change of 5% can be estimated within the simple Coulomb picture from the different Vanadium charges in NaV_2O_5 and CaV_2O_5 (i.e. 4.5 and 4, respectively), which is in qualitative agreement with experiment. For the V–O2 stretching mode, in contrast, the

frequency in CaV_2O_5 hardly differs from the one in NaV_2O_5. In both materials the O2 component is very dominant in the eigenvector (Fig. 6.1), while there is a much smaller contribution of the V atoms, and the rest of the atoms hardly contribute at all. In CaV_2O_5, the V component of the eigenvector is still considerably smaller than in NaV_2O_5, such that the eigenmode represents almost a pure oscillation of the O2 subsystem. In comparison with NaV_2O_5, neither the metal atom with its different mass nor the V ion with its altered charge plays a role in this eigenmode, which explains why the frequencies are so close to each other.

In both, the 446 cm^{-1} and the 412 cm^{-1} modes, representing a V–O1–V and a $O1_z$+O3–V–O2 bending, respectively, the O1 participation is considerably stronger than in NaV_2O_5, at the expense of the V displacement. Moreover, the V movements have a larger z–component, reflecting the smaller V–O1–V angle in the Ca compound. Again the results of both materials are close to each other in terms of frequency.

The symmetry assignment of the phonon modes between 180–350 cm^{-1} is considered as a tentative one in Ref. [39], arguing that only single-crystal measurements can resolve different symmetry modes in this spectral region. In this context, the interpretation of the Raman scattering intensities as presented in Section 9.2 together with the polarized spectra presented in Ref. [93] are helpful for an unambiguous assignment. As reported in Ref. [93], but not correspondingly interpreted in Refs. [39] and [94], respectively, theory clearly shows that the mode somewhat above 300 cm^{-1} has got A_g symmetry. In fact, this O3–V–O2 bending mode is very similar to a mode of NaV_2O_5, both in the frequency and the eigenvector components. The main deviation from the NaV_2O_5 mode consists in a somewhat larger contribution from the apex oxygen O3.

The 265 cm^{-1} mode of CaV_2O_5 represents an O3–V–O2 bending as the 232 cm^{-1} vibration of NaV_2O_5, but it slightly differs from the latter. In detail, the $O2_z$ and the Ca_z components of the eigenvector are considerably larger in CaV_2O_5, while for V the direction changes clearly. Instead of oscillating towards the O2 of the neighboring ladder, it moves more parallel to the V–O1 bond, as it is demonstrated in Fig. 6.1. For this reason the V–O1 distance in the CaV_2O_5 eigenmode changes more strongly than in the NaV_2O_5 counterpart, which leads to a higher frequency. Another feature of the CaV_2O_5 mode are considerable eigenvector contributions from O2 and Ca_z. Experimentally, a peak around 280 cm^{-1} can be found in all Refs. [39, 93, 94]. Due to the peaks found in the polarized Raman spectra of NaV_2O_5, which served as the basis for the assignment of the CaV_2O_5 mode, in Ref. [39] the 280 cm^{-1} mode was interpreted as a B_{3g} vibration. Its measured intensity is twice as strong as the one of the 292 cm^{-1} peak. At the same time, the theoretical Raman spectra show that the A_g peak in this frequency range is clearly dominating, while the B_{3g} peak is still one order of magnitude larger than a B_{1g} and a B_{2g} peak close in frequency. For these reasons we suggest that the 280 cm^{-1} peak is the one with A_g symmetry, while the

292 cm^{-1} has B_{3g} character.

The 201 cm^{-1} mode, where Ca oscillates parallel to the c axis, is roughly 20% higher in frequency than in NaV_2O_5, which caused interpretation problems in literature. In Ref. [39], where the assignment of the CaV_2O_5 modes was done in comparison with the phonons of NaV_2O_5, the 138 cm^{-1} mode of the unpolarized spectrum was interpreted as A_g vibration since its frequency compared to that of the (Na ∥ c) mode scales as the inverse square root of the corresponding masses. But in Ref. [93] the 138 cm^{-1} peak appears in crossed polarization, which strongly suggests that it belongs to B_g symmetry, while in parallel polarization there are peaks only at 238 and 282 cm^{-1}. This situation is also verified by the theoretically obtained Raman spectra in Sect. 9.2. The measured 138 cm^{-1} peak turns out to originate from both, a B_{1g} and a B_{2g} eigenmode. The physical origin of the frequency shift of this Ca-dominated oscillation can be related to the larger positive charge—and hence stronger interaction—of the Ca^{2+} ion compared to the Na^+ ion. This increased attraction, which in a simple Coulomb picture implies a frequency shift by +40%, over-compensates the effect of the larger Ca mass, which would lead to a 25% decrease of this frequency.

Regarding the lowest-frequency mode, which represents a chain rotation, theory and experiments perfectly agree in the point that the frequencies for NaV_2O_5 and CaV_2O_5 are almost identical. This implies a stronger inter-ladder interaction in CaV_2O_5 compared to NaV_2O_5, since the mass of Ca and, analogously, the mass of the rotating chain is larger in CaV_2O_5, which by itself would lead to a frequency lowered by about 5%. This enhanced inter-ladder interaction of CaV_2O_5 is also reflected in the larger tight binding parameter t_i (see Tabs. 10.1 and 10.4).

6.1.3. MgV_2O_5

The eigenvectors and eigenfrequencies of MgV_2O_5 are shown in Table 6.3 and Fig. 6.2, respectively. On the experimental side, only unpolarized Raman spectra of MgV_2O_5 are available. In Ref. [93] no assignment of the symmetries is done, therefore the frequencies of column two (marked by *) are selected due to the theoretical frequencies and the theoretical Raman spectra of Chap. 9.3. In Ref. [39], the symmetries are assigned by comparison of the unpolarized MgV_2O_5 spectra with the polarized NaV_2O_5 spectra. The result of this assignment represent the values in column three. Column four (marked by **), in contrast, shows frequencies of the same reference, again selected in the light of the theoretical phonon frequencies and Raman spectra. The V–O3 stretching mode (1019 cm^{-1}) excellently agrees with experiment, and also the assignment is unambiguous. It represents a stretching of the strongest bond, i.e. the bond between V and the apex oxygen O3. Also the 546 cm^{-1} mode is very close to the experimental frequency, but the experimental assignment is not verified. While in NaV_2O_5—which is the reference material for the assignment in Ref. [39]—the mode with the second highest frequency can be identified as a V–O2 stretching, in MgV_2O_5 the

Theory	Experiment		
	Ref. [93]*	Ref. [39]	Ref. [39]**
1019	1001	1002	1002
546	534	536	534
419	413	478	414
395	373	414	374
353	314	?	315
310	278 (299?)	233	278 (300.5?)
250	219	–	220
104	98	98	98

ω	Eigenvector								Assignment	
	V_x	V_z	Mg_z	$O1_z$	$O2_x$	$O2_z$	$O3_x$	$O3_z$	Ref. [39]	This work
1019	0.07	0.23	-0.01	0.01	0.01	0.01	-0.13	-0.42	V-O3 stretch.	V-O3 stretch.
546	-0.13	-0.07	0.01	0.05	0.46	-0.11	-0.02	0.04	V-O2 stretch.	leg ↔ leg
419	0.10	-0.16	-0.13	0.36	-0.11	-0.33	0.12	-0.09	V-O1-V bend.	$O2_z$+V-O1-V bend.
395	-0.33	0.17	-0.17	0.00	-0.05	0.03	0.30	-0.05	O-V-O bend.	Mg_z+O3-V-O2 bend.
353	0.01	0.06	-0.21	0.36	0.06	0.34	-0.16	0.10	O-V-O bend.	O2-V-O1 bend.
310	0.34	0.14	-0.30	-0.15	0.14	-0.03	0.16	0.08	O-V-O bend.	Mg_z+O1-V-O3 bend.
250	-0.17	-0.02	-0.31	-0.15	-0.08	-0.19	-0.34	0.06	Mg‖c	Mg_z+O2-V-O3 bend.
104	0.00	0.37	0.15	0.12	0.01	-0.20	-0.07	0.23	chain rot.	chain rot.

Table 6.3.: Upper table: Calculated eigenfrequencies (cm^{-1}) of the A_g phonon modes of MgV_2O_5 compared to experimental results from literature. Lower table: Theoretical eigenvector components and assignment of the phonon modes compared to the assignment of Ref. [39]. Details are explained in the text.

main feature of the 546 cm^{-1} mode appears to be an in-phase motion of the V and O2 atom of one leg in x direction, while the two legs of one ladder oscillate against each other and the leg of the next neighboring ladder. At the same time, each leg shows a zigzag-like deformation in the x–y plane due to the fact that the O2 atom oscillates more strongly than the V atom. Also for the 419 cm^{-1} mode, the experimental assignment has to be revised. Instead of a pure V–O1–V stretching, which is encountered in NaV_2O_5 and CaV_2O_5, in MgV_2O_5 this mode represents a more complex oscillation, with O2 moving in z direction, out-of-phase with respect to the neighboring V, while O3 has a considerable component parallel to the V motion. Correspondingly, the frequency differs considerably from its counterparts in NaV_2O_5 and CaV_2O_5. The 395 cm^{-1} mode of MgV_2O_5, in turn, is comparable with the $O1_z$+O2–V–O3 mode found in NaV_2O_5 and CaV_2O_5, also consisting in an O2–V–O3 bending. However, the in-rung oxygen O1 hardly participates in this oscillation, while Mg has a considerable z component.

The 353 cm^{-1} mode of MgV_2O_5 represents an out-of-phase oscillation in z direction of the in-rung O1 and the in-leg O2, while the V atoms virtually stay

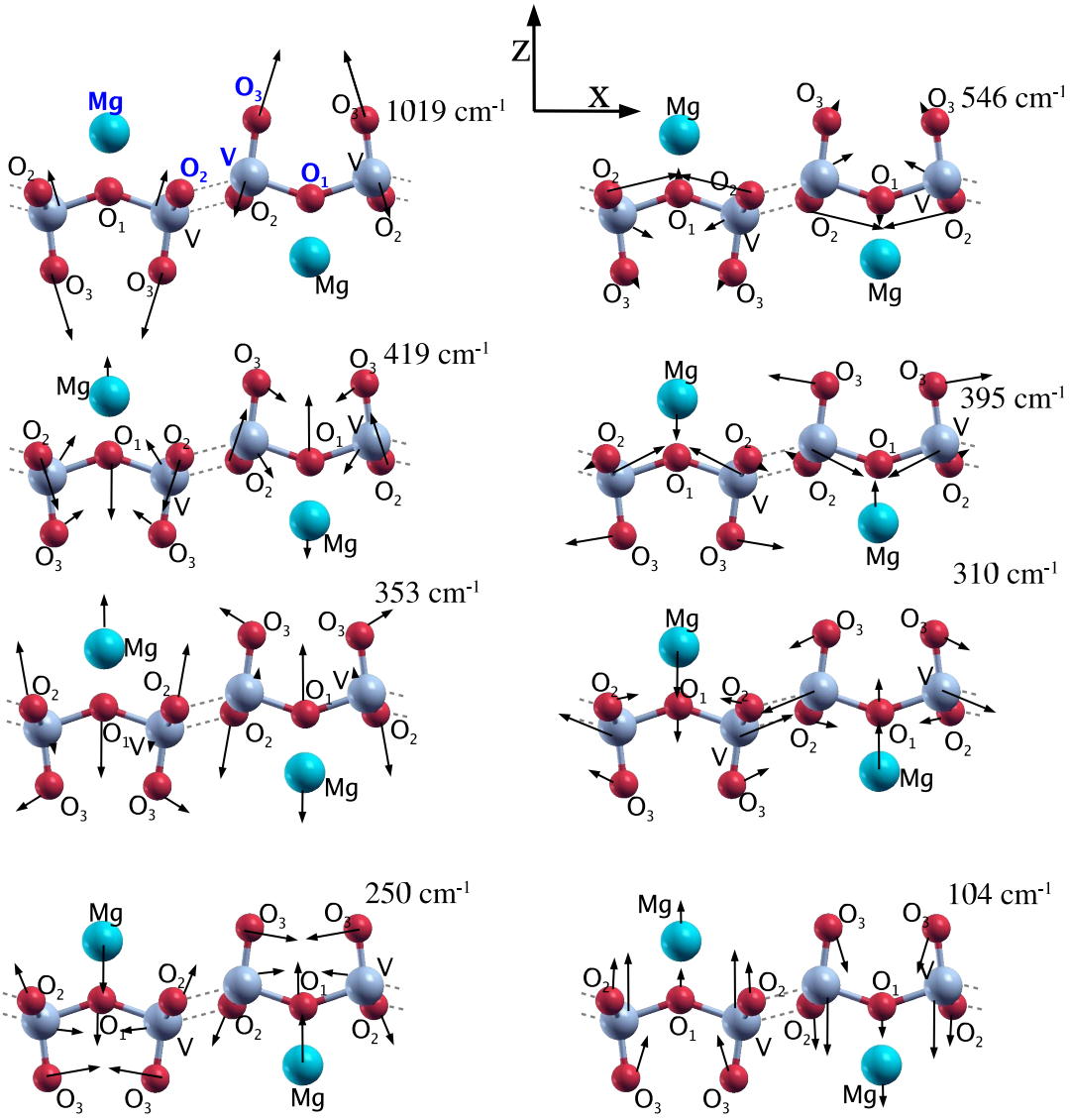

Figure 6.2.: A_g phonons of MgV_2O_5. The arrows show the direction and magnitude of the atomic displacements for each eigenmode.

on their positions. Instead, the Mg atoms vibrate parallel to the O2 atoms of the same ladder, while the eigenvector components of the apex oxygen moving perpendicular to the V–O3 bond is comparably small. The involvement of Mg on the one hand, and the minor participation of O3 and V on the other hand, are the main differences to the corresponding eigenmodes of NaV_2O_5 and CaV_2O_5 at 308 cm^{-1} and 307 cm^{-1}, respectively, which have pronounced O2–V–O3-bending character. In Ref. [39], there is no such A_g mode identified for MgV_2O_5, even though there is a peak found at 315 cm^{-1}. Comparison to the theoretically obtained frequencies and the Raman spectra make it very probable that the peak at 315 cm^{-1} has got A_g symmetry, both, due to its position and its intensity

. Hence this peak was included in column four. The symmetry assignment made in Ref. [39] may have to be revised also for the A_g mode at 310 cm^{-1}. First, the theoretically obtained frequency shows that there must be an A_g mode considerably higher in frequency than 233 cm^{-1}. Second, the Raman spectra presented in Section 9.3 clearly show that the corresponding peak must have strong intensity, while the peak at 233 cm^{-1} in Ref. [39] is rather weak. For this reasons we claim that not the 233 cm^{-1}, but more probably the 278 cm^{-1} peak corresponds to the theoretically found A_g mode at 310 cm^{-1}. Another candidate could be an experimental peak at 300 cm^{-1}, which is closer in frequency, but its low intensity is inconsistent with the theoretical findings and suggests that it may stem from some B_{ng} mode. The 310 cm^{-1} mode represents an O1–V–O3 bending, where Mg oscillates in phase with the apex oxygen O3. Since also the O2 atoms contribute to this eigenmode, it has a certain similarity to the O2–V–O3 bending mode at 232 cm^{-1} (265 cm^{-1}) of NaV_2O_5 (CaV_2O_5). The MgV_2O_5 A_g mode second lowest in frequency at 250 cm^{-1}, in contrast, deviates strongly both in frequency as in the eigenvector components from its counterpart in NaV_2O_5 and CaV_2O_5, respectively. Instead of representing an oscillation of the metal ion against the rest of the ladder, in MgV_2O_5 the Mg ion moves in phase with its nearest neighbor, i.e. the in-leg oxygen O1 (see Fig. 6.2). The most characteristic feature of this mode is a breathing of the pentagon formed by the in-leg oxygen together with the two adjacent V atoms and their apex oxygens, respectively. The O2 atoms, finally, oscillate out of phase with respect to the rest of the ladder. These two features explain the relatively high frequency of this mode.

The assignment of the lowest-frequency mode at 104 cm^{-1}, finally, is unambiguous. Analogous to NaV_2O_5 and CaV_2O_5—and correctly identified in Ref. cm^{-1}Popovic02—it can be described as chain rotation mode, where neighboring ladders oscillate antisymmetrically in z direction. The higher frequency of this oscillation compared to the chain rotation in NaV_2O_5 and CaV_2O_5, which both have experimental frequencies of 90 cm^{-1}, can be explained by the same arguments as used in the discussion of the CaV_2O_5 mode: On the one hand, the inter-ladder interaction is stronger than in NaV_2O_5, which is also reflected in the smaller inter-ladder distance. On the other hand, the mass of the ladders is smaller than in CaV_2O_5 and in fact almost the same as in NaV_2O_5.

6.2. B_{1g} modes

6.2.1. NaV_2O_5

The B_{1g} phonon modes of NaV_2O_5 are presented in Figure 6.3 and Table 6.4, respectively. Regarding the results of Ref. [90], in spite of their interpretation in terms of the space group $P2_1mn$, a unique relation between experiment and

Theory	Experiment							
	Ref. [90]	Ref. [7]	Ref. [91]	Ref. [37]	Ref. [36]	Ref. [19]	Ref. [16]	Ref. [92]
661	678	685	684	683	683	685	692	674
283	289	292	297	294	295	293	292	288
167	172	173	175	175	174	174	173	170

ω	Eigenvector			Assignment	
	$V1_y$	$O2_y$	$O3_y$	Ref. [37]	This work
661	0.13	-0.48	-0.00	V-O2 stretching	V-O2 stretching
283	-0.34	-0.10	0.35	O-V-O bending	O3-V-O2 bending
167	0.34	0.09	0.35	chain rotation	antiparallel leg-shift

Table 6.4.: Upper table: Calculated eigenfrequencies (cm^{-1}) of the B_{1g} phonon modes of NaV_2O_5 compared to experimental results from literature. Lower table: Theoretical eigenvector components and assignment of the phonon modes compared to the assignment of Ref. [37]. Details are explained in the text.

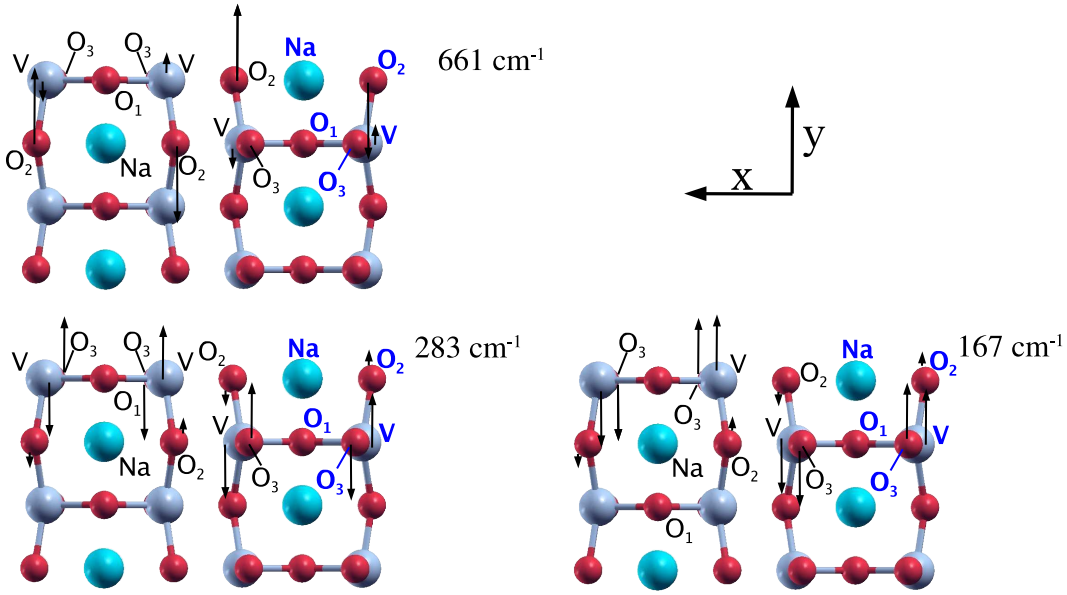

Figure 6.3.: B_{1g} eigenmodes of NaV_2O_5. The arrows show the direction and magnitude of the atomic displacements for each eigenmode.

theory is possible due to the polarization of the incoming and outgoing light in the Raman experiment. Moreover, three eigenmodes were found, which is compatible with the space group *Pmmn*. Thus, the B_1 modes of Ref. [90] ((*ab*) geometry) directly correspond to the B_{1g} modes. Ref. [7] (column three) does not specify any space group and reports a fourth mode at 262 cm^{-1} in (*ab*) geometry . But from the Raman spectra in Fig. 1 of this reference it can be seen, that the peak at

262 cm^{-1} has only very small intensity compared to the other three peaks. Hence it can be attributed either to noise or to an admixture of a B_{3g} mode found at the same frequency (see section 6.4.1 and, e.g., Ref. [37]). Therefore this mode is not included in Tab. 6.4.

The theoretical frequencies of all three B_{1g} modes are in very good agreement with experiment with differences smaller than 3.5%. The highest-frequency mode represents a stretching of V against the in-leg oxygen O2 in ladder direction, where the two legs of one ladder oscillate antisymmetrically while the apex oxygen O3 is not involved at all. This agrees with the assignment in Ref. [37]. In contrast to this mode, in the 283 cm^{-1} vibration a large O3 contribution is found. In detail, the apex oxygen O3 moves in y direction, out of phase with respect to the in-leg atoms V and O2, resulting in an O3–V–O2 bending. This is consistent with the description as V–O–V bending in Ref. [37]. The third B_{1g} mode with 167 cm^{-1}, finally, represents an antiparallel shift of the two legs of each ladder, together with a shearing of the apex O3, which oscillates more strongly in y direction than V and O2. This is in contrast to the assignment of Ref. [37], which interpret this mode as a chain rotation.

6.2.2. CaV_2O_5

Table 6.5 shows the theoretically obtained B_{1g} eigenmodes of CaV_2O_5 together with a comparison to experimental frequencies from literature. In Ref. [93], the spectra with HV polarization where identified as B_{1g} ones. But as already discussed in the context of the A_g modes, a direct assignment of the spectra with crossed polarization to B_{1g}, B_{2g}, or B_{3g}, respectively, is not possible. In fact, these spectra represent a mixture of all B_{ng} modes together with a participation of the A_g phonons. For this reason, columns two *and* three show frequencies from Ref. [93], where the former constitutes the original assignment, while frequencies in the latter column (marked with *) originate from a interpretation of the same data in view of the theoretically obtained phonon modes and Raman spectra. Again making use of theoretical results as a point of reference, column four (marked with **) shows a selection of the unpolarized results from Ref. [94]. Column five (marked by **) presents the B_{1g} frequencies of Ref. [39] as chosen in this work, where the assignment of the unpolarized Raman spectra of CaV_2O_5 was only done by comparison with the polarized NaV_2O_5 results. In contrast, column six again presents an assignment motivated by the theoretical results for phonon modes and Raman spectra.

The highest B_{1g} frequency with 593 cm^{-1} agrees reasonably with the experimental result (636–638 cm^{-1}), where the deviation is about 7%. As in NaV_2O_5, it represents a V–O2 stretching with hardly any participation of the apex oxygen O3. Nevertheless the frequency is about 6% smaller, which is due to the greater ionic charge of V in NaV_2O_5 compared to CaV_2O_5. As it is also the case for the V–O3 A_g stretching mode, a difference of 5% can be estimated from a simple

Theory	Experiment				
	Ref. [93]	Ref. [93] *	Ref. [94]**	Ref. [39]	Ref. [39]*
593	638	638	636	636	636
253	292	–	–	292	–
136	212	137	–	182	138.6

ω	Eigenvector			Assignment	
	$V1_y$	$O2_y$	$O3_y$	Ref. [39]	This work
593	-0.17	0.47	0.01	V-O2 stretching	V-O2 stretching
253	-0.28	-0.11	0.40	O-V-O bending	O3-V-O2 bending
136	0.38	0.14	0.30	chain rotation	antiparallel leg-shift

Table 6.5.: Upper table: Calculated eigenfrequencies (cm^{-1}) of the B_{1g} phonon modes of CaV_2O_5 compared to experimental results from literature. Lower table: Theoretical eigenvector components and assignment of the phonon modes compared to the assignment of Ref. [39]. Details are explained in the text.

Coulomb picture, which is in very good agreement with experiment.

Also the assignment of the 253 cm^{-1} mode corresponds to its NaV_2O_5 counterpart: It represents a O3–V–O2 bending. Compared to the NaV_2O_5 mode located at 283 cm^{-1}, the eigenvector component of V is slightly smaller in CaV_2O_5, while the apex oxygen O3 oscillates more strongly. The frequency shift of the CaV_2O_5 mode with respect to NaV_2O_5 is, again, due to the different ionic charge of V. Even though Refs. [39] and [93] identify the 292 cm^{-1} mode as a B_{1g} one, theoretical Raman spectra show that this peak must refer to a B_{2g} mode with a theoretical frequency of 259 cm^{-1}, because its intensity is more than one order of magnitude higher than that of the B_{1g} mode. Also for the 136 cm^{-1} mode the experimental situation appears to be confusing. Ref. [93] reports a B_{1g} frequency at 212 cm^{-1}, in contrast to 182 cm^{-1} found in Ref. [39]. Considering the theoretically obtained B_{1g} mode and analyzing the B_{ng} Raman spectra presented in Sect. 9.2, the 212 cm^{-1} and the 182 cm^{-1} modes should be assigned B_{2g} and B_{3g} symmetry, respectively. In turn, the B_{1g} mode lowest in frequency is found at 138 cm^{-1} in the Raman spectra of Refs. [39] and [93]. More precisely, theory predicts peaks in both, the B_{1g} and in the B_{2g} Raman spectra, at almost the same frequency, i.e. at 136 and 135 cm^{-1}, respectively, which moreover have virtually the same peak height. This implies that the experimental peak most probably originates from the superposition of a B_{1g} and a B_{2g} peak. Returning to the discussion of B_{1g} phonon frequencies, this means that the agreement between theory and experiment is excellent with less than 1% difference. Just as in NaV_2O_5, the 136 cm^{-1} mode of CaV_2O_5 corresponds to an anti-parallel shift of the two legs of one ladder combined with a shearing of the apex O3 with respect to the V–O2 leg. Compared with NaV_2O_5, the shearing is less pronounced in CaV_2O_5, i.e. the

amplitude of the O3 displacement and those of the V and O2 oscillations are more balanced.

6.3. B_{2g} modes

6.3.1. NaV_2O_5

Theory	Experiment									
	Ref. [90]	[90]*	[37]	[37]*	[36]	[36]*	[19]	[19]*	[92]	[92]*
979	970	949	954	954	951	951	954	954	954	954
683	531	693	550	683	–	–	550	690	677	677
472	–	470	–	–	550	477	–	474	–	–
360	308	398	–	–	429	392	–	393	–	–
286	224	257	–	260	392	254	–	254	–	256
206	190	224	226	226	225	225	226	226	226	226
157	176	190	192	192	186	186	192	192	190	190
141	89	146	149	149	141	141	149	149	144	144

ω	Eigenvector								Assignment	
	V_x	V_z	Na_x	$O1_x$	$O2_x$	$O2_z$	$O3_x$	$O3_z$	Refs. [37]	This work
979	0.04	-0.24	-0.01	-0.01	-0.01	-0.00	-0.04	0.41	V-O3 stretch.	V-O3 stretch.
683	0.12	0.04	0.02	-0.65	0.14	0.02	0.01	0.01	V-O1 stretch.	V-O1 stretch.
472	0.01	0.03	0.01	-0.17	-0.47	0.11	-0.02	0.00	V-O2 stretch.	O2-V-O1 bend.
360	0.26	-0.17	0.04	0.10	0.05	0.16	-0.22	-0.14	O-V-O bend.	O2-V-O3 bend.
286	-0.20	-0.16	-0.04	-0.05	0.05	0.33	0.26	-0.04	O-V-O bend.	O2-V-O3 bend.
206	0.25	-0.13	-0.19	0.05	-0.06	-0.15	0.34	-0.07	O-V-O bend.	Na-ladder shear
157	-0.04	-0.17	0.60	-0.04	-0.04	-0.14	0.07	-0.11	chain rotation	Na ∥ a + chain rot.
141	-0.19	-0.27	-0.29	-0.16	-0.05	-0.18	-0.14	-0.17	Na ∥ a	chain rotation

Table 6.6.: Upper table: Calculated eigenfrequencies (cm^{-1}) of the B_{2g} phonon modes of NaV_2O_5 compared to experimental results from literature. Lower table: Theoretical eigenvector components and assignment of the phonon modes compared to the assignment of Ref. [37]. Details are explained in the text.

The B_{2g} phonon modes of NaV_2O_5 are shown in Figure 6.4 and Table 6.6, respectively. The assignment of B_{2g} phonons presented in literature is incomplete. Instead, one to three B_{2g} modes are missing in the different papers. Moreover, there are inconsistencies when comparing the references to each other. Taking into account the theoretically obtained B_{2g} eigenvectors and frequencies together with the computed Raman spectra, a new interpretation of the experimentally measured spectra in xz polarization is possible. For this reason, in Table 6.6 together with the results from Refs. [90, 37, 36, 19] a second column with the re-interpreted spectra marked with * is presented.

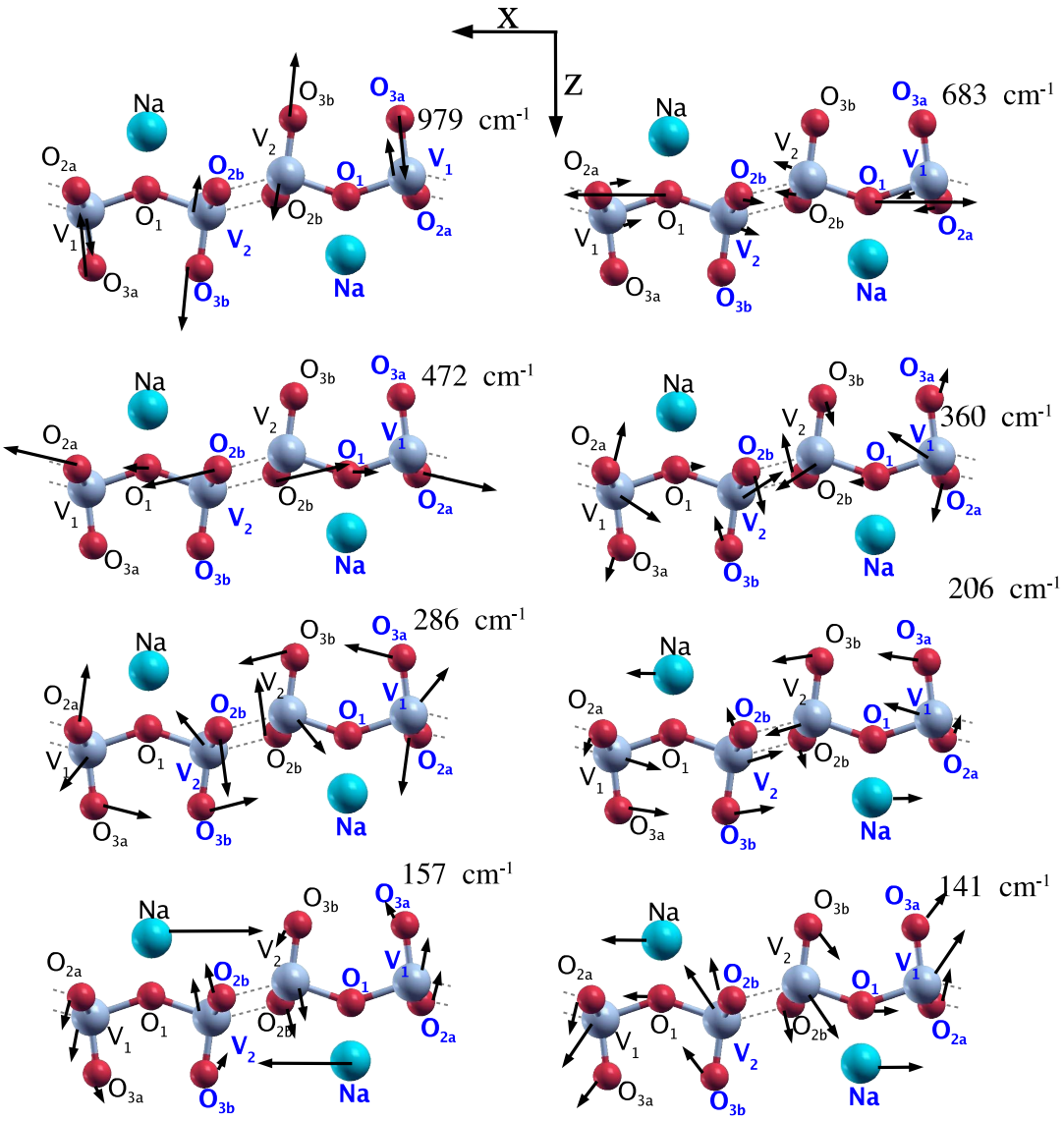

Figure 6.4.: B_{2g} eigenmodes of NaV_2O_5. The arrows show the direction and magnitude of the atomic displacements for each eigenmode.

For the highest-frequency mode the experimental situation is rather clear. Except for Ref. [90], where a frequency of 970 cm^{-1} is presented, all references report a peak at about 950 cm^{-1}. Analyzing the peak at 970 cm^{-1} in Ref. [90], it turns out that its position coincides with the position of an A_g peak, strongly indicating that it does not belong to a phonon mode with B_{2g} symmetry, as already discussed by Ref. [37]. For this reason the experimental frequency can be assumed to be at 950 cm^{-1}, which is not as close to the theoretical frequency of 979 cm^{-1} as 970 cm^{-1}, but still in very good agreement. Also the displacement pattern is unambiguous: As described in Ref. [37], the calculated eigenvectors

clearly exhibit a V–O3 stretching.

In contrast, the assignment of the B_{2g} mode next lower in frequency is quite controversial. Ref. [90] presents a B_{2g} mode at 530 cm^{-1}, which—as already discussed in Ref. [37]—appears to come from the A_g mode found at the same frequency, while Refs. [37, 36, 19] report a B_{2g} mode at 550 cm^{-1}. In Ref. [92], however, this B_{2g} mode is found at 681 cm^{-1}, which is in perfect agreement with the theoretical frequency of 683 cm^{-1}. Moreover, the experimental feature around 550 cm^{-1} is very asymmetric and smeared out, while there is a sharp peak at 683 cm^{-1} present in the xz polarized Raman spectra of Refs. [92] and [37]. For all these reasons we propose that the B_{2g} mode second-highest in frequency is located at about 685 cm^{-1}, while the feature at 550 cm^{-1} is likely to involve higher-order terms or other mechanisms not directly related to the discussed eigenmodes. In spite of the different frequency given in Ref. [37], its mode assignment agrees with the theoretical eigenvector identifying the phonon mode as a V–O1 stretching.

Both, theoretical Raman spectra and experiments, agree in the point that the O2–V–O1 bending mode at 472 cm^{-1} has rather low intensity. This may be the reason why in Refs. [90] and [36] no corresponding entry is found in the tables of B_{2g} phonons, although —in excellent agreement with theory—peaks at 470 cm^{-1} and 477 cm^{-1}, respectively, can be distinguished in the corresponding spectra. In the B_{2g} spectra of Refs. [37, 95, 92], on the other hand, such a peak can hardly be identified. Regarding the atomic movements related to this eigenmode, the V–O2 stretching reported in Ref. [37] is verified by theory, with an additional participation of the in-leg oxygen O1, oscillating in c direction (Fig. 6.4).

The range between 390 cm^{-1} and 450 cm^{-1} again appears to be controversial in literature. In the spectra of Refs. [37, 19, 92] only a very broad feature, but no peaks can be distinguished between 330 cm^{-1} and 550 cm^{-1}. Consequently no B_{2g} modes are reported for this region. Nevertheless, a calculation within a valence shell model presented in Ref. [37] gives a mode of 382 cm^{-1}. Ref. [90] assigns a peak at 308 cm^{-1} B_{2g} symmetry, but—as already argued in Ref. [37]—it most probably stems from an A_g mode found at the same energy. On the other hand, the spectra of Ref. [90] with xz polarization show a clear peak at 398 cm^{-1}, which is well compatible with the theoretically obtained frequency of 360 cm^{-1}. This also agrees with Ref. [36], which reports a B_{2g} mode at 392 cm^{-1}, while the 429 cm^{-1} mode presented in the same reference can most probably be related to the A_g mode at 420 cm^{-1}. In agreement with the characterization given in Ref. [37] we find that the 360 cm^{-1} mode represents an O–V–O bending. A more detailed analysis of the eigenvector allows a improved description of the participating oxygen atoms, showing that mostly the in-leg oxygen O2 and the apex oxygen O3 contribute to this bending mode, while the displacement of the in-rung oxygen O1 is comparably small.

Theory also allows a more detailed analysis of the 286 cm^{-1} mode, again described as O–V–O bending in Ref. [37]. Also this mode can be identified as O2–V–O3 bending, but in comparison to the previously described mode the O3

atom oscillates more strongly and with a larger x component, i.e. parallel to the ladder plane. Moreover, the V oscillation changes its direction: While in the 360 cm^{-1} mode the V atoms move towards the O2 of the neighboring ladder, in the 286 cm^{-1} mode they oscillate perpendicular to this direction. The experimental situation is comparable to the one for the O1–V–O2 bending mode. The spectra presented in Refs. [90, 37, 19, 92] show a weak peak located between 255 and 260 cm^{-1}, but apparently this peak was not pronounced enough to be included in the respective tables. Here, again, the theoretical eigenfrequency together with the calculated Raman spectra, which confirm the low intensity of the corresponding peak, allow a re-interpretation of the experimental curves identifying the above mentioned weak features as originating from a B_{2g} phonon mode.

The situation is clearer for the 206 cm^{-1} mode. All five references [90, 37, 36, 19, 92] report a B_{2g} mode at about 225 cm^{-1}, which is in acceptable agreement with theory. On the other hand, the assignment of Ref. [37], describing this mode as O–V–O bending, is not verified by our calculations. Instead we find a movement of all atoms in x direction, where Na oscillates out of phase compared to the other atoms belonging to the same ladder. These displacements correspond to a shear of Na with respect to the V–O ladders. Also for the B_{2g} mode next lower in frequency the experimental situation is quite clear. In all experiments (Refs. [90, 37, 36, 19, 92]) a peak at about 190 cm^{-1} can be found in the xz polarized spectra, which is also interpreted as B_{2g} mode in the last three references. Ref. [90] assigns a peak in the xz polarized spectra at 175 cm^{-1} B_{2g} symmetry, even though there is a stronger peak 15 cm^{-1} above. In fact, already in Ref. [37] this 175 cm^{-1} peak is interpreted as A_g feature. Also in view of the other references, the 190 cm^{-1} peak is probable to be the one stemming from a B_{2g} phonon mode. Comparing the experimental frequency with the theoretical result (157 cm^{-1}), a difference of 16% is found. The calculated eigenvector somewhat differs from the mode-assignment in Ref. [37]: While we find a weakly pronounced chain rotation as it is also described in this references, the most striking feature of the 157 cm^{-1} mode is an oscillation of Na in x direction.

In contrast to the assignment of Ref. [37], the 141 cm^{-1} mode turns out to represent the chain rotation, i.e. the experimental assignment for the two modes lowest in frequency appears to be swapped. For the lowest-frequency mode experimental and calculated frequency excellently agree. The theoretical frequency lies at 141 cm^{-1}, and experiments report this mode to be located between 141 and 149 cm^{-1}. The only exception is found in Ref. [90] with the lowest B_{2g} mode at 89 cm^{-1}. But—as Ref. [37] also stated for this mode—the related peak is very likely to derive from the A_g mode at the same frequency, while the same spectra show a peak at 146 cm^{-1} as well, which perfectly agrees with the theoretical and other experimental results. Therefore we conclude that the latter peak is the one originating from a phonon with B_{2g} symmetry.

6.3.2. CaV_2O_5

Theory	Experiment			
	Ref. [93]	Ref. [94]	Ref. [39]	Ref. [39]*
842	867	–	–	–
652	–	–	–	
499	–	–	–	–
342	310	310	334	311
259	–	–	311	–
219	212	211	213	213
190	182	–	–	182
135	137	–	–	138.6

ω	Eigenvector								Assignment	
	V_x	V_z	Ca_x	$O1_x$	$O2_x$	$O2_z$	$O3_x$	$O3_z$	Ref. [39]	This work
842	0.04	-0.25	-0.02	0.03	-0.03	-0.01	-0.05	0.43	V-O3 stretch.	V-O3 stretch.
652	-0.21	-0.02	-0.01	0.62	-0.07	-0.07	-0.02	-0.04	V-O1 stretch.	V-O1 stretch.
499	-0.01	0.03	0.02	-0.04	-0.48	0.12	-0.01	-0.02	V-O2 stretch.	O2-V-O1 bend.
342	-0.33	0.18	-0.04	-0.12	-0.03	-0.21	0.18	0.15	O-V-O bend.	O2-V-O3 bend.
259	-0.19	-0.23	-0.05	-0.03	0.06	0.29	0.25	-0.07	O-V-O bend.	O2-V-O3 bend.
219	0.28	-0.02	-0.14	0.07	-0.07	-0.16	0.36	-0.02	O-V-O bend.	Ca-ladder shear
190	-0.04	-0.28	0.39	-0.06	-0.06	-0.26	0.05	-0.15	chain rotation	Ca ∥ a + chain rot.
135	-0.10	-0.24	-0.38	-0.09	-0.05	-0.20	-0.18	-0.17	Ca ∥ a	chain rotation

Table 6.7.: Upper table: Calculated eigenfrequencies (cm^{-1}) of the B_{2g} phonon modes of CaV_2O_5 compared to experimental results from literature. Lower table: Theoretical eigenvector components and assignment of the phonon modes compared to the assignment of Ref. [39]. Details are explained in the text.

The eigenfrequencies and eigenvectors of the B_{2g} phonon modes of CaV_2O_5 are presented in Table 6.7. On the experimental side, the number of reported B_{2g} modes is rather sparse. In the polarized measurements on a polycrystalline sample reported in Ref. [93], where B_{2g} phonon peaks are mostly found in HV polarization, four peaks be related to B_{2g} modes. Among these four modes, only for one mode the measured frequency at 212 cm^{-1} was explicitly given in the reference, while we determined the other three modes at 182 cm^{-1}, 310 cm^{-1}, and 867 $cm^{-1}$by assigning additional peaks appearing in the presented cross-polarized spectra. In Refs. [94], where the peaks are not assigned a certain symmetry, we identify three frequencies of the unpolarized spectra as B_{2g} peaks. For Ref. [39] finally, where the unpolarized spectra were assigned by comparison to the NaV_2O_5 results, we present, in addition, in column five (marked with *) the interpretation of this spectra in the light of theoretically obtained eigenfrequencies and Raman spectra.

Like its NaV_2O_5 counterpart, the highest frequency B_{2g} mode of CaV_2O_5 represents an unambiguous V–O3 stretching. The eigenvectors of the CaV_2O_5 and the NaV_2O_5 mode are virtually identical, with the main contributions coming from oscillations of V and the apex oxygen O3 along the V–O3 bond. On the experimental side little information about this B_{2g} mode can be found. Only in Ref. [93], in good agreement with theory a feature at 867 cm^{-1} can be distinguished, which however is very weak and not explicitly labeled in the reference. The lower frequency in CaV_2O_5 compared NaV_2O_5, as it is the case for the A_g V–O3 stretching mode, is due to the smaller positive charge carried by the V ion in the former compared to the latter.

For the B_{2g} mode at 652 cm^{-1} no experimental result is found at all. Similar to the situation in NaV_2O_5, this mode represents a V–O1 stretching, with the most characteristic feature being an oscillation of the in-rung O1 in x direction. The main differences to NaV_2O_5 consist in a larger V_x component and a change in the O2 movement, which has a considerable z component in CaV_2O_5. As for the V–O3 stretching, also for this mode the frequency is lower compared to the analogous NaV_2O_5 vibration, which can be explained again by the differently charged V ion and by the fact that V, which has a much larger mass than oxygen, contributes considerably more to the eigenvector.

The B_{2g} vibration next lower in energy represents an O2–V–O1 bending mode at 499 cm^{-1}, where the $O2_x$ component is clearly dominating the eigenvector. Here the theoretical eigenvectors allow to render more precisely the assignment given in Ref. [39], where this mode is identified as V–O2 stretching. Altogether, the eigenvector again hardly differs from the respective NaV_2O_5 counterpart. Experimentally, there are no results available for this phonon mode. This implies that its Raman intensity is quite small, which is also verified by the theoretical Raman spectra. In terms of eigenfrequencies, the CaV_2O_5 mode is located lower than the NaV_2O_5 mode, which can be related to the fact that both the distances to the next V atom along the leg and the next V atom on the neighboring ladder are smaller in CaV_2O_5.

In contrast to this mode, for the O2–V–O3 bending an experimental frequency can be found in all three references. Assuming that the 334 cm^{-1} mode—appearing in the tables of A_g as well as B_{2g} modes in Ref. [39]—is in fact an A_g feature, all three references ([93, 94, 39]) concordantly report a frequency of about 310 cm^{-1}, which is about 10% lower than the theoretical result of 342 cm^{-1}. Comparing the displacement pattern to that of the NaV_2O_5 O2–V–O3 bending mode, the V components of the eigenvector are considerably larger and more parallel to the ladder plane, while O2 has a slightly larger z component. The eigenfrequency is distinctly lower in CaV_2O_5 than in NaV_2O_5, which another time can be ascribed to the smaller charge of the V ion in CaV_2O_5, on the one hand, and on the other hand to the fact that the heavy V has a larger contribution to the eigenmode.

For the 259 cm^{-1} mode, no corresponding experimental feature can be found

in Refs. [39, 93, 94]. The reason for this are most probably the dominant peaks of the A_g modes at 280 cm^{-1} and 238 cm^{-1}, respectively, which are likely to cover the scattering intensity from the B_{2g} mode, as can be seen from the theoretical Raman spectra in Sect. 9.2. Also this mode can be described as a O2–V–O3 bending, where however the V atoms oscillate less and the O2 and O3 atoms more intensively than in the 340 cm^{-1} mode. The eigenvector of this CaV_2O_5 mode is quite similar to that of the NaV_2O_5 286 cm^{-1} vibration, with slightly altered V components and a moderately enhanced $O2_z$ displacement. Again we assume that the lower frequency in the CaV_2O_5 mode is due to the smaller Coulomb force in this system.

The B_{2g} mode next lower in energy is well documented experimentally. All three references report phonon mode at about 212 cm^{-1}, which excellently agrees with the theoretical result of 219 cm^{-1}. However, we find a somewhat different movement of the atoms compared to the assignment of Ref. [39], where this mode is presented as O–V–O bending. The theoretical eigenvector shows a considerable oscillation of Ca parallel to x, which is out of phase with respect to a corresponding movement of the ladder atoms O1, V, and O3 along the same direction, thus representing a kind of shear of the Ca plane with respect to the V–O ladders. The orientation of the ladders' movement in x direction is even more pronounced than in the analogous NaV_2O_5 mode. On the other hand, also the in-leg oxygens O2 are considerably involved in this B_{2g} mode oscillating perpendicular to the ladder plane. The frequency of the CaV_2O_5 and the NaV_2O_5 mode differ only little, indicating that competing effects widely compensate each other: On the one hand, the ionic charge of Ca^{2+} is larger compared to that of Na^+ and the V–O2 distances are shorter CaV_2O_5. On the other hand, Ca is heavier than Na and the V ions carry less charge in CaV_2O_5.

Both of the two B_{2g} modes lowest in frequency involve rotations of the ladder together with a movement of Ca in x direction. In the first mode, with a theoretical frequency of 190 cm^{-1}, Ca moves out-of-phase with respect to the x components of the ladder atoms V, O1, and O2. The Ca participation represents an additional feature with respect to the assignment in Ref. [39], where this mode is solely described as a chain rotation. In terms of frequency it can be related to an experimentally observed phonon mode found at 182 cm^{-1}, as it is reported in Ref. [93]. Also in the unpolarized spectra presented in Ref. [39] a peak at 182 cm^{-1} can be distinguished. While this peak—in analogy to the 172 cm^{-1} peak of the NaV_2O_5 B_{2g} mode—was interpreted as B_{1g} peak in the cited reference, theory implies that it is rather stemming from a B_{2g} phonon. Thus theory and experiment agree very well for this mode. Relating the discussed B_{2g} mode to the respective mode of NaV_2O_5, a smaller frequency is found in the former despite of the larger Coulomb attraction implied by the stronger ionicity of Ca^{2+} compared to Na^+. This can be explained by the much greater mass of Ca compared to Na together with a larger eigenvector component of the heavy V atom in CaV_2O_5.

The second chain-rotation mode in CaV_2O_5 is located at a theoretical frequency of 135 cm^{-1}. In contrast to the 190 cm^{-1} mode, in this mode the Ca atom moves in-phase with the V and O atoms of the ladder, hence making this mode even clearer a chain rotation than the previous one. Compared to the respective vibration in NaV_2O_5, the x component of the metal ion is considerably larger in CaV_2O_5. Taking into account that on the one hand the ratio of the Ca_x component to the Na_x component is 1.31, and on the other hand the ratio of the square root of masses $\sqrt{m_{Ca}/m_{Na}}$ equals 1.32, the effective displacements of the metal ion in the lowest-frequency B_{2g} mode precisely coincide. Looking at the V atoms, we find that their oscillation is smaller and more perpendicular to the ladder plane in CaV_2O_5 compared to NaV_2O_5. On the experimental side, the corresponding peak is most probably a feature found at about 138 cm^{-1} in both Refs. [39] and [93]. As already discussed in section 6.2.2, this feature is in fact likely to represent a superposition of both, a B_{1g} and a B_{2g} peak, at almost the same frequency and with almost the same intensity. Once more the agreement between theory and experiment is very good, with a difference of only 2%. Comparing the lowest-frequency B_{2g} mode of CaV_2O_5 with the corresponding mode of NaV_2O_5, the latter is again about 5% higher in frequency. At the first sight, this seems to be a contradiction, since the ionic charge is larger and consequently a larger Coulomb attraction must be present in CaV_2O_5. In turn, the reduced mass of the atoms contributing to the CaV_2O_5 oscillation is larger, which is due to the larger mass of Ca compared to Na together with a larger eigenvector component of the metal ion in CaV_2O_5, at the expense of the eigenvector components of the lighter oxygen atoms. The altered reduced mass explains the lower frequency in this compound.

6.4. B_{3g} modes

6.4.1. NaV_2O_5

Figure 6.5 and Table 6.8 show the B_{3g} modes of NaV_2O_5 as obtained from theory. Regarding the experimental results in Tab. 6.8, for each reference together with the originally reported eigenfrequencies a second column with a re-interpretation of the reported spectra in the light of the calculated eigenmodes and Raman spectra is added. For Ref. [90], where not the actual space group $Pmmn$, but the earlier proposed space group $P2_1mn$ was assumed, the values reported in Tab. 6.8 refer to the peaks measured in yz polarization and presented as phonon modes with A_2 symmetry.

Theory and the assignment in Ref. [37] accordingly identify the B_{3g} mode at 708 cm^{-1} as a V–O2 stretching mode, where the in-leg oxygen O2, however, is much more displaced than the V neighbor. Regarding the experimental frequency of this phonon mode, Ref. [90] reporting 970 cm^{-1} contravenes the results of

Theory	Experiment								
	Ref. [90]	Ref. [90]*	Ref. [37]	Ref. [37]*	Ref. [36]	Ref. [36]*	Ref. [19]	Ref. [92]	Ref. [92]*
708	970	685	684	684	683	683	684	681	681
384	685	365	366	366	418	366	368	362	362
262	365	260	260	260	366	257	261	260	260
188	260	165	–	173	257	169	–	–	170
136	89	135	–	140	169	137	–	–	137

ω	Eigenvector					Assignment	
	$V1_y$	Na_y	$O1_y$	$O2_y$	$O3_y$	Ref. [37]	This work
708	-0.14	-0.00	-0.04	0.48	0.00	V-O2 stretching	V-O2 stretching
384	-0.30	-0.03	0.48	-0.05	0.20	V-O1-V bending	O1-V-O3 bending
262	-0.28	0.05	-0.32	-0.11	0.33	O-V-O bending	rung *vs* O3 shear
188	0.30	-0.26	0.03	0.09	0.35	Na ∥ b	(ladder *vs* Na) ∥ b
136	-0.21	-0.55	-0.09	-0.07	-0.21	chain rotation	antiparallel ladder shift

Table 6.8.: Upper table: Calculated eigenfrequencies (cm^{-1}) of the B_{3g} phonon modes of NaV_2O_5 compared to experimental results from literature. Lower table: Theoretical eigenvector components and assignment of the phonon modes compared to the assignment of Ref. [37]. Details are explained in the text.

Refs. [37, 36, 19, 92], which clearly indicate that this mode is located at about 685 cm^{-1}. As already discussed in Ref. [37] and Sect. 6.3.1, the peak at 970 cm^{-1} found in the yz polarized spectra of Ref. [90] is in fact likely to stem from an A_g mode at the same frequency. Instead we propose that in Ref. [90] the next lower frequency at 685 cm^{-1} is the B_{3g} mode highest in energy, as it is displayed in the third column. This frequency is in good agreement with theory.

Also for the B_{3g} mode next lower in energy the situation in literature is not completely univocal. Ref. [36], in addition to a lower frequency of 366 cm^{-1}, also presents a B_{3g} mode at 418 cm^{-1}, which, however, is neither verified by the other experiments nor by theory. Instead, Refs. [37, 19, 92] for the B_{3g} mode second highest in frequency report a value of 362–368 cm^{-1}, which is close to the theoretical eigenfrequency of 384 cm^{-1}. Moreover, the frequency of 418 cm^{-1} coincides with the location of a A_g peak, such that it is quite likely not to belong to the B_{3g} modes. Therefore in our assignment of the spectra of Ref. [36] in column seven this frequency was substituted by the lower one at 366 cm^{-1}. Concerning the mode assignment, the theoretically calculated eigenvector suggests some alteration with respect to the results presented in Ref. [37]. In this reference, the mode at 365 cm^{-1} is related to a V–O1–V bending, while we also find a considerable contribution of the apex oxygen O3 oscillating parallel to the in-rung oxygen, but out-of-phase with respect to the vanadium atom, which implies that this mode represents a O1–V–O3 bending.

For the B_{3g} eigenmode at 262 cm^{-1}, the peak assignment with respect to the

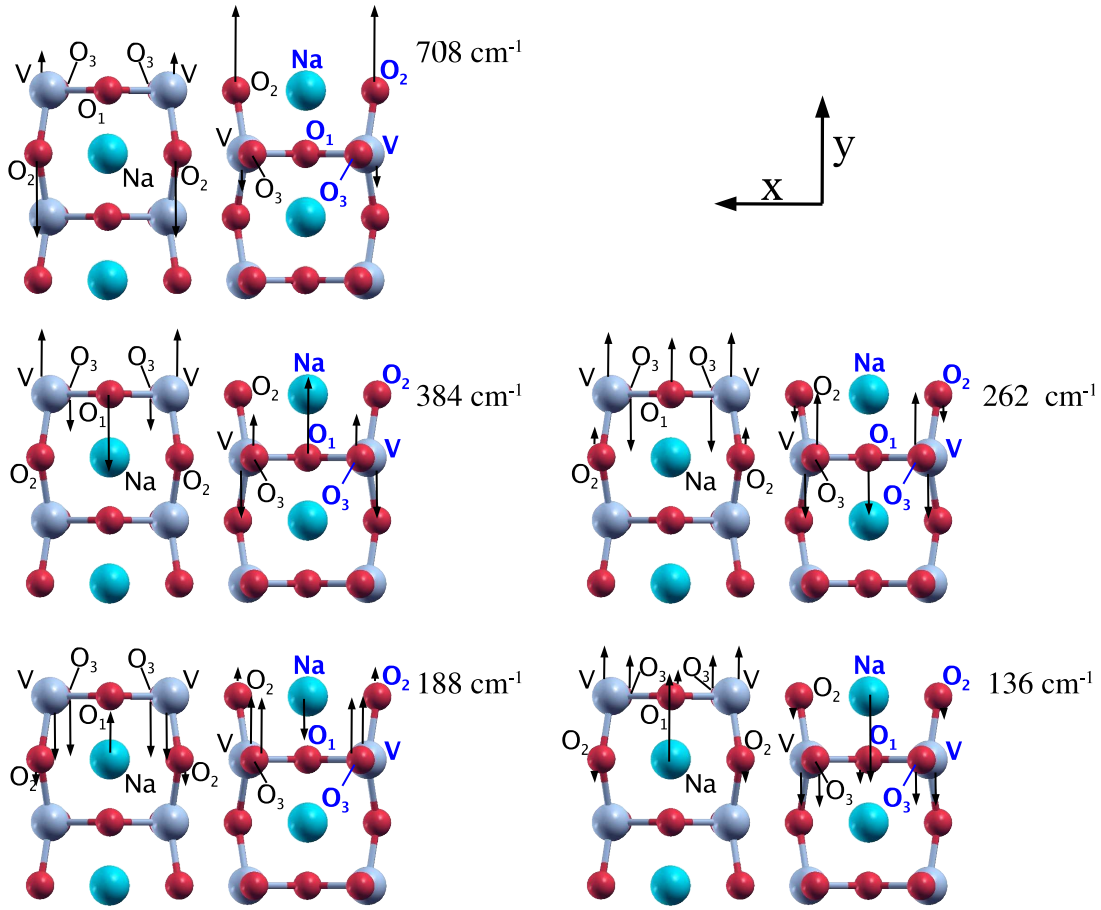

Figure 6.5.: B_{3g} eigenmodes of NaV_2O_5. The arrows show the direction and magnitude of the atomic displacements for each eigenmode.

experimental spectra is unambiguous. All Refs. ([90, 36, 37, 19, 92]) report a corresponding mode in the range between 257 and 261 cm^{-1}, i.e. within a few wave numbers from the theoretically obtained values. Regarding the mode assignment, the theoretically calculated eigenvector allows a more detailed specification. While Ref. [37] speaks about an O–V–O bending, we find that this mode involves an oscillation of the apex oxygen O3, which is antiparallel to the movement of the ladder-atoms V and O1 such that it can be described as a shear of the O3 atoms with respect to the rest of the ladder. Also the in-leg oxygen O2 makes some contribution to this mode, which is however much smaller than the before mentioned eigenvector components of V, O2 and O3.

For the two B_{3g} phonon modes lowest in energy the experimental situation appears to be more challenging. Refs. [37, 19, 92] do not explicitly report any frequency at all, while Refs. [90] and [36] find just one frequency located at 89 cm^{-1} and 169 cm^{-1}, respectively. The theoretical B_{3g} spectrum presented in

Sect. 9.1 sheds light on the situation: The intensity of the B_{3g} Raman spectra at 188 and 136 cm^{-1}, respectively, turns out to be very small, thus making it difficult to identify the related peaks. Nevertheless, making use of the theoretical results in terms of peak heights and eigenfrequencies, a new interpretation of the experimental spectra presented in literature is possible. In fact, in three of the references (Refs. [90, 37, 92]) additional B_{3g} peaks at about 170 cm^{-1} can be distinguished confirming the 169 cm^{-1} mode reported in Ref. [36], and in all four references [90, 36, 37, 92] a peak at 135–140 cm^{-1} can be found, which is in perfect agreement with the calculated eigenfrequency of 136 cm^{-1}.

6.4.2. CaV_2O_5

Theory	Experiment			
	Ref. [93]*	Ref. [94]*	Ref. [39]	Ref. [39]*
605	–	–	636	–
392	369	–	366	366
254	292	293	280	292
195	–	–	-	-
113	–	–	-	-

ω	Eigenvector					Assignment	
	$V1_y$	Ca_y	$O1_y$	$O2_y$	$O3_y$	Ref. [39]	This work
605	-0.18	-0.00	-0.01	0.46	0.02	V-O2 stretching	V-O2 stretching
392	-0.16	-0.11	0.59	-0.06	0.19	V-O1-V bending	O1-V-O3 bending
254	-0.27	0.06	-0.20	-0.12	0.38	O-V-O bending	rung *vs* O3 shear
195	0.24	-0.51	-0.10	0.08	0.22	Ca ∥ b	(ladder *vs* Ca) ∥ b
113	-0.34	-0.28	-0.07	-0.13	-0.27	chain rotation	antiparallel ladder shift

Table 6.9.: Upper table: Calculated eigenfrequencies (cm^{-1}) of the B_{3g} phonon modes of CaV_2O_5 compared to experimental results from literature. Lower table: Theoretical eigenvector components and assignment of the phonon modes compared to the assignment of Ref. [39]. Details are explained in the text.

The calculated eigenvectors and eigenfrequencies of CaV_2O_5 with B_{3g} symmetry are shown in Table 6.9. In Refs. [93, 94] the unpolarized spectra are presented without a symmetry assignment such that the peak positions reported in the respective columns (marked by *) are chosen due to the theoretical eigenmodes and Raman spectra. Also for the results of Ref. [39], where a symmetry assignment of the unpolarized Raman spectra was done by comparing the peak positions with those of the polarized spectra for NaV_2O_5, an additional column with a re-interpretation of the spectra in the light of theory is presented (also marked with *). In general the experimental information about the B_{3g} phonons is quite limited. Among the five B_{3g} modes existing in CaV_2O_5, only between one and

three modes are detected, where in the latter case one of the three modes is not verified by theory. Ref. [39] makes use of the assignment originally done for NaV_2O_5 also for CaV_2O_5 by relating the peaks interpreted as B_{3g} modes to the NaV_2O_5 B_{3g} mode closest in frequency. Therefore, the characterizations of these modes do not have to apply to CaV_2O_5.

The B_{3g} mode with a frequency of 605 cm^{-1} represents a clear V–O2 stretching, where the in-leg oxygens O2 oscillate very strongly towards the neighboring V atoms of the same leg, which in turn move out-of-phase with the O2 atoms, but with considerably smaller amplitude. All other atoms do virtually not participate in this eigenmode. Thus the eigenvector of this mode is very similar to the one of the corresponding NaV_2O_5 mode and to the assignment given in Ref. [39]. On the experimental side, only Ref. [39] presents a result, i.e. a B_{3g} frequency of 636 cm^{-1}. But since, on the one hand, this peak was also included in the list of B_{1g} modes of this reference, and on the other hand the theoretical Raman spectra (Sect. 9.2) indicate that the B_{1g} peak with 593 cm^{-1} has an intensity one order of magnitude greater than the B_{3g} mode, we assume that the 636 cm^{-1} peak stems from a B_{1g} vibration. Compared to the frequency of the related NaV_2O_5 mode situated at about 700 cm^{-1}, the energy of the CaV_2O_5 mode is much lower. In this context, an analogous argumentation as for the V–O2 mode with B_{1g} symmetry applies, i.e. the lower frequency can be ascribed to the smaller charge of the V ion in CaV_2O_5 compared to NaV_2O_5.

For the B_{3g} mode with a frequency of 392 cm^{-1}, the experimental situation is comparably clear. Refs. [39] and [93] both show a peak at around 367 cm^{-1}, which is about 6% lower than the theoretical result. The main characteristics of this phonon mode comprise oscillations of the in-rung oxygen O1 and the apex oxygen O3, which together move antiparallel with respect to the V atoms. The $O1_y$ component, however, is strongly dominating with respect to the V_y and the $O3_y$ displacements. Thus the theoretical findings mostly verify the assignment given in Ref. [39], extending it by the contribution of the apex oxygen atoms. Compared to the NaV_2O_5 B_{3g} mode at 384 cm^{-1}, the V atoms participate considerably less in the CaV_2O_5 eigenmode, while the O1 component is even larger. The lowered frequency of the CaV_2O_5 mode with respect to its NaV_2O_5 counterpart can be related to the fact, that in the CaV_2O_5 mode the contribution of the light O atoms is considerably greater than in the NaV_2O_5 case.

Also for the B_{3g} mode at 254 cm^{-1} experimental counterparts can be found. In detail, the spectra of all references ([39, 93, 94]) contain a peak at about 292 cm^{-1}. As already discussed in the context of the A_g phonons (Section 6.1.2), we suppose that the 292 cm^{-1} peak of the unpolarized spectra in Ref. [39] is the one with B_{3g} symmetry. The reason for our assignment are the theoretical Raman spectra as presented in Sect. 9.2, which show that the intensity of the B_{3g} peak at 254 cm^{-1} is about 15 times higher than the one of a B_{1g} mode at 253 cm^{-1} and about seven times higher then the one of B_{2g} peak at 259 cm^{-1}. In contrast, the theoretical A_g peak at 265 cm^{-1} is again much higher than the

B_{3g} peak with 254 cm^{-1}. For this reason we identify in the spectra of Ref. [39] the peak at 280 cm^{-1} as A_g mode, even though it is originally assigned B_{3g} symmetry. The eigenvector of the 254 cm^{-1} vibration shows an oscillation of the apex oxygen O3 which is out-of-phase with respect to the V and O3 atoms of the ladder, while the O2 component is rather small. Thus it can be characterized as a shear of the O3 atom vs. the rung of the ladder. Thus, we provide a further specification compared to the assignment found in Ref. [39], which describes the B_{3g} mode third highest in energy as a O–V–O bending. Compared to the 262 cm^{-1} mode of NaV_2O_5, the CaV_2O_5 phonon has a smaller O1 component, which is compensated by a stronger movement of the apex oxygen O3. In terms of frequency, theory finds a slightly lower frequency in the CaV_2O_5 case, while the experimental frequency appears to be about 10% higher than in the Na compound.

The B_{3g} mode at 195 cm^{-1} lacks any experimental counterpart. This can be understood taking into account the theoretical Raman spectra, which show that the peak height for this mode is very small. As the NaV_2O_5 mode with 188 cm^{-1}, it represents an oscillation of the V and apex oxygen O3 antiparallel to the metal atom Ca (Na). However, a much larger eigenvector component of the metal ion is found, at the expense of a lowered V contribution. In addition, a considerable O1 contribution in-phase with the Ca motion is present. The frequency of the CaV_2O_5 mode appears to be slightly higher than the one for the corresponding NaV_2O_5 oscillation. This can be attributed to the smaller contribution of the heavy V atom in the CaV_2O_5 case.

For the B_{3g} mode lowest in frequency a theoretical result of 113 cm^{-1} is obtained. On the experimental side, no corresponding phonon mode can be found in literature, which can probably be ascribed to the fact that an A_g mode at a theoretical frequency of 106 cm^{-1} shrouds the much weaker B_{3g} peak. The 113 cm^{-1} mode represents an antiparallel shift of the two ladders of one unit cell in $+y$ and $-y$ direction, respectively. In comparison to the antiparallel ladder shift in NaV_2O_5, the V component is considerably larger in the CaV_2O_5 mode, while the Ca contribution is much smaller than the corresponding Na displacement. In turn, the in-leg oxygen O2 and the in-rung oxygen O3 show an increased component compared to NaV_2O_5. This implies that the ladder shift is more uniform in CaV_2O_5 than in NaV_2O_5, which is also one clue for the understanding of the 15% decrease in frequency compared to NaV_2O_5. A second reason is provided by the stronger participation of the heavy V atoms together with the larger mass of the metal atom in CaV_2O_5 (40 atomic mass units for Ca compared to a value of 23 for Na). These two effects lead, in contrast to the larger inter-ladder interaction as emerging from the enhanced tight binding parameter t_i (see Tabs. 10.1 and 10.4), to a considerably lower frequency of the antiparallel ladder shift in CaV_2O_5 compared to its counterpart in the sodium vanadate.

7. Infrared-active Phonon Modes

7.1. B_{1u} modes

7.1.1. NaV_2O_5

Theory	Experiment			
	Ref. [36]	Ref. [36]*	Ref. [37]	Ref. [38]
971	955	955	955	954
554	760	591	–	583
478	591	468	460	468
352	468	–	(368)	–
292	179	–	–	–
190	162	179	181	182
154	–	162	164	164

ω	Eigenvector								Assignment	
	V_x	V_z	Na_z	$O1_z$	$O2_x$	$O2_z$	$O3_x$	$O3_z$	Refs. [37]	This work
971	-0.05	0.25	-0.01	0.01	0.01	-0.01	0.06	-0.43	V-O3 stretch.	V-O3 stretch.
554	-0.35	-0.06	0.01	0.08	0.33	0.01	0.09	0.02	V-O2 stretch.	V-O2 stretch.
478	-0.05	-0.22	0.01	0.35	-0.18	0.31	-0.01	-0.12	V-O1-V bend.	O1-V-O2 bend.
352	0.03	0.10	-0.02	0.36	0.05	-0.32	-0.26	0.03	O-V-O bend.	O1-V-O2 b. + $O3_x$
292	0.28	-0.04	0.00	-0.01	0.33	0.18	-0.16	-0.07	O-V-O bend.	rung stretching
190	-0.20	-0.10	0.18	-0.19	-0.08	0.02	-0.39	-0.10	Na ∥ c	O1-V-O3 b.+ Na ∥ c
154	-0.12	0.11	-0.57	-0.07	-0.05	0.14	-0.20	0.05	Chain rotation	Na ∥ c

Table 7.1.: Upper table: Calculated eigenfrequencies (cm^{-1}) of the B_{1u} phonon modes of NaV_2O_5 compared to experimental results from literature. Lower table: Theoretical eigenvector components and assignment of the phonon modes compared to the assignment of Ref. [37]. Details are explained in the text.

The eigenfrequencies and eigenvectors of the B_{1u} modes of NaV_2O_5 are presented in Tab. 7.1 and Fig. 7.1, respectively. On the experimental side, only part of the seven B_{1u} modes resulting from theory are detected. In addition, the interpretation of the experimental peaks as presented in Ref. [36] is not fully consistent with the theoretical findings. For this reason, as in the previous sections, a second column with a re-interpretation of experimental spectra is presented (marked by *).

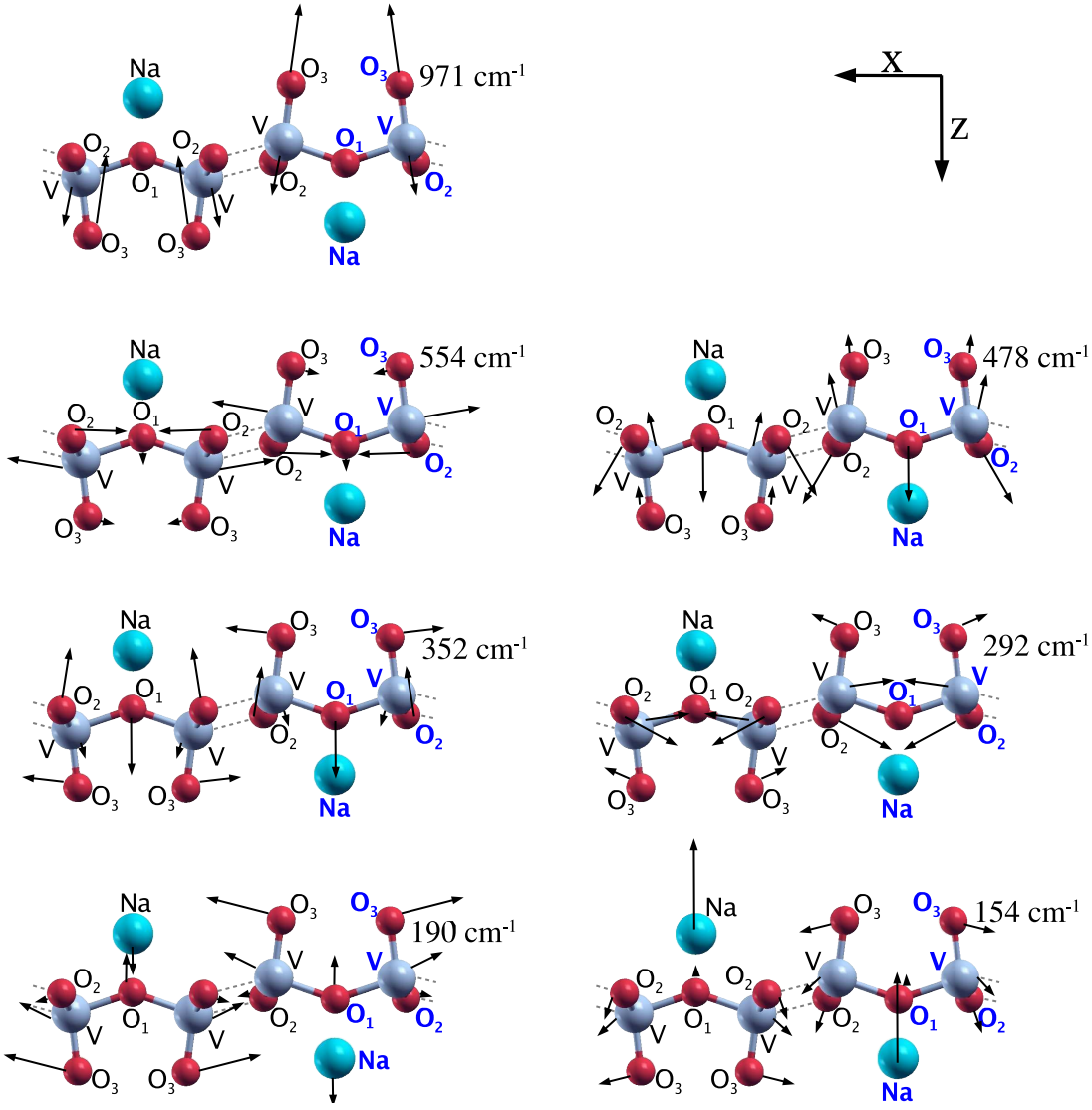

Figure 7.1.: B_{1u} eigenmodes of NaV_2O_5. The arrows show the direction and magnitude of the atomic displacements for each eigenmode.

Analogous to the A_g and B_{2g} modes highest in frequency, the eigenvector of the B_{1u} mode at 971 cm^{-1} represents a V–O3 stretching, which is also consistent with the assignment given in Ref. [37]. The theoretical frequency of 971 cm^{-1} is about 1.5% higher than its experimental counterpart of 955 cm^{-1}, reported in all three Refs. [36, 37, 38].

For the V–O2 stretching mode at 554 cm^{-1}, the experimental situation is not completely clear. While Ref. [37] does not present any measured frequency for this eigenmode, Refs. [36] and [38] give a frequency of 760 cm^{-1} and 583 cm^{-1}, respectively. Thus, the theoretical findings are in favor of the results of Ref. [38],

which are moreover supported from a calculated result included in Ref. [37], which reports an even lower frequency for this mode, i.e. 488 cm^{-1}. For this reason we believe that the weak 760 cm^{-1} feature in the spectra of Ref. [36] (polarization $\parallel$ c) does not originate from a B_{1u} mode.

The B_{1u} mode next lower in energy is located at a theoretical frequency of 478 cm^{-1}, which is in very good agreement with the experimental value of 460–468 cm^{-1}, with a deviation of 2–3% only. Regarding the assignment of this mode, the characterization as V–O1–V bending given in Ref. [37] is also verified by theory, where, however, also a rather large O2 component is found. Theory also allows the refinement of the mode assignment for the 352 cm^{-1} vibration. While Ref. [37] reports a O–V–O bending, the theoretical eigenvector reveals more details of this oscillation showing that it comprises both, an O1–V–O2 bending and an O3 movement in x direction. The frequency of this phonon mode as obtained by theory is 352 cm^{-1}. Experimentally, only Ref. [37] reports a corresponding frequency at 368 cm^{-1}, and even this peak is treated as not totally unambiguous, since it coincides with a B_{2u} peak at the same energy. Theory, however, indicates that this feature is really stemming from a phonon mode with B_{1u} symmetry.

An experimental result is completely missing for the B_{1u} mode with 292 cm^{-1}. Nevertheless, a calculated eigenfrequency for the eigenfrequency computed within a valence shell model together with a mode assignment is presented in Ref. [37]. In this context, a frequency of 277 cm^{-1} is presented, which is about 5% lower than our theoretical result. Regarding the mode assignment, our calculations again yield a more detailed determination. While Ref.[37] reports a O–V–O bending, our eigenvector exhibits an oscillation of the two legs of one ladder against each other, thus stretching the rungs. In addition, a small contribution of the apex oxygen is found.

For the B_{1u} mode at 190 cm^{-1}, the experimental counterpart is well documented. In all three references ([36, 37, 38]) a peak at around 180 cm^{-1} appearing in polarization $\vec{E} \parallel \vec{c}$ is reported, which is in good agreement with theory. On the other hand, the theoretical results suggest some modification with respect to the mode assignment given in Ref. [37]. While the cited reference describes this B_{1u} mode as oscillation of Na $\parallel$ c, we find that other contributions are more significant in this phonon mode. As the main characteristic, we identify a breathing-like oscillation of the two V–O3 pairs located at both ends of one rung, which move in x direction. In addition, a considerable z component of the in-rung oxygen O1 and the Na atom is found, where the latter, however, is not dominant.

In turn, theory implies that the B_{1u} mode lowest in frequency clearly involves a Na oscillation $\parallel$ c as its main feature. This is in contrast to the assignment given in Ref. [37], where the respective mode is described as chain rotation. In addition to the Na oscillation, we find a breathing-like motion of the V and O3

atoms similar to the one described above, but with smaller amplitude. The phase of the Na vibration with respect to the V–O3 breathing, however, is opposed to the one found in the 190 cm^{-1} mode. The theoretical frequency of 154 cm^{-1} is again in good correspondence with the experimental findings in literature, where frequencies of 162–164 cm^{-1} are reported.

7.1.2. CaV_2O_5

Theory	Experiment	
	Ref. [39]	Ref. [39]*
903	956	956
559	–	578
483	–	–
348	–	–
282	264	264
235	–	–
195	198	198

ω	Eigenvector								Assignment	
	V_x	V_z	Ca_z	$O1_z$	$O2_x$	$O2_z$	$O3_x$	$O3_z$	Refs. [39]	This work
903	-0.09	0.23	-0.01	0.03	0.05	-0.01	0.10	-0.42	V-O3 stretch.	V-O3 stretch.
559	-0.30	-0.02	0.02	-0.00	0.37	-0.10	0.05	0.11	V-O2 stretch.	V-O2 stretch.
483	-0.15	-0.25	0.00	0.39	-0.05	0.28	0.06	-0.07	V-O1-V bend.	O1-V-O2 bend.
348	0.11	0.11	-0.06	0.34	0.07	-0.25	-0.31	-0.00	O-V-O bend.	O1-V-O2 b. + $O3_x$
282	0.17	-0.08	0.04	-0.12	0.27	0.25	-0.24	-0.12	O-V-O bend.	rung stretching
235	-0.30	-0.05	0.13	-0.13	-0.19	-0.02	-0.32	-0.07	Ca ∥ c	O1-V-O3 b.+ Ca ∥ c
195	-0.14	0.14	-0.56	-0.06	-0.04	0.18	-0.11	0.09	Chain rotation	Ca ∥ c

Table 7.2.: Upper table: Calculated eigenfrequencies (cm^{-1}) of the B_{1u} phonon modes of CaV_2O_5 compared to experimental results from literature. Lower table: Theoretical eigenvector components and assignment of the phonon modes compared to the assignment of Ref. [37]. Details are explained in the text.

Table 7.2 presents the eigenvectors and eigenfrequencies of CaV_2O_5 with B_{1u} symmetry together experimental findings. In fact, to the best of our knowledge only one infrared reflectivity measurement for CaV_2O_5 is published in literature (Ref. [39]), which is presented in column two. Even though the measurements were performed with unpolarized light, the same reference also ascribes both, a symmetry and displacement pattern to its IR active modes, which is achieved by comparison with the results for NaV_2O_5. Since the theoretically calculated eigenmodes do not fully confirm the symmetry assignment of Ref. [39], in column three (marked with *) a re-interpretation of the experimental spectra in the light of the theoretical frequencies is presented.

The B_{1u} V–O3 stretching mode of CaV_2O_5 is found at a frequency of 903 cm^{-1}, which is about 5% lower than the experimental result of 954 cm^{-1}. The eigenvector is very similar to the one of the corresponding NaV_2O_5 mode, with slight variations in the V, the O2 and the O3 movements, which show an increased component in x direction. Also the experimental frequencies are virtually identical in both structures, which is quite surprising. In contrast, theoretical frequencies exhibit a shift of -7% going from NaV_2O_5 to CaV_2O_5. This finding is compatible with a lower V–O3 interaction in the latter, which is due to the decreased ionicity of the V ion. This behavior also reflected in the diminished energies of its V–O3 stretching modes with A_g and B_{3g} symmetry, respectively.

For the 559 cm^{-1} mode, no experimental counterpart is reported in literature. However, a peak located at 578 cm^{-1} is found in the unpolarized spectra of Ref. [39]. Even though this peak is originally interpreted as B_{2u} peak, the calculated eigenfrequencies indicate that it rather belongs to B_{1u} symmetry. In turn, we suggest that a peak found at 515 cm^{-1} (described as B_{3u} mode in the same reference) could originate from a phonon mode with B_{2u} symmetry. (This would imply that for the B_{3u} mode with a calculated frequency of 479 cm^{-1} no peak can be distinguished in the experimental spectra.) Compared to NaV_2O_5 the eigenvector somewhat differs. The V oscillation is more oriented in x direction, while O2 has a larger z component, i.e. it vibrates more clearly towards the adjacent V site of the neighboring ladder. The O1 movement is hardly present, while O3 has got a considerable contribution in z direction. The latter also explains the comparably high frequency in CaV_2O_5, in spite of the smaller ionic charge on the V sites.

An experimental result is also missing for the B_{1u} mode at 483 cm^{-1}. Its eigenvector components show considerable differences to the ones of the respective NaV_2O_5 mode, yet clearly representing a O1–V–O2 bending. One difference consists in the noticeably increased V_x component in CaV_2O_5, while the $O2_x$ contribution is reduced. Also the O3 participation is subject to a modification: While in NaV_2O_5 the in-leg oxygens oscillate almost exclusively in z direction, the same atoms turn out to move diagonally in CaV_2O_5, with the x and z component being very similar. The higher frequency of the CaV_2O_5 mode compared to the NaV_2O_5 case, which is again in contrast to the lower V charge, can be understood by the fact that the V–O2 distance is changed more strongly in the former.

The B_{1u} mode next lower in frequency is located at 348 cm^{-1}. One more time, no corresponding peak is found in the spectra of Ref. [39]. In terms of the eigenvector, the assignment given for the respective NaV_2O_5 vibration is verified for the CaV_2O_5 mode as well, i.e. it also involves an O1–V–O3 bending in combination with an oscillation of the apex oxygen parallel to the rungs. In contrast to NaV_2O_5, the V movement in CaV_2O_5 shows a considerable component in x direction. The O3 atoms in CaV_2O_5 move strictly in x direction and the amplitude of their oscillation is much larger. The eigenfrequency of the CaV_2O_5 oscillation is slightly lower than for the NaV_2O_5 mode, with a difference of about 1.5%.

A frequency decrease of 3% with respect to NaV_2O_5 is also found for the rung-stretching mode of CaV_2O_5 at 282 cm^{-1}. An analysis of the eigenvector components reveals that the in-rung oxygens O1 have got a z component in phase with the one of vanadium, hence the effective kinking of the rungs is only moderate. In turn, the directions of the V, O2, and O3 displacements are changed, i.e the x component is decreased in favor of an increase in z direction. Since this results in a perpendicular motion of the in-leg oxygens O2 with regard to the V atoms, the most characteristic feature consists in a bending of the legs. Compared to the situation in NaV_2O_5, the apex oxygens O3 participate more intensively. Overall, the CaV_2O_5 mode shows a greater intricacy compared to the NaV_2O_5 mode. In this sense, theory also provides a considerable improvement of the mode specification compared to the one in Ref. [39], where this mode was identified as an O–V–O bending. Concerning the infrared reflectivity measurements of Ref. [39], the 282 cm^{-1} mode can be related to a peak detected at 264 cm^{-1}.

The B_{1u} mode lowest in frequency is found at 195 cm^{-1}, which is very close to the peak position at 198 cm^{-1} related to a B_{1u} mode in Ref. [39]. However, the theoretical frequency of a B_{2u} mode with 196 cm^{-1} (Tab. 7.4) is even closer to the experimental peak. Thus from the theoretical point of view no unambiguous symmetry assignment of the experimental mode with 198 cm^{-1} can be done without a calculation of theoretical scattering intensities. The eigenvector of this mode is very similar to the one found in the B_{1u} mode of NaV_2O_5 lowest in energy. In fact, only the oscillation of the apex oxygen O3 differs considerably: While in NaV_2O_5 this atom moves rather parallel to the ladder plane, in CaV_2O_5 its z component is comparable to the x displacement, i.e. it moves diagonally in x - z direction. Regarding the frequencies, a rather large increase is found going from NaV_2O_5 to the Ca compound. This tendency was already found for the A_g phonon dominated by a Ca vibration parallel to c and can similarly be derived from the enhanced ionic charge of Ca^{2+} compared to Na^+.

7.2. B_{2u} modes

7.2.1. NaV_2O_5

The theoretical results for the eigenfrequencies and eigenvectors of the NaV_2O_5 phonon modes with B_{2u} symmetry are presented in Tab. 7.3 and Fig. 7.2, respectively. Experimentally, a relatively large number of infrared reflectivity measurements can be found in literature. References [37, 40, 38] actually present a complete table of B_{2u} modes, while in Refs. [90, 91, 36] three of the four modes predicted by factor group analysis are reported. Column one of the experimental data, referring to Ref. [90], contains the modes interpreted as B_1 modes in this reference, because space group $P2_1mn$ was assumed for NaV_2O_5. They are obtained from reflectivity spectra for $\vec{E} \parallel vecb$, which implies that they actually correspond to

Theory	Experiment					
	Ref. [90]*	Ref. [40]	Ref. [91]	Ref. [36]	Ref. [37]	Ref. [38]
562	587	586	582	584	582	580
386	367	371	372	365	370	366
231	–	225	–	–	230.5	230
174	587	177	177	175	178	176

ω	Eigenvector					Assignment	
.	$V1_y$	$Na1_y$	$O1_y$	$O2_y$	$O3_y$	Refs. [37]	This work
562	0.25	0.00	0.03	-0.43	-0.03	V-O2 stretching	V-O2 stretching
386	-0.22	-0.04	0.54	-0.10	0.20	V-O1-V bending	O1-V-O3 bending
231	-0.12	0.01	-0.24	-0.11	0.44	Na ∥ b	O3 *vs* ladder shear
174	0.21	-0.60	0.02	0.11	0.11	O-V-O bending + Na ∥ b.	Na ∥ b

Table 7.3.: Upper table: Calculated eigenfrequencies (cm^{-1}) of the B_{2u} phonon modes of NaV_2O_5 compared to experimental results from literature. Lower table: Theoretical eigenvector components and assignment of the phonon modes compared to the assignment of Ref. [37]. Details are explained in the text.

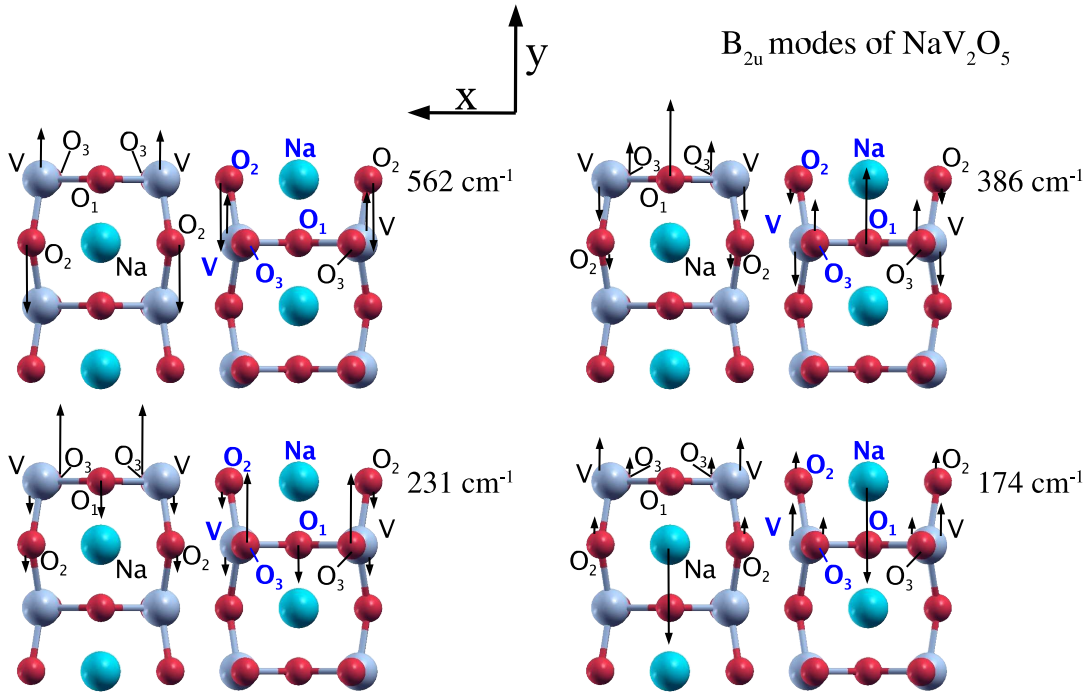

Figure 7.2.: B_{2u} eigenmodes of NaV_2O_5. The arrows show the direction and magnitude of the atomic displacements for each eigenmode.

B_{2u} modes.

The highest calculated frequency for a NaV_2O_5 phonon mode with B_{2u} symme-

try is found at 562 cm^{-1}, which is about 3% below the experimental value. The corresponding eigenvector allows an unambiguous assignment as V–O2 stretching, where the V–O2 pairs constituting the legs change their bond length. All other atoms do virtually not participate in this eigenmode. The frequency is, however, considerably lower than the ones of the V–O2 stretching modes with B_{1g} and B_{3g} symmetry, respectively, where in both cases an experimental peak located at 685 cm^{-1} is reported. This can be understood by the fact that the y displacements of the V atoms, which are much heavier than the oxygens, is much larger in the B_{2u} mode.

For the B_{2u} mode second highest in energy an experimental frequency of about 370 cm^{-1} is presented in literature. The theoretical result for this phonon is found at 386 cm^{-1}, i.e. about 4% above experiment. Regarding the mode assignment, theory provides a better insight into the nature of this oscillation. While Ref. [37] speaks about a V–O1–V bending, we find an additional O3 contribution comparable in amplitude to the O1 movement. In detail, O1 and O3 oscillate synchronously against the V atom, while the in-leg oxygens O2 follow their V neighbors.

A perfect agreement between theory and experiment is found for the B_{2u} mode next lower in frequency, where our calculations as well Refs. [40, 37, 38] report a value of about 230 cm^{-1}, while no corresponding peak is found in the spectra of Refs. [90, 91, 36]. The eigenvector of this phonon mode consists in an oscillation of the apex oxygens against V, O1, and O2, thus representing a shear of O3 versus the ladder atoms. The Na atoms, on their part, do not contribute to this mode, which is in contrast to the assignment in Ref. [37], where a movement of Na parallel to b is reported.

Instead, a strong oscillation of Na $\parallel$ b is found for the B_{2u} mode at 174 cm^{-1}. Here, in turn, the additional O–V–O bending described in Ref. [37] can not be verified. In fact, V, O2 and O3 move simultaneously in y direction, why the in-leg oxygens O1 hardly participate. As for the 230 cm^{-1} mode, also here an excellent agreement between the calculated eigenmodes and experiment is found. In fact, peaks between 175 and 178 cm^{-1} are detected in corresponding spectra presented in literature.

7.2.2. CaV_2O_5

The B_{2u} modes of CaV_2O_5 are presented in Table 7.4, which contains the eigenvectors obtained from theory together with a comparison of the theoretical eigenfrequencies with the experimental data from Ref. [39]. In addition, column two of the experimental results (marked with *) contains the peaks identified as B_{2u} peaks on the basis of a re-interpretation of the experimental spectra due to theory.

For the V–O2 stretching, representing the B_{2u} mode highest in frequency, our calculations give a result of 550 cm^{-1}, while Ref. [39] assigns a peak at 578 cm^{-1} B_{2u} symmetry. This assignment is, however, not unambiguous, since theory pre-

Theory	Experiment	
	[39]	[39]*
550	578.6	515
401	368.6	408
229	–	–
196	122.6	198

ω	Eigenvector					Assignment	
.	$V1_y$	$Ca1_y$	$O1_y$	$O2_y$	$O3_y$	Refs. [39]	This work
550	0.26	0.01	-0.01	-0.43	-0.04	V-O2 stretching	V-O2 stretching
401	-0.16	-0.10	0.58	-0.13	0.19	V-O1-V bending	O1-V-O3 bending
229	-0.16	0.06	-0.21	-0.13	0.43	Ca ∥ b	O3 *vs* ladder shear
196	0.23	-0.56	-0.06	0.11	0.16	O-V-O bending + Ca ∥ b	Ca ∥ b

Table 7.4.: Upper table: Calculated eigenfrequencies (cm^{-1}) of the B_{2u} phonon modes of CaV_2O_5 compared to experimental results from literature. Lower table: Theoretical eigenvector components and assignment of the phonon modes compared to the assignment of Ref. [37]. Details are explained in the text.

dicts an additional infrared active B_{1u} phonon at 559 cm^{-1}, which is even closer to the 578 cm^{-1} peak of Ref. [39]. In this case, a somewhat lower peak at 515 cm^{-1} would be the best candidate for the V–O2 stretching mode. The eigenvector components of this vibration are almost identical to the ones found for the NaV_2O_5 mode with 562 cm^{-1}. A difference in frequency of about 2% is consistent with the weaker Coulomb attraction in CaV_2O_5 due to the smaller charge of the V ions.

An analysis of the spectra given in Ref. [39] in the light of theory also leads to a new finding with regard to the B_{2u} mode second highest in energy. In Ref. [39] a peak at 368 cm^{-1} is interpreted as B_{2u} mode, while a peak at 408 cm^{-1} is described as B_{3u} oscillation. In contrast, the calculated eigenmodes imply that this assignment is switched, i.e. the B_{2u} mode with 401 cm^{-1} is related to the peak higher in frequency, while the peak at 368 cm^{-1} corresponds to the theoretical B_{3u} frequency of 367 cm^{-1}. The eigenvector corresponding to 401 cm^{-1} represents an O1–V–O3 bending, as it is also the case for the respective NaV_2O_5 mode. Compared to the latter, the V_y component is smaller in the CaV_2O_5 case. This also provides an explanation for the frequency increase by about 10%, since the displacement of V, the heaviest element in the considered compound, is replaced by components of lighter atoms. The metal ions, on their part, participate considerably in the calcium compound, while in NaV_2O_5 hardly any contribution from Na is present.

Also the ladder-shear mode comprises a change in the V and Na/Ca components comparing NaV_2O_5 with CaV_2O_5. Here, in contrast to the previous mode,

both, the V and the Ca contributions, are larger compared to their counterparts in NaV_2O_5, at the expense of O1 and O3, which oscillate with a smaller amplitude. This does, however, not affect the main characteristics of the mode, i.e. the shear of the apex oxygens with respect to the ladder atoms. Thus, the assignment of this mode in Ref. [39], where it is identified as "Ca ∥ b" motion, is not verified by theory. The theoretical eigenfrequency of 229 cm^{-1} is very close to the result for NaV_2O_5, differing less than 1%. Since the lower charge of the V ions in CaV_2O_5 together with larger eigenvector components of the heavier elements (V and Ca) would imply a lowering of the frequency, a competing mechanism must be involved. In fact, the relevant feature in this context is the slight out-of-phase motion of Ca with respect to the ladder, which induces an increased back-driving force in this oscillation.

Consistent with the findings for NaV_2O_5, the main feature of the B_{2u} mode lowest in frequency is an oscillation of the metal ion in y direction against the rest of the ladder. The fact that the different metal ions—Ca^{2+} and Na^{+}, respectively—carry different electronic charges, plays an important role. It leads to a much stronger interaction between the negatively charged oxygen atoms with the Ca ion compared to the Na ion. As a result, the frequency of 196 cm^{-1} for the CaV_2O_5 mode is about 12% higher than the one of the corresponding B_{2u} mode in NaV_2O_5, in spite of the larger atomic mass of Ca. The change in the eigenvector going from NaV_2O_5 to CaV_2O_5 is rather small. The main differences in the latter consist in a stronger participation of the apex oxygens O3 together with a non-vanishing component of the in leg-oxygen O1. Regarding the experimental results presented in Ref. [39], another time theory implicates a re-assignment of the peak symmetries. Instead of the 122.6 cm^{-1} peak, we propose that the 198 cm^{-1} peak is the one corresponding to the B_{2u} mode lowest in frequency, while we suggest that the former peak is related to the B_{3u} vibration with a theoretical frequency of 114 cm^{-1}.

7.3. B_{3u} modes

7.3.1. NaV_2O_5

Figure 7.3 and Table 7.5 present the eigenvectors and eigenfrequencies of the B_{3u} modes of NaV_2O_5 in comparison with experimental results from literature. The measured data presented in Refs. [90, 91, 37, 36, 38, 40] are rather heterogeneous and differ considerably for some of the eigenmodes under consideration. Nevertheless, a rather large number of published infrared reflectivity spectra with polarization $\vec{E} \parallel \vec{a}$ exists. For this reason, a comparison of the different references together with the theoretical findings allows a re-interpretation of the spectra in Refs. [37, 40], where a second column with a new peak assignment (marked with *) is added. As previously discussed, the results of Ref. [90], which where originally

Theory	Experiment							
	Ref. [90]*	Ref. [40]	Ref. [40]*	Ref. [91]	Ref. [36]	Ref. [37]	Ref. [37]*	Ref. [38]
944	–	938	938	940	–	940	940	940
675	526	740	518	505	525	505	505	522
445	–	518	–	469	–	469	469	–
409	–	–	–	436		438	438	–
255	251	246	246	254	251	254	254	252
145	145	137	137	140	153	144	144	146.7
92	(90)	90	90	–	(90)	138	–	

ω	Eigenvector								Assignment	
	V_x	V_z	Na_x	$O1_x$	$O2_x$	$O2_z$	$O3_x$	$O3_z$	Refs. [37]	This work
944	-0.04	0.25	0.01	0.01	-0.00	-0.01	0.05	-0.43	V-O3 stretching	V-O3 stretching
675	-0.06	-0.07	-0.01	0.64	-0.18	0.05	-0.02	-0.03	V-O1 stretching	O1 ∥ a
445	-0.27	0.05	0.02	0.19	0.36	-0.13	0.04	0.06	V-O2 stretching	O2-V-O1 bend. ∥ a
409	0.11	0.21	-0.03	0.06	-0.11	-0.40	-0.09	0.11	O-V-O bending	V-O2 bend. ∥ c
255	-0.12	0.11	-0.05	-0.06	-0.16	0.00	0.40	0.12	O-V-O bending	V-O3 bending
145	0.13	0.01	-0.65	0.08	0.11	0.03	0.04	-0.01	Na ∥ a	Na ∥ a
92	-0.01	-0.35	-0.04	-0.07	-0.03	-0.26	0.12	-0.18	chain transl. ∥ c	chain rotation

Table 7.5.: Upper table: Calculated eigenfrequencies (cm^{-1}) of the B_{3u} phonon modes of NaV_2O_5 compared to experimental results from literature. Lower table: Theoretical eigenvector components and assignment of the phonon modes compared to the assignment of Ref. [37]. Details are explained in the text.

analyzed in terms of the space group $P2_1mn$. Therfore the modes measured with light polarized $\parallel \vec{a}$ (originally labeled A_1) are shown in column two of Tab. 7.5.

For the B_{3u} mode highest in frequency the situation seems to be clear. Even though not in all references a corresponding peak is detected, Refs. [91, 37, 38, 40] consistently report a B_{3u} mode of about 940 cm^{-1}, which is in excellent agreement with the theoretical result of 944 cm^{-1}. The assignment is unambiguous: Reference [37] in agreement with theory identifies this mode as a V–O3 stretching. Compared with the V–O3 stretching vibrations with A_g, B_{2g}, and B_{1u} symmetry, respectively, the energy of the B_{3u} mode is slightly lower.

For the B_{3u} mode with a theoretical frequency of 675 cm^{-1} the comparison with experiment turns out to be difficult, and no good agreement is found. Reference [40] reports a weak signal at 740 cm^{-1}, which, however, is not verified by the other experiments, such that we assume that the peak at 518 cm^{-1} is the one related to the B_{3u} mode second highest in energy. Thus, among the measured peaks on the one hand candidates with a frequency of 505 cm^{-1} ([91, 37, 38]), and on the other hand peaks in the range between 518 and 526 cm^{-1} (Refs.[40, 38, 36, 90]), respectively, are left. In addition, experiment shows a very pronounced and rather broad shoulder between 550 and 620 cm^{-1}. As stated in Refs. [90, 46] and con-

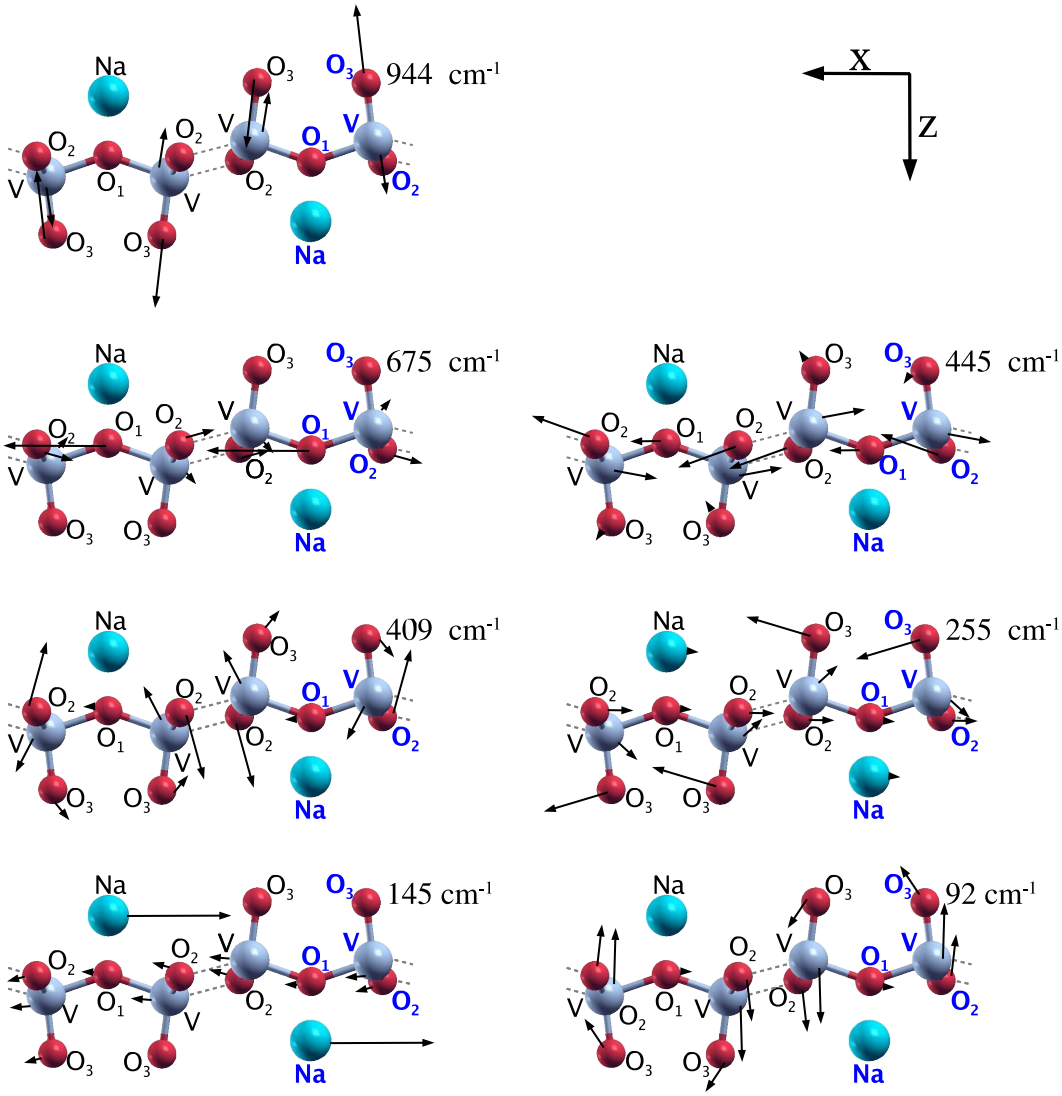

Figure 7.3.: B_{3u} eigenmodes of NaV_2O_5. The arrows show the direction and magnitude of the atomic displacements for each eigenmode.

firmed by Ref. [37], it can be identified as continuum feature, also present in the room temperature Raman spectra of NaV_2O_5, which possibly results from an electronic level splitting of the V $3d$ states induced by the crystal field. This means that the experimental spectra are superposed with effects not directly related to the B_{3u} phonons, thus making the assignment of the phonon frequencies more difficult. In terms of the eigenvector assignment, the identification as V–O1 stretching given in Ref. [37] is roughly confirmed. In fact, theory shows that the stretching is induced by a clearly dominating $O1_x$ movement in rung direction, such that we propose to describe the mode as an oscillation of O1 $\parallel$ a.

The B_{3u} mode at 445 cm^{-1} agrees relatively well with the experimental findings. Actually, Refs. [91, 37] both report a peak of infrared reflectivity spectra (polarization $\vec{E} \parallel \vec{a}$) at 469 cm^{-1}, which is about 5% above the theoretical value. Regarding the characterization of this phonon mode, the calculated eigenvector allows a further specification of the result presented in Ref. [37]. In detail, it shows that the V–O2 bending takes place in the x–y plane and that also the in-rung oxygens participate.

In contrast, the V–O2 bending with a frequency of 409 cm^{-1} is due to displacements of the involved atoms in z direction. A stretching of the V–O3 bond is, however, avoided since the apex oxygens, to some extent, follow the motion of the vanadium atoms. Experimentally, this B_{3u} mode is present in the references (Refs. [91, 37]) reporting a peak located at 438 cm^{-1}.

The experimental situation is even clearer for the O–V–O bending mode next lower in frequency. All Refs. [90, 40, 91, 36, 37, 38] report a frequency between 246 and 254 cm^{-1}, which is in perfect agreement with the theoretical result of 255 cm^{-1}. One more time the eigenvector components obtained by theory allow an extension of the assignment given in Ref. [37], showing that V and O3 give the main contribution for the bending, while the in-leg oxygens O2 oscillate less intensively. Moreover, Na and O1 have got a small x component in-phase with V and O2.

For the B_{3u} vibration at 145 cm^{-1}, the measured counterparts are found in a relatively large range from 137 cm^{-1} (Ref. [40]) to 153 cm^{-1} (Ref. [36]). However, three of the references ([90, 37, 38]) consistently report a frequency of about 145 cm^{-1}, which is again in excellent agreement with theory. The characterization of this mode is unambiguous, assigning it an oscillation of Na parallel to a. In this point the description due to theory and the one given in Ref. [37] are fully compatible.

The B_{3u} mode lowest in frequency appears to be more challenging in terms of assignment. While Ref. [37] reports a chain translation parallel to the c axis, the theoretical eigenvector gives a quite different picture. It clearly shows a chain rotation, where each leg moves in-phase with the adjacent leg of the neighboring ladder in c direction, but out-of-phase relative to the other leg of the same ladder. The Na atoms, on their part, hardly contribute to this eigenmode. Concerning measured infrared reflectivity spectra, the situation is not unambiguous. While this mode appears in no measurement at room temperature, Refs. [90, 40, 36] report a peak at 90 cm^{-1} for the spectra obtained at 40 K, which is still about 5 K above the critical temperature of the phase transition. At the other hand, Ref. [37] presents a peak at 138 cm^{-1}, i.e. only 6 cm^{-1} below the the next higher B_{3u} mode. This mode, however, is not measured, but obtained from a fitting procedure of the non-polarized reflectivity spectrum. For this reason and since also theory predicts a frequency of 92 cm^{-1}, we assume that actually the 90 cm^{-1} peak detected in the experiments at $T = 40K$ represents the lowest-energy peak

of the B_{3u} mode.

7.3.2. CaV_2O_5

Theory	Experiment	
	Ref. [39]	Ref. [39]*
845	892	892
658	515	–
479	408	–
367	–	386
229	244	–
174	–	–
114	–	122

ω	Eigenvector								Assignment	
	V_x	V_z	Ca_x	$O1_x$	$O2_x$	$O2_z$	$O3_x$	$O3_z$	Refs. [39]	This work
845	-0.05	0.24	0.02	-0.01	0.01	-0.00	0.06	-0.43	V-O3 stretching	V-O3 stretching
658	-0.18	-0.07	-0.01	0.63	-0.10	0.01	-0.01	-0.03	V-O1 stretching	O1 ∥ a
479	-0.24	0.03	0.01	0.00	0.41	-0.14	-0.02	0.05	V-O2 stretching	O2-V-O1 bend. ∥ a
367	0.12	0.24	-0.03	0.06	-0.09	-0.38	-0.10	0.11	O-V-O bending	V-O2 bend. ∥ c
229	-0.13	0.08	-0.09	-0.03	-0.09	-0.04	0.44	0.12	O-V-O bending	V-O3 bending
174	0.20	-0.02	-0.58	0.07	0.17	0.06	0.00	-0.05	Ca ∥ a	Ca ∥ a
114	-0.07	-0.34	-0.06	-0.07	-0.09	-0.28	0.03	-0.18	chain transl. ∥ c	chain rotation

Table 7.6.: Upper table: Calculated eigenfrequencies (cm^{-1}) of the B_{3u} phonon modes of CaV_2O_5 compared to experimental results from literature. Lower table: Theoretical eigenvector components and assignment of the phonon modes compared to the assignment of Ref. [37]. Details are explained in the text.

Table 7.6 shows the theoretical B_{3u} eigenmodes of CaV_2O_5 together with the experimental results from Ref. [39]. In this work, unpolarized far-infrared reflectivity spectra are measured and the symmetry assignment is done by relating each peak to the peak of a polarized NaV_2O_5 spectrum closest in frequency. Since the theoretical results indicate a different symmetry assignment for some of the measured CaV_2O_5 frequencies, in Tab 7.6 a second column with the re-interpreted spectra in the light of theory is added (marked by *).

As in NaV_2O_5, the B_{3u} mode highest in frequency represents a V–O3 stretching. In fact, the respective eigenvector of both compounds is virtually identical, while the frequency in CaV_2O_5 (845 cm^{-1}) is considerably lower, which is consistent with the findings for the V–O3 stretching modes with A_g, B_{2g}, and B_{1u} symmetry. Compared to the measured peak at 892 cm^{-1}, the calculated phonon energy is about 5% lower.

A frequency decrease of about 3% compared to the NaV_2O_5 case is found for the V–O2 stretching mode with B_{3u} symmetry ($\omega = 658$ cm^{-1}). As for the previous mode, the smaller charge of the V ion and a hence smaller Coulomb interaction accounts for this frequency change. The comparison with experiment turns out to be rather difficult. The measured spectra only provide a peak at 515 cm^{-1}, which, however, is closer to a theoretical B_{2u} mode. Comparing the contributions of the different atoms with the situation in NaV_2O_5, it turns out that the V atoms show a noticeably larger x component at the expense of the O2 movement, where a considerable decrease in amplitude is found. Nevertheless, the main characteristic is a very dominant motion of the in-leg oxygen in rung direction.

The B_{3u} mode at 445 cm^{-1} comprises a strong bending of the leg, caused by displacements of V and the in-leg oxygen O2 with the main component in x direction. As opposed to the respective NaV_2O_5 mode, the in-rung oxygens do not contribute at all in CaV_2O_5, while O2 participates even more. Thus we identify this mode as pure V–O2–V bending, which is in contrast to the assignment given in Ref. [39], where a V–O1–V bending is reported. In spite of the smaller V charge, a frequency increase from 445 cm^{-1} to 479 cm^{-1} is found going from NaV_2O_5 to the Ca structure. In connection with the predominance of the O2 and V displacements, a correlation with results for phonon modes with other symmetries is evident, where it turns out that the V–O2 bending involves a higher energy than oscillations changing the V–O1 bond. Regarding the symmetry assignment, theory once more implicates interpretation of the peaks presented in Ref. [39]. Even though in the cited reference a 408 cm^{-1} peak is described as the B_{3u} feature, we find that it agrees much better with a B_{2u} mode situated at 401 cm^{-1}, as already described in Section 7.2.2.

In turn, the theoretical results indicate that the 386 cm^{-1} peak—associated with a B_{2u} mode in Ref. [39]—more probably represents the $\mathbf{B_{3u}}$ mode next lower in frequency, with a theoretical frequency of 367 cm^{-1}. Regarding the characterization of this eigenmode, the calculated eigenvector of CaV_2O_5 is different from the one presented in Ref. [39]. In this paper, the 386 cm^{-1} mode is portrayed as V–O1–V bending, while the theoretical eigenvector represents a V–O2–V bending in the x–y plane. In fact, its components are very similar to the ones of the corresponding NaV_2O_5 mode. On the other hand, the frequency of the NaV_2O_5 vibration is about 10% higher. The reason for this are both the greater charge of the V ions in the Na compound as well as its somewhat smaller displacements of the heavy V atoms.

A lower energy in comparison with the respective NaV_2O_5 mode is also found for the V–O3 bending of CaV_2O_5: While for the former structure a frequency of 255 cm^{-1} is obtained, for the latter we find a value of 229 cm^{-1}. This frequency shift is not only a consequence of the smaller Coulomb interaction exerted by the V ions, but also due to a considerable participation of Ca, with its relatively large atomic mass. In general, several eigenvector components of the V–O3 bending

in CaV_2O_5 are slightly altered with respect to NaV_2O_5, yet not affecting the main character of this eigenmode. On the experimental side, the interpretation of the 244 cm^{-1} peak in the unpolarized IR reflectivity spectra as B_{3u} mode is not supported by theory, since a B_{1u} mode at a theoretical frequency of 235 cm^{-1} fits the measurements much better (see Sect. 7.1.2).

For the B_{3u} mode with a frequency of 174 cm^{-1} no experimental counterpart is found. The main feature of this eigenmode consists in a strong oscillation of the metal atom Ca in x direction, which is, however, reduced compared to the Na motion in NaV_2O_5. In turn, the motion of both the V atoms and the in-leg oxygens O2 is more pronounced in calcium vanadate. This feature also accounts for the considerably higher frequency in CaV_2O_5, since it involves much stronger bonds compared to the rather loosely bound metal ion.

A similar frequency shift going from NaV_2O_5 to CaV_2O_5 is also found for the B_{3u} mode lowest in frequency. While the corresponding eigenfrequency for the former is about 90 cm^{-1}, for the latter it is more than 20% higher, i.e. 114 cm^{-1}. This effect can be attributed to a more pronounced kink-like deformation of the legs in the CaV_2O_5 eigenmode due to a different amplitude of the V and O2 oscillations. In order to understand this distortion one has to take into account that not the eigenvector components themselves are proportional to the amplitude of the atomic displacements, but the components weighted by the square root of the corresponding atomic mass. Therefore a $O2_x$ component of -0.09 corresponds to a displacement about twice as large as the one related to a V_x component of 0.07. Even though reference [39] does not explicitly report a frequency for this mode, theory indicates that the peak located at 122 cm^{-1} in experimental spectra is related to a phonon mode with B_{3u} instead of B_{2u} symmetry, as originally assumed. In fact the lowest B_{2u} mode is is found at a theoretical frequency of 196 cm^{-1}, while the frequency of the lowest B_{3u} mode (114 cm^{-1}) is in much better agreement with the discussed peak.

8. Electronic and Optical Properties

8.1. Electronic properties

8.1.1. NaV_2O_5

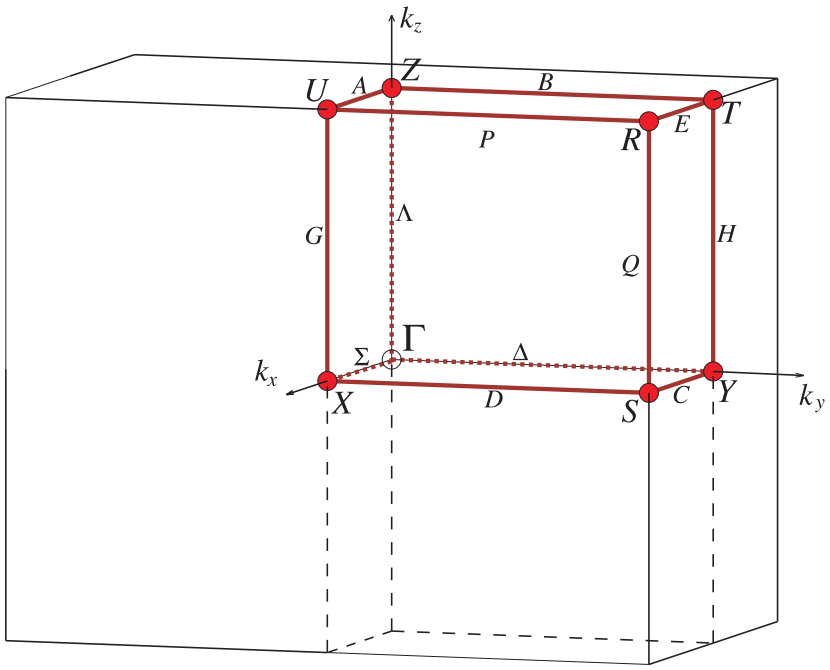

Figure 8.1.: Brillouin zone and high symmetry points for space group $Pmmn$ (59), i.e. for NaV_2O_5 (T>T_c) and CaV_2O_5. The figure is taken from Ref. [96]. The band structures presented in this section are calculated for the $\vec{k}$ path $Y-\Gamma-X-S-\Gamma-Z-U-R-Z-T$.

The Brillouin zone of the space group no. 59 ($Pmmn$), including high symmetry points, is shown in Fig. 8.1, while the band structure and atomic densities of states (DOS) for the relaxed structure of NaV_2O_5 are presented in Fig. 8.2. The band structure is characterized by two about 1 eV wide conduction bands bisected by the Fermi level. An analysis of the electronic structure in terms of atomic densities of states exhibits that this pair of bands is almost exclusively formed by V states. Only a small admixture of O2 states with $2p_x$ character can be

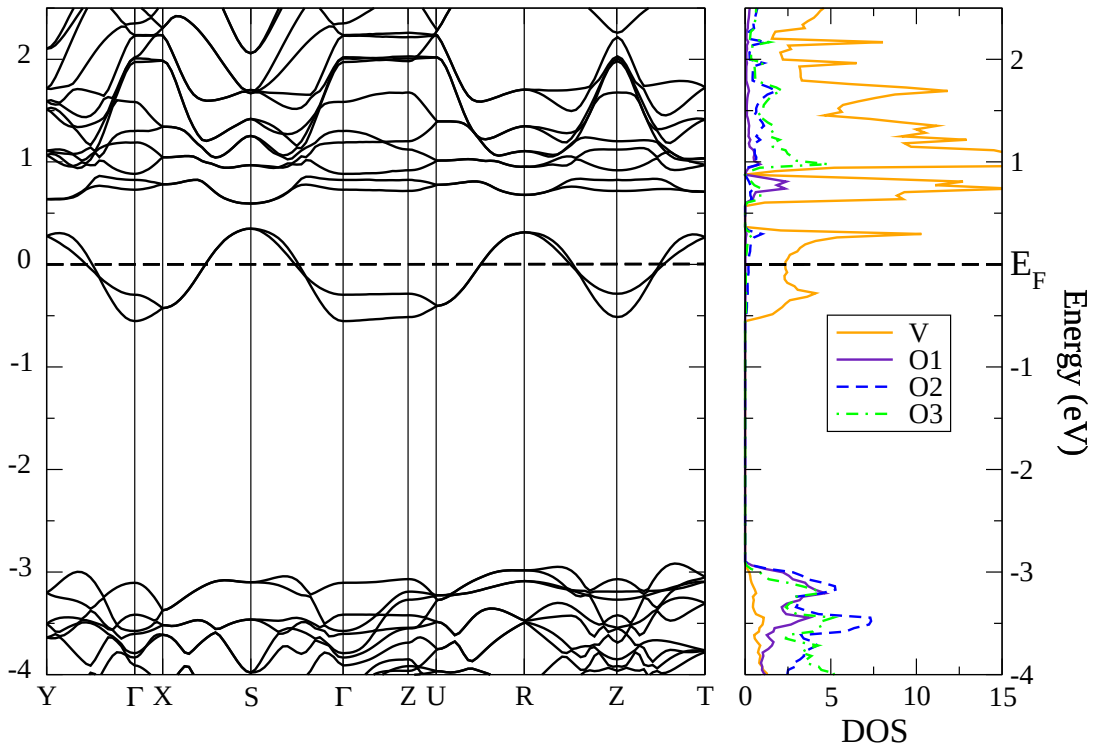

Figure 8.2.: Band structure and density of states of NaV_2O_5. The displayed energy range includes the upper valence bands with O $2p$ character, the V d_{xy} states around E_F and some more conduction bands dominated by V states, while no Na states are found in this range.

detected, which, however, is centered above E_F. In detail, the bands are mainly build up of V d_{xy} states, as can be seen in the partial densities of states presented in Fig. 8.3, in agreement with the findings in Refs. [97, 98, 32, 99, 100]. Actually, the considered bands intersecting the Fermi level in k_y direction originate from the bonding combination of V d_{xy} states. Their dispersion is due to hopping along the ladders, while the splitting of this pair of bands at the Γ point is due to inter-ladder hopping, as it is discussed in Sect. 5.1 and in Ref. [100]. The inter-ladder hopping is also responsible for the band crossing of the V d_{xy} bands in b direction close to E_F [32].

Looking at different parts of the Brillouin zone, a strong dispersion is found for the section of the $\vec{k}$ path leading from the Y point to Γ and the one between X to S, respectively. Between Y and Γ the splitting is noticeable, while the two bands virtually coincide between X and S. The splitting increases again going from S back to the Γ point. Continuing the $\vec{k}$ path from the Γ point in k_z direction, the bands hardly show any curvature and consequently keep their separation found at Γ, which is about 0.15 eV. Moving from Z in k_x direction to the U point,

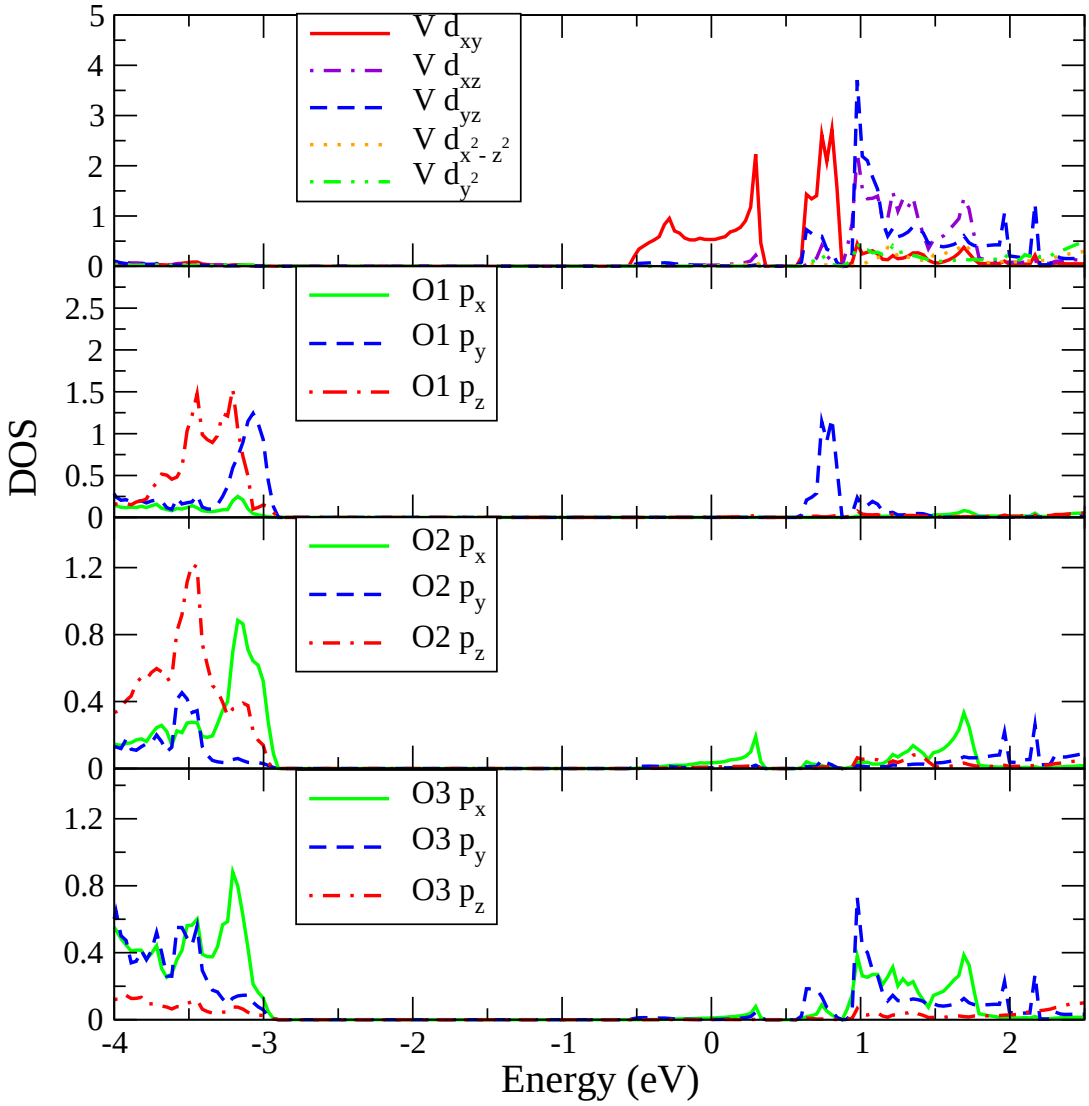

Figure 8.3.: Partial densities of states of NaV_2O_5, showing the orbital character of the V $3d$ and the O $2p$ bands. In the considered energy range, no sodium states are encountered.

the splitting reduces another time, while the bands are as dispersive as they are between Γ and X. In effect, the features of the bands for the points lying in the $k_z = \pi/c$ plane are almost identical with the ones previously found for the corresponding $\vec{k}$ points in the $k_z = 0$ plane. This means, that the band structure of the V $3d_{xy}$ bands between Z, U, R and back to Z resembles the structure found between Γ, X, S, and Γ, while the dispersion between Z and T correlates with the one going from Γ to the Y point. The maximum of the discussed bands is found at X, why the minimum is located at the Γ point. The reported findings

in terms of dispersion in a, b, and c direction, respectively, are consistent with the descriptions in Refs. [98, 32, 99, 100]. As pointed out in Ref. [101], the two partially degenerate half-filled narrow conduction bands crossing E_F are very similar to the corresponding bands in $GeCuO_3$ (Ref. [102]), the first inorganic spin-Peierls compound. The band structure also bears great resemblance to the chemically equivalent LiV_2O_5 [103], even though differing due to a splitting of the V conduction bands at X and T.

The two conduction bands next higher in energy, separated by a 0.25 eV gap from the V $3d_{xy}$ bands around the Fermi level, represent their anti-bonding counterpart. Consequently, they are also dominated by V $3d_{xy}$ character, with a moderate contribution from oxygen O $2p_x$ and $2p_z$ states. The latter are mainly derived from the in-rung oxygen O1, but to a small extent from O2 and O3, respectively. The dispersion of these bands is in general very flat, with weakly pronounced maxima between Y and Γ, X and S, as well as X and Γ. The corresponding maxima in the $k_z = \pi/c$ plane are even hardly visible. The minimum of the higher lying conduction bands is found at S, i.e. opposite to the band maximum of the bands around E_F. As it is the case for the dispersion, also the band splitting is very small for the anti-bonding V $3d_{xy}$ bands.

The conduction bands next higher in energy appear to be detached from the bands discussed above, resulting in a zero gap of the density of states at approximately 0.85 eV. Their dispersion is noticeably larger than the one found for the two lower lying conduction bands, and also their splitting is considerable. In terms of band character, a strong increase of O3 $2p_x$ states is found, while the participation of O1 and O2 is minor. Also the character of the V states changes compared to the conduction bands formerly discussed. Instead of a d_{xy} contribution, a mixture of d_{xz} and d_{yz} states is detected, in agreement with the results of Ref. [32]. Also with respect to the location of the V bands higher in energy (which are not included in Figs. 8.2 and 8.3), the results of the cited reference are mostly verified. We find that the d_{xz} bands are mainly situated at 0.6–2.15 eV, the d_{yz} bands at 0.6–1.8 eV, and the $d_{x^2-z^2}$ and d_{y^2} characters are located in the range from 2.2–4.0 eV, d_{y^2}. However, the contribution of the V d_xz and d_y^2 states, which is exhibited in Fig. 8.2, is not obtained in Ref. [32].

The bands 2.3 eV below the bonding V $3d_{xy}$ bands consist of $2p_x$ states from the in-leg oxygen O2 and the apex oxygen O3 together with O1 $2p_y$ states, which all contribute to a comparable extent.

Dipole transitions between the different bands will be discussed in Section 8.2.1 in comparison with optical conductivity measurements [41, 104, 40, 90, 105, 43].

The influence of the Hubbard term U on the properties of V-based ladder compounds is widely discussed in the literature. It is important to mention that the enhanced electron correlation when accounted for by the Hubbard parameter reproduces the semiconducting behavior with the charge gap close to $2|t_\perp|$ [106]. Correspondingly, the dispersion along the y-axis of the band derived from the bonding combination of V-d_{xy} orbitals will be π rather than 2π periodic (Sect. 5.1

and Refs. [107, 108]). At the same time, we find that in general the physical properties determined by the electron density are not strongly influenced by the Hubbard repulsion and can be reliably described within DFT.

8.1.2. CaV_2O_5

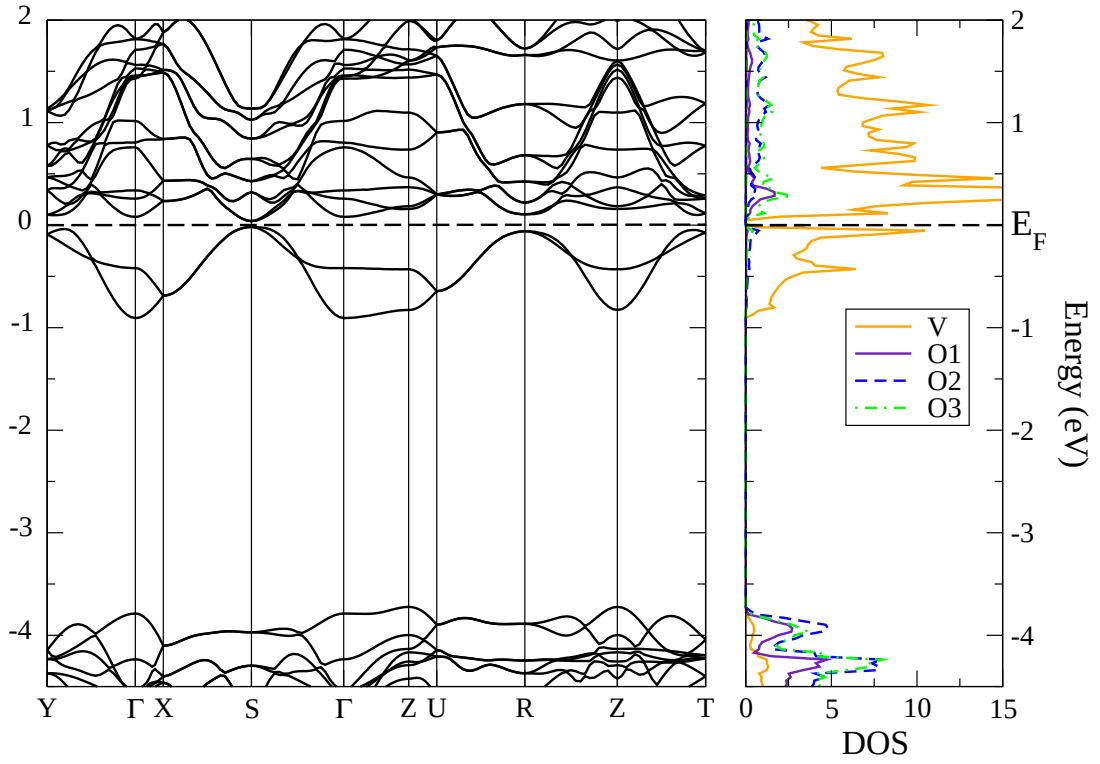

Figure 8.4.: Band structure and atomic densities of states of CaV_2O_5. The displayed energy range comprises the upper valence bands with O $2p$ character, the V d_{xy} states around E_F and some more conduction bands dominated by V states, while no Ca states are found in this range.

Figure 8.4 shows the band structure and atomic densities of states, respectively, for the structure of CaV_2O_5 with relaxed atomic positions, while Fig. 8.5 presents the densities of states in terms of orbital characters. Since CaV_2O_5 is iso-structural to NaV_2O_5, it has the same Brillouin zone, i.e. the one presented in Fig. 8.1. The main striking difference with respect to NaV_2O_5 consists in the shifted Fermi level, which in CaV_2O_5 is located *above* the bonding V $3d_{xy}$ bands, and actually separates them from the corresponding anti-bonding states. Another difference is found in the noticeably altered size of the band widths. Moreover, the gaps between the two pairs of V $3d_{xy}$ bands, on the one hand, and between the

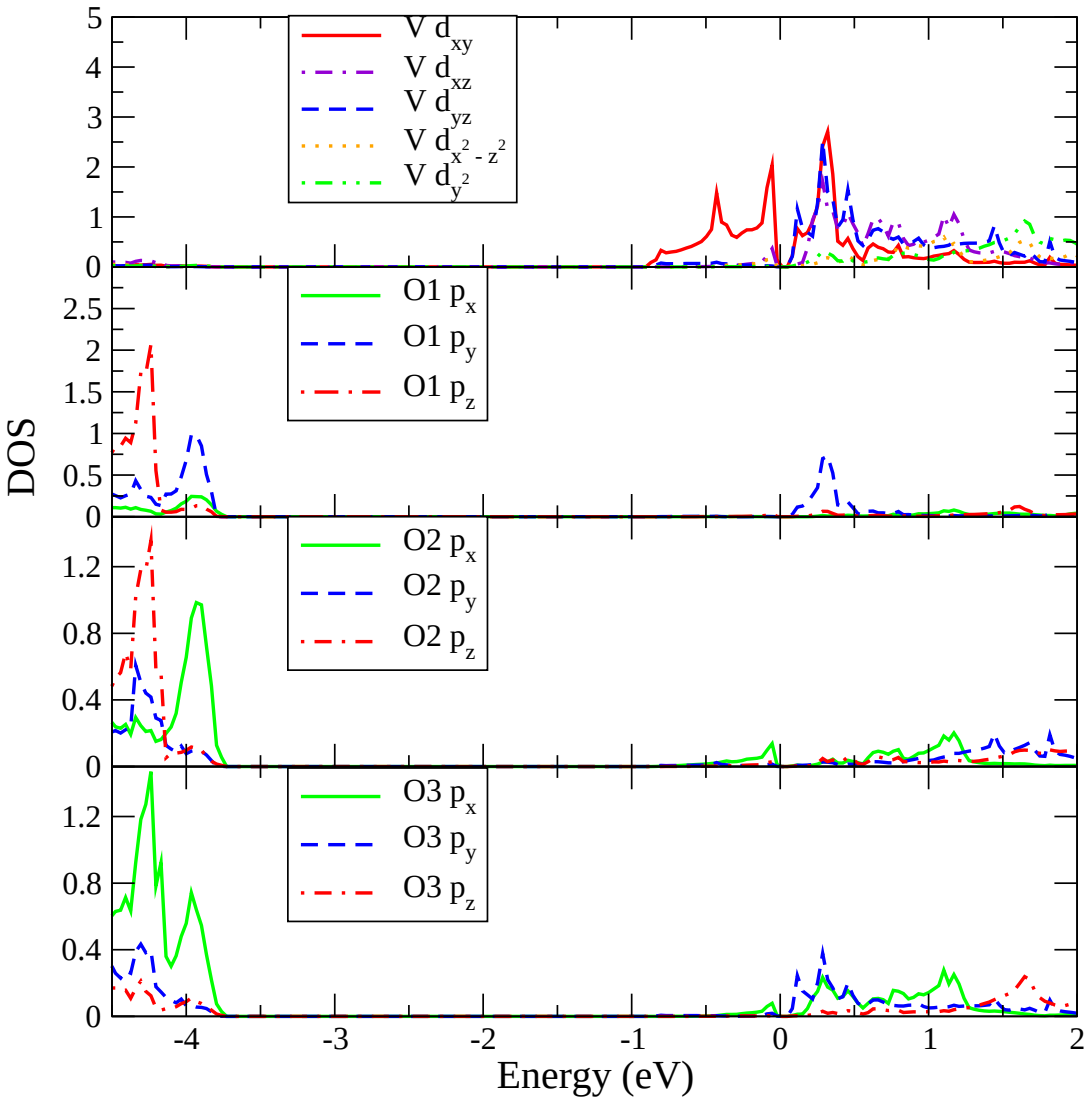

Figure 8.5.: Partial densities of states of CaV_2O_5, showing the orbital character of the V $3d$ and the O $2p$ bands. In the considered energy range, no calcium states are encountered.

lower pair of V $3d_{xy}$ and the O valence bands, on the other hand, changes. While the former gap is 0.25 eV in NaV_2O_5, either pairs of bands in CaV_2O_5 almost touch at X, leaving only a very small gap of 0.03 eV, which is consistent with the results of Ref. [26]. In turn, the separation between the V valence bands just below E_F and the states next lower in energy, which originate from the oxygen atoms, is increased with respect to the sodium compound from 2.3 eV to 2.8 eV. The band width of the V bands below (around) E_F is virtually the same in both vanadates, while their Γ point splitting is by a factor of two larger in CaV_2O_5 (0.5 eV compared to 0.25 eV in NaV_2O_5). This implies, that the inter-ladder

hopping probability and accordingly the interaction between neighboring ladders is higher in CaV_2O_5, as it is discussed in Sect. 10.2. At the same time, the band crossing of the bonding V $3d_{xy}$ bands takes place farther away from the Γ point. For the rest, the characteristics of the discussed bands in terms of dispersion are very similar to the ones of NaV_2O_5, i.e. the bands are most dispersive between $Y - \Gamma$, less dispersive between Γ and X, and almost flat in z direction. Besides the strongly dominating V $3d_{xy}$ character, also O2 and O3 $2p_x$ contribute to the bands below E_F.

Analyzing the anti-bonding conduction bands above the Fermi level, several differences with respect to NaV_2O_5 are exhibited. First of all, they are not separated anymore from higher-lying V $3d$ states. This may be due to a stronger dispersion of the former states with respect to NaV_2O_5. The closing of this gap is in contrast to Ref. [26], which reports a separation of the V d_{xy} states from the V d states higher in energy. Regarding further contributions to the bands above E_F, in CaV_2O_5 the O3 character is stronger than the O1 character, which is clearly the predominating oxygen contribution of these bands in sodium vanadate. Nevertheless, the main feature of the conduction band coincides with the one in NaV_2O_5, i.e. the band is clearly characterized by V $3d_{xy}$ states.

Also for the oxygen-dominated bands at about 4 eV below E_F, many similarities to its NaV_2O_5 counterparts are present. In an analogous way, they are build up by O2 and O3 $2p_x$ states together with an O1 $2p_y$ character, while O1 $2p_z$ states can be found just 0.25 eV below. In turn, the band dispersion is altered qualitatively and quantitatively with respect to NaV_2O_5, yielding considerably larger band widths in the calcium structure. Moreover, the maximum of the oxygen bands is not located between Y and Γ, as in NaV_2O_5, but at the Γ point.

8.1.3. MgV_2O_5

In order to make the band structure better comparable to the one of calcium and sodium vanadate, the same $\vec{k}$ path, i.e. the same Cartesian coordinates in $\vec{k}$ space, as for the other two compounds was used. Accordingly, the high symmetry points of the Brillouin zone are labeled as in the Brillouin zone for the space group 59–*Pmmn*, and *not* according to the labels normally used for the space group 63–*Cmcm*. In terms of of the standard notation for the latter space group, on the one hand the choice of the Cartesian axes is different, namely such that k_x is parallel to the ladders, k_y is parallel to the stacking and k_z is parallel to the rung direction. On the other hand, the labels for high symmetry points of the Brillouin zone used in Fig. 8.6 differs from the *standard* notation, where the relation between these two is given in Tab. 8.1

Figure 8.6 shows band structure and atomic densities of states of MgV_2O_5 for the relaxed structure (upper panel) and the band structure for the system with the experimental atomic positions [28] (lower panel). While for the crystal structure with the experimental atomic positions we find the same band structure as in

This work	Standard notation
Y	Y_1
Γ	Γ
X	Z
S	T_1
Z	Y_2
U	T_2
R	(1/2, 1/2, 1/2)
T	(1/2,1/2,0)

Table 8.1.: Special k points used for the band structure of MgV_2O_5 compared with labels (coordinates) in standard notation and axes orientation.

Ref. [26], it changes considerably for the relaxed positions. The most remarkable difference is found in a strong change of dispersion together with a shift of the anti-bonding pair of V $3d_{xy}$ bands. On the one hand, they are completely detached from their bonding counterparts and strongly overlap with the conduction bands next higher in energy, while, on the other hand, the density of states vanishes at E_F. This is in contrast to the situation for the non-relaxed structure, where a finite density of states is found at E_F, as it can be seen in Fig. 6 of reference [28]. Moreover, the band width and dispersion of the anti-bonding V $3d_{xy}$ changes drastically. While for the structure with experimental atomic positions these bands are rather flat and the band width is only about 0.3 eV, Fig. 8.7 shows that in the relaxed structure they are strongly dispersive and spread over a range of more than 0.7 eV.

A remarkable change in band width is also detected for the bonding V $3d_{xy}$ states just below E_F. While for the un-relaxed structure it is about 1 eV, for the system with relaxed atomic positions it is about 50% larger. In contrast, the gaps at Γ and Z change rather little. The O $2p$ dominated bands 4 eV below E_F show an altered dispersion comparing the band structure of the original experimental structure with the theoretically relaxed one. The dispersion is stronger in former case, while in the other one a crossing of the two O $2p$ bands highest in energy is detected. Nevertheless, the maximum of the O $2p$ bands can be found at almost the same energy for either case.

Comparing the relaxed structures of MgV_2O_5 and the chemically equivalent CaV_2O_5, respectively, the most striking differences consist in the much larger band width of the pair of V $3d_{xy}$ below E_F in MgV_2O_5, and the closing of the gap at the Fermi level.

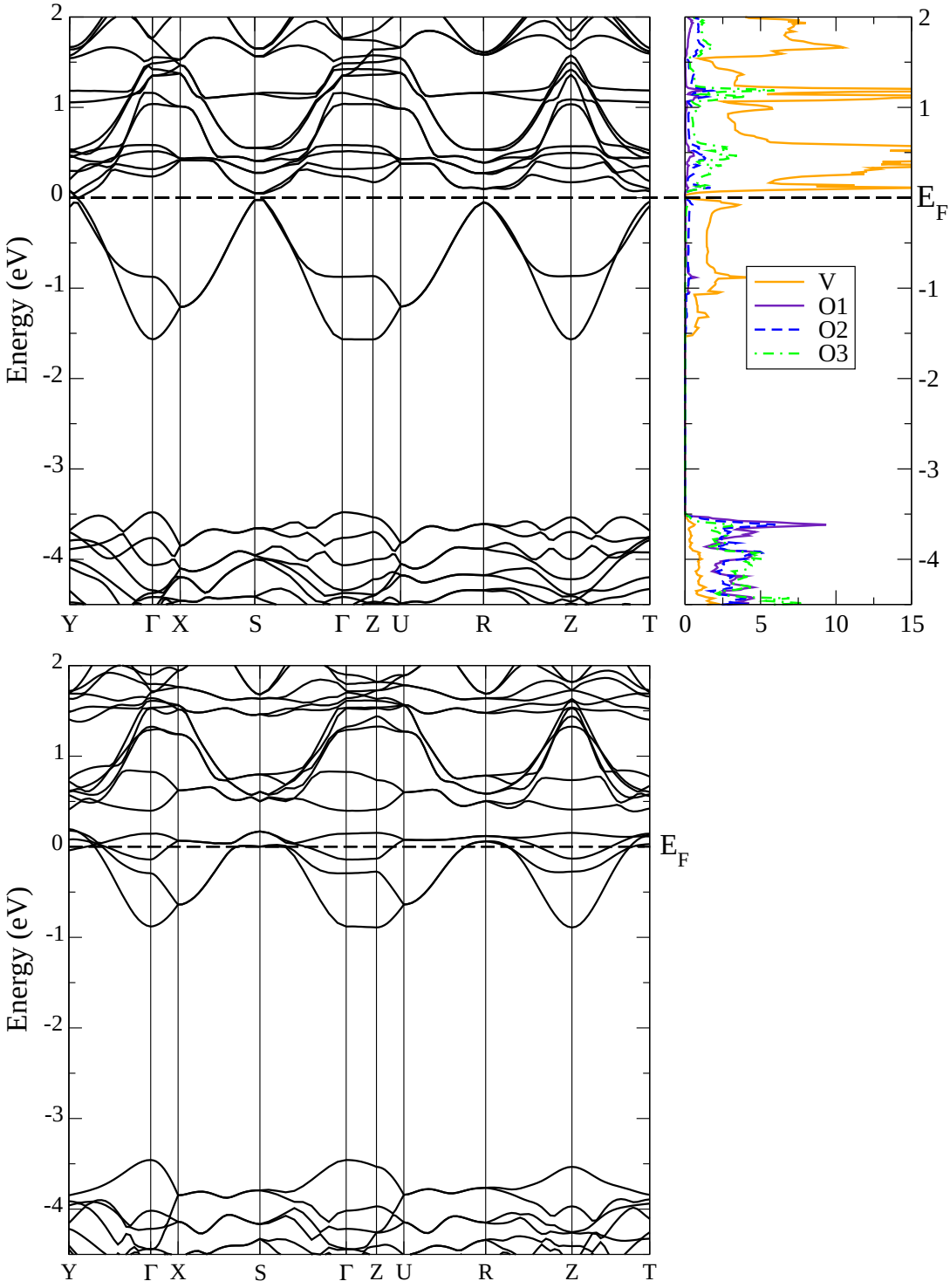

Figure 8.6.: Band structure and atomic densities of states of MgV_2O_5 for relaxed (upper panel) and experimental [28] (lower panel) atomic positions.

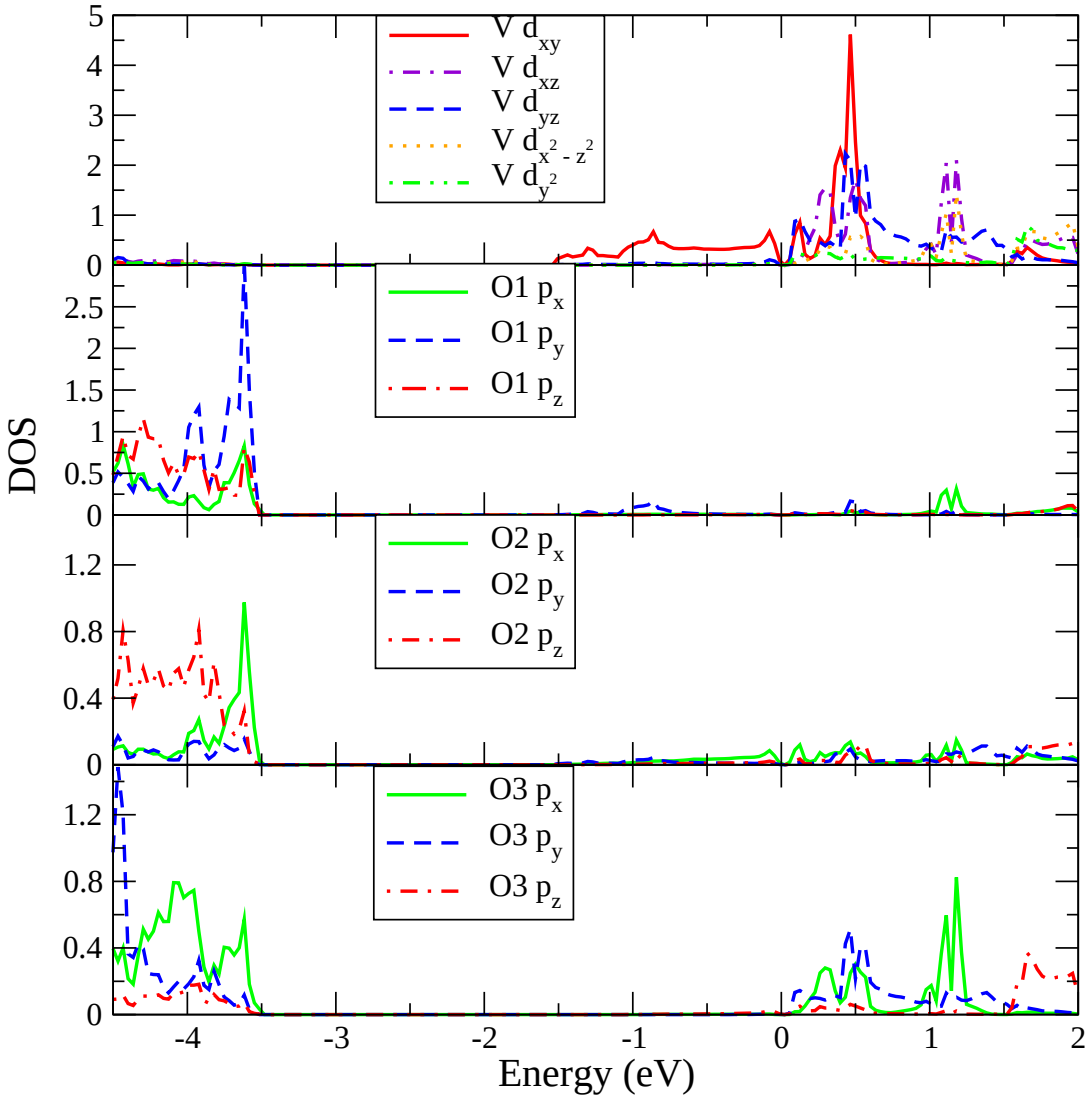

Figure 8.7.: Partial densities of states of MgV_2O_5, showing the orbital character of the V $3d$ and the O $2p$ bands. In the considered energy range, no magnesium states are present.

8.2. Optical properties

8.2.1. NaV_2O_5

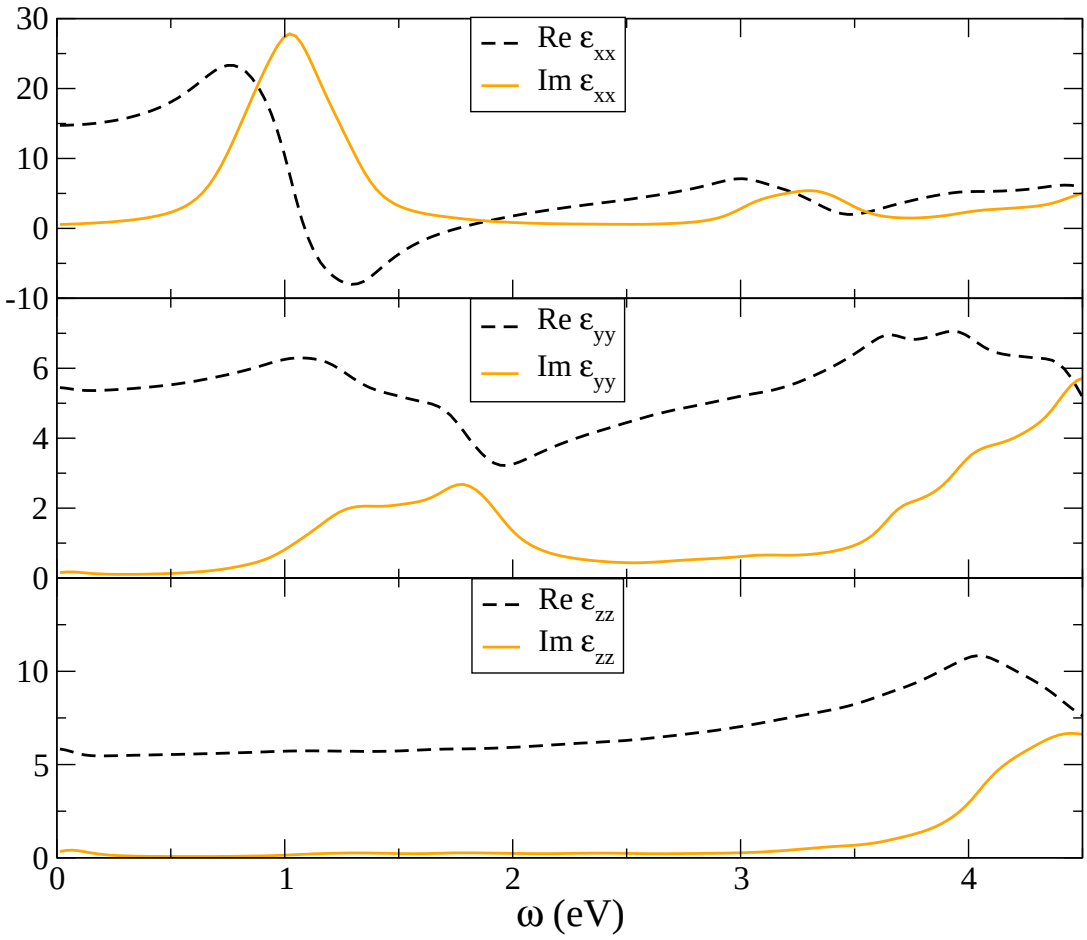

Figure 8.8.: Real and imaginary part of the dielectric function of NaV_2O_5 in xx, yy, and zz polarization, respectively.

Figure 8.8 shows the real and imaginary parts of the xx, yy, and zz components of the dielectric function of NaV_2O_5, respectively. The imaginary part of the dielectric function, ϵ_2, is related to the optical conductivity σ by the relation $\sigma_1 \propto \omega\epsilon_2$. Comparing the theoretical results with the measured xx and yy components of the optical conductivity presented in Refs. [41, 40, 90, 105, 43, 109] good agreement is found. This may surprise, since the gap at E_F can only be described taking into account correlation effects and is not present in the band structure presented in Section 8.1.1. On the other hand, the good agreement between theory and experiment shows that our calculations describe the electronic states very.

Literature consistently reports a peak in the xx components of σ_1 at about 0.9 eV, while the yy component shows a relatively weak peak above 1 eV and a more pronounced peak at about 1.75 eV. These features are well reproduced by theory. An analysis of the inter-band momentum matrix elements at different wave vectors k_y exhibits that the first peak in the xx response (at 1 eV) originates from transitions bonding and anti-bonding bands with V $3d_{xy}$ character. This is in agreement with the findings of Refs. [41, 43]. Thus, the peak reflects the hopping parameter within one rung of the V ladders, i.e. the peak positions corresponds approximately to $2t_{\parallel}$, with some deviation due to the dispersion of the respective bands.

The yy component (light polarized along the legs) is dominated by a double-peak structure at 1.27 eV and 1.78 eV, respectively. It is considerably weaker than the xx response. The analysis of the band structure reveals that the shoulder at 1.3 eV comes from in-rung transitions. These can contribute to $\varepsilon_{yy}(\omega)$ since at finite k_x values the in-rung states are neither odd nor even with respect to the $x \rightarrow -x$ transformation, and, therefore, can couple to light polarized along the y-axis.

In both polarizations, the peaks occurring at higher energies ($\omega > 3$ eV) originate from transitions between O-$2p$ and V orbitals. For example, the broad feature around 3 eV in the xx spectra arises from transitions between O1-$2p_z$ states at -3.3 eV and bonding V-d_{xy} states around E_F. This finding is in contrast to the interpretation of Ref. [41], where the peak at 3 eV is attributed to V $3d_{xy}$ $\rightarrow$ V $3d_{x^2-y^2}$ transitions.

In turn, in agreement with Ref. [41], we find that the small magnitude of the imaginary part of ϵ_{xx} (ϵ_{yy}) between 1.6 and 2.3 (2.6) eV can be related to the wide, but flat V $3d_{y^2}$ density of states in this energy region (see Fig. 8.3).

For E$\parallel c$, the imaginary part of the dielectric tensor hardly shows any signal up to 4 eV, which is consistent with a very weak interaction between different V–O layers in z direction.

8.2.2. CaV_2O_5

The dielectric function of CaV_2O_5 corresponding to $\vec{E} \parallel \vec{a}$ (ϵ_{xx}), $\vec{E} \parallel \vec{b}$ (ϵ_{yy}), and $\vec{E} \parallel \vec{c}$ (ϵ_{zz}) is presented in Fig. 8.9. The imaginary part of the calculated ϵ_{xx} shows a pronounced feature at low energies (0.6 eV), while ϵ_{yy} has a double peak structure below 1 eV. These findings are consistent with the measured optical conductivity of CaV_2O_5 presented in Ref.[105], where maxima are found at 1 eV (E $\parallel$ a) and at slightly higher energies for E $\parallel$ b. Accordingly, the theoretical peak at 1.5 eV can be related to the shoulder of the measured spectra at about 1.7 eV.

The character of the electronic transitions responsible for the peaks in the dielectric functions are, in general, the same as in NaV_2O_5. The low-energy peak of ϵ_{xx} corresponds to transition from the bonding to the anti-bonding V states

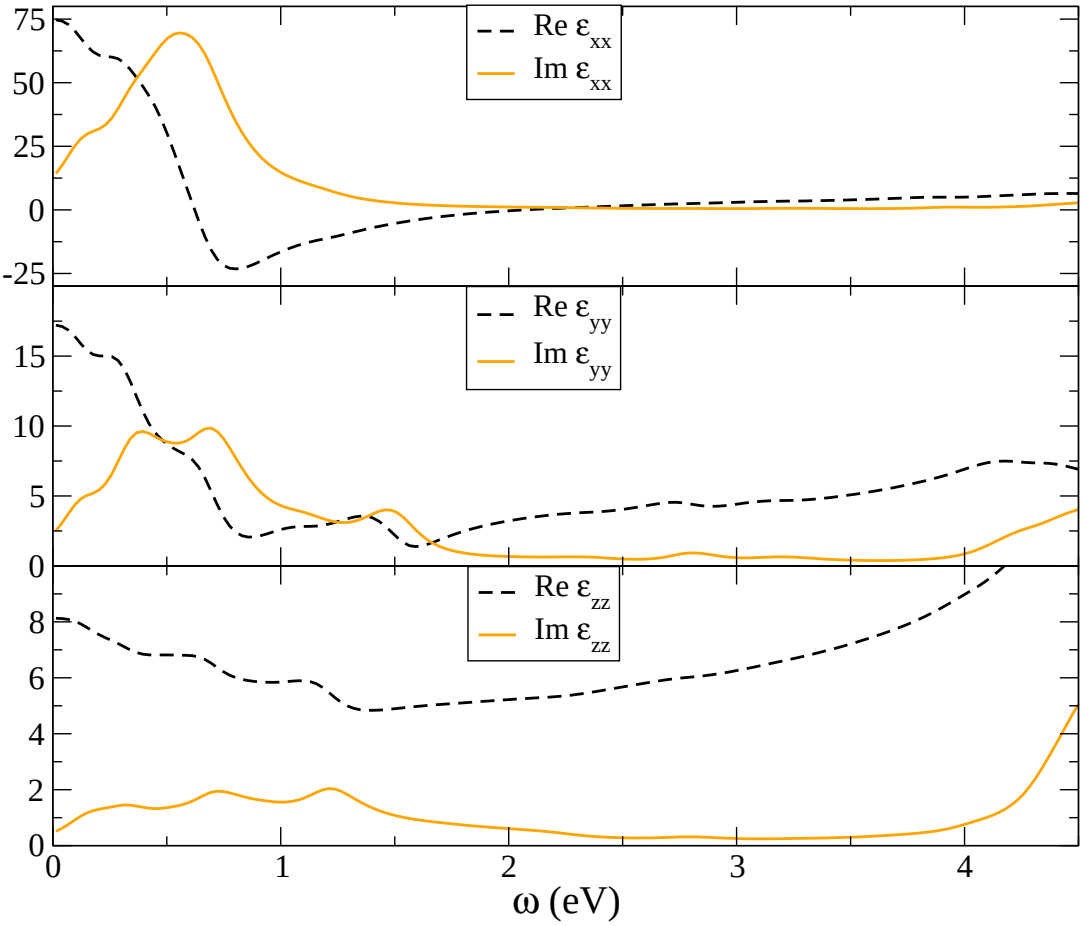

Figure 8.9.: Real and imaginary part of the dielectric function of CaV_2O_5 in xx, yy, and zz polarization, respectively.

with d_{xy} character, which is also described in Ref. [105]. On the other hand, the fact that Ca provides one more valence electron to the system compared to Na has two obvious effects: First, the optical response is stronger compared to NaV_2O_5. Second, the peak present in NaV_2O_5 around 3 eV is missing, since the bonding V-d_{xy} states are occupied and thus don't provide final states for the transitions. At the same time, since the in-ladder hopping matrix elements are smaller in CaV_2O_5 than in NaV_2O_5, the spectrum of unoccupied band states in CaV_2O_5 is denser, as can be seen in Figs 8.2 and 8.4, respectively. For this reason, the low-energy part of the dielectric function ($\omega < 1$ eV) of CaV_2O_5 shows a more complicated ω dependence than for NaV_2O_5 since more inter-band transitions are allowed at this spectral range.

Regarding the zz components of the dielectric function, some features are found around 1 eV, which are, however, very weak. Thus the situation appears to be comparable to the one in NaV_2O_5.

8.2.3. MgV_2O_5

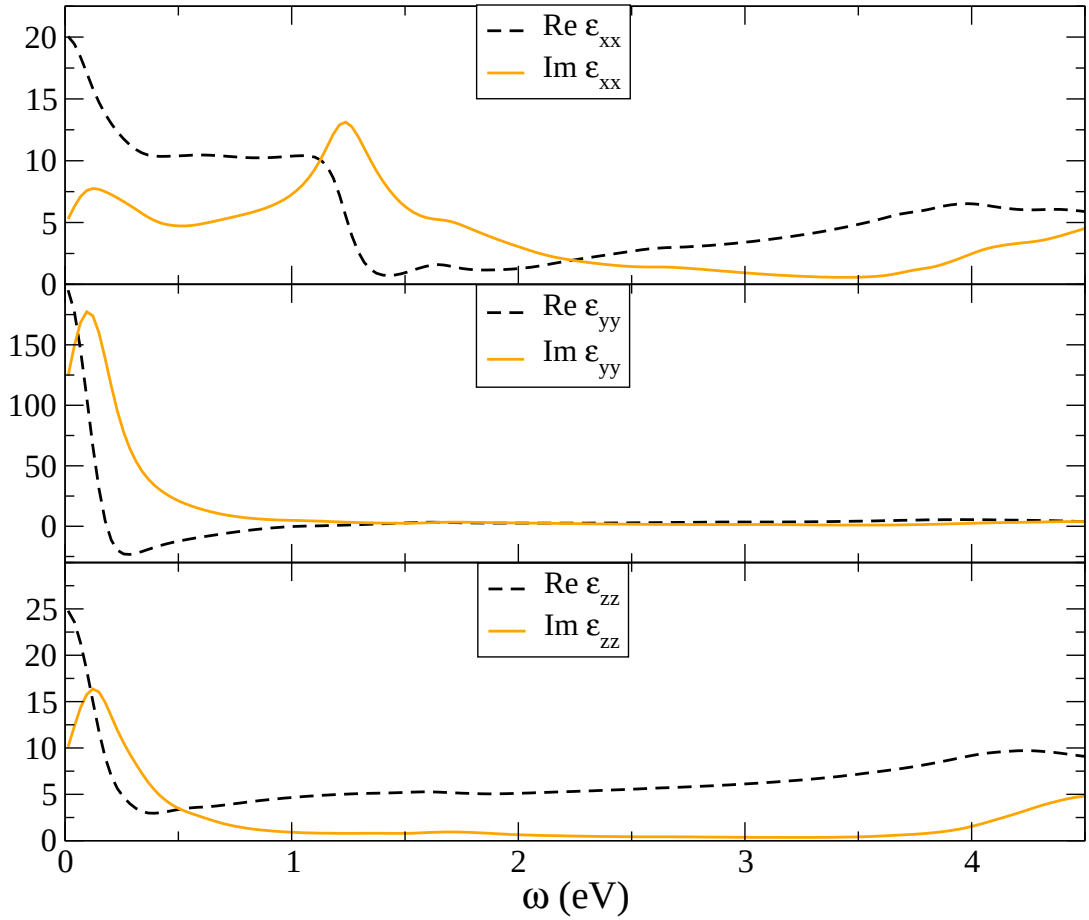

Figure 8.10.: Real and imaginary part of the dielectric function of MgV_2O_5 in xx, yy, and zz polarization, respectively.

The dielectric functions for the relaxed structure of MgV_2O_5 are presented in Fig. 8.10. Due to the fact that the gap between bonding and anti-bonding states in MgV_2O_5 disappears, large contributions to all three components at energies below 0.5 eV are found. Moreover, in Im ϵ_{xx} a pronounced feature at 1.25 eV and a weaker shoulder at 1.7 eV appears. While the former can be assigned to bonding → anti-bonding transitions around the Γ point, the latter corresponds to transition from the bonding V $3d_{xy}$ bands to V $3d_{xz}$ at about 1.2 eV (cf. Fig. 8.7).

Regarding ϵ_{yy}, the peak below 0.5 eV is strongly dominating.Yet, a shoulder at 1.1 eV and a peak at 1.7 can be detected. The shoulder at 1.1 eV can again be assigned to transitions from bonding to anti-bonding V d_{xy} states at the Γ point, and also the characterization of the 1.7 eV peak is analogous to the one found in ϵ_{xx}. With respect to the zz component, also in MgV_2O_5 no considerable contributions are present in the energy range between 0.5 eV and 3.5 eV.

9. Raman Spectra

9.1. NaV_2O_5

The theoretical Raman spectra of NaV_2O_5, calculated for a laser energy of 2.54 eV (488 nm), is presented in Figure 9.1. Regarding experimental results, various measurements are found in literature. In Refs. [91, 36, 92, 37, 90] polarized Raman spectra for the laser energy used in Fig. 9.1 are presented, while Refs. [7, 19, 16] report measurements at a laser frequency of 2.41 eV. For the results reported in Ref. [110], finally, six different lasers with frequencies between 1.64 eV (752.5 nm) and 2.71 eV (457.9 nm) were applied. The experimental spectra as presented in Ref. [37] are shown in Fig. 9.2.

For the A_g spectra with xx polarization, very good agreement of theory and experiment is found. As in the measured spectra, the peaks at 176 cm^{-1}, 308 cm^{-1}, 512 cm^{-1} and 996 cm^{-1} dominate the spectrum. Also the double peak structure of the 414 cm^{-1} and the 467 cm^{-1} modes agree very well with experiment, while the signals at 111 cm^{-1} and 232 cm^{-1} are found to be very weak.

A good consistency with experiment is also found with respect to the large intensity for the 308 cm^{-1} and the 99 cm^{-1} peak in yy polarization, while the features between 400 cm^{-1} and 512 cm^{-1} quantitatively differ from the measured ones. Regarding the 232 cm^{-1} peak, the relative height is greater than the one in xx polarization, but still smaller than the experimental one in Fig. 9.2.

The peak structure of the A_g modes appearing in zz polarization is very characteristic. While all peaks between 200 cm^{-1} and 600 cm^{-1} are virtually invisible, the V–O3 stretching mode at 996 cm^{-1} contributes with a very large intensity. The chain rotation mode at 111 cm^{-1} and the 176 cm^{-1} vibration, where Na oscillates parallel to c, show at least a small contribution. The intensity of the former is, however, much smaller than the experimentally measured one, which appears to be comparable to the one of the 996 cm^{-1} mode.

Comparing the calculated intensities obtained in the three parallel polarizations, the largest peak is related to the 996 cm^{-1} mode with incoming and outgoing light polarized in z direction, respectively. However, in average the largest intensities are found in xx polarization, which are almost one order of magnitude larger than the one in yy polarization.

The spectra corresponding to crossed polarization, i.e. the B_{1g} modes (xy), B_{2g} modes (xz) and the B_{3g} modes (yz), exhibit in general much weaker signals than the A_g modes. The xy and xz spectra show peak heights up to 0.005, while

the highest peak of the B_{3g} modes has an intensity of 0.015 $sr^{-1}cm^{-1}$. Comparing the theoretical B_{1g} modes with the experimental spectra taken from Ref. [37], a very strong resemblance is encountered. Experiment and theory consistently show that the B_{1g} modes highest and the lowest in frequency give the largest peak, while the O3–V–O2 bending mode at 253 cm^{-1} has a lower intensity.

Comparing the B_{2g} spectra (yz polarization) and the different measured results with each other it turns out, that the peak assignment is not unambiguous. As already discussed in detail in section 6.3.1, our calculated Raman spectra allow a re-interpretation of the actual B_{2g} mode frequencies. Thus we believe that the broad experimental feature at about 530 cm^{-1} (Refs. [90, 37, 36, 19, 92, 110]) does not originate from a B_{2g} mode, and instead we suggest that the peak found at about 685 cm^{-1} has B_{2g} symmetry. In terms of relative peak heights, we find in agreement with experiment a very strong intensity for the B_{2g} modes second lowest in energy and in addition considerable peak heights for the 206 cm^{-1} mode, the 360 cm^{-1} mode (e.g. Ref. [92]) and the 683 cm^{-1} mode. In turn, the large theoretical intensity of mode close to 300 cm^{-1} is not verified by experiment.

A new interpretation due to theory is also possible for the B_{3g} modes of NaV_2O_5. Accordingly, theory shows that also two smaller peaks located at 140 cm^{-1} and 176 cm^{-1}, respectively, in the yz polarized spectra of Ref. [37], are due to interactions with B_{2g} oscillations. As theory exhibits, these two modes contribute only with a weak intensity to the spectrum, but they can still be distinguished. Nevertheless, the modes at 262 cm^{-1}, 384 cm^{-1}, and 708 cm^{-1} clearly predominate. Sect. 6.4.1 contains a further discussion of the peak assignment in Refs. [90, 37, 36, 19, 92] in the light of the theoretically findings.

Fig. 9.3 shows the change of the dielectric function with respect to atomic displacements along the eigenvectors, $|d\epsilon_{ii}/dQ|^2$, at laser energies from 1.9 eV to 3.1 eV for the A_g modes of NaV_2O_5. The results for $|d\epsilon_{zz}/dQ|^2$ are only shown for the 996 cm^{-1} mode, since for all other modes it hardly contributes throughout the considered energy range. As it is explained in Sect. 4.4, large values of $|d\epsilon/dQ|^2$ at a certain laser energy imply resonances measuring with a respective laser. Thus, Fig. 9.3 indicates that the laser frequencies used in References [91, 36, 92, 37, 90, 7, 19, 16], i.e. 2.41 eV (514 cm) and 2.54 eV(488 nm), respectively, are located at energies where the system shows a rather weak response. Actually, for almost all modes and polarizations $|d\epsilon_{ii}/dQ|^2$ shows a minimum between 2.25 eV and 2.75 eV. In turn, for all modes $|d\epsilon_{xx}/dQ|^2$ shows a maximum around 3 eV, while $|d\epsilon_{yy}/dQ|^2$ gives the largest contributions at about 2 eV. The derivative of ϵ_{zz} with respect to Q for the 996 cm^{-1} mode, finally, is relatively linear in the range between 2.0 and 3.0 eV, but also has its largest contributions at laser frequencies of 3. eV.

These theoretical findings are in excellent agreement with the results presented in Ref. [110]. Even though it is not possible to compare the absolute intensities of spectra measured with different lasers, at least relative peak heights indicate trends in terms of resonances. In concordance with our findings, in xx polar-

ization the low-frequency phonons show the strongest resonances when the laser frequency is higher than 2.4 eV (514 nm). In contrast, the relative peak heights of the A_g modes of NaV_2O_5 are large for low laser energies (1.83 eV – 2.4 eV), while they decrease applying a laser frequency higher than 2.5 eV.

9.2. CaV_2O_5

The theoretically calculated Raman spectra of CaV_2O_5 for A_g modes (xx, yy, and zz polarization), B_{1g} modes (xy polarization), B_{2g} modes (xz polarization), and B_{3g} modes (yz polarization) are shown in Fig. 9.4. Concerning the A_g modes, as in NaV_2O_5 the V–O3 stretching mode strongly dominates the xx polarized spectra. Nevertheless, the absolute peak height is by a factor of two smaller than in the sodium compound. In yy polarization, peaks for all eight A_g modes can be distinguished. Among these, the eigenmodes between 200 cm^{-1} and 310 cm^{-1} together with the V–O2 stretching mode at 516 cm^{-1} yield the largest intensities. The peak height of the 446 cm^{-1} mode is already much smaller, and the 106 cm^{-1}, the 412 cm^{-1}, and the 900 cm^{-1} modes exhibit an even weaker intensity. With regard to the small contribution of the V–O3 vibration at 900 cm^{-1}, calcium vanadate actually differs from sodium vanadate, where the respective peak is much higher.

The latter mode is also virtually absent in xx polarized spectra. While the 446 cm^{-1} and the 516 cm^{-1} mode show maximum intensities of about 0.1 $sr^{-1}cm^{-1}$, the peak height of the V–O3 stretching mode is more than one order of magnitude smaller. The same is true for the Ca $\parallel$ c oscillation at 201 cm^{-1} and the $O1_z$+O3–V–O2 bending mode at 412 cm^{-1}. The chain rotation mode at 106 cm^{-1} and the the O3–V–O2 bending modes at 265 cm^{-1} and 307 cm^{-1}, respectively, have a much smaller intensity than the strongest eigenmodes, but still contribute noticeable to the xx spectra.

On the experimental side, up to now to the best of our knowledge no polarized measurements with CaV_2O_5 single crystals exist. As discussed in detail in section 6.1.2, Ref. [93] presents measurements in different polarizations, but the sample was polycrystalline. This implies that the orientation of the polarization with respect to the crystal axes is not known, which in consequence also leads to admixtures of contributions of non-diagonal terms in parallel polarization and vice versa. In turn, the other two available measurements (Refs. [94, 39]) are unpolarized, and the peak assignment was only done by relating the peaks to the ones of polarized NaV_2O_5 spectra closest in energy.

In order to facilitate the interpretation of the experimental spectra in the light of theory, unpolarized spectra—obtained from a superposition of the calculated polarized spectra–are presented in Fig. 9.5, while Fig. 9.6 shows the experimental results from Ref. [39]. Comparing the to figures it turns out, that the measured peak at 138 cm^{-1} is apparently due to a B_{1g} and a B_{2g} mode, both situated

at 135 cm^{-1}, while the A_g mode second highest in energy is shifted to much higher frequencies (201 cm^{-1}) compared to NaV_2O_5. In an analogous way, also the peaks at 280 cm^{-1} and 334 cm^{-1}, interpreted as B_{3g} and B_{2g} peaks in the reference, respectively, can be identified as originating from an A_g mode. Further detailed discussions of the mode assignment for CaV_2O_5, comparing theory and the measurements from literature, are presented in the corresponding sections of Chap. 6.

In Fig. 9.7, the resonance behavior of the A_g modes of CaV_2O_5 with respect to the laser frequency is presented. As already explained in the context of the NaV_2O_5 spectra, large values for $|d\epsilon_{ii}/dQ|^2$ imply a strong response of the system to a laser with the corresponding energy. As in NaV_2O_5, the change of ϵ_{zz} with respect to phonon distortions is considerable only for the V–O3 stretching mode with 900 cm^{-1}, where this component is even dominating. In all other modes, $|d\epsilon_{zz}/dQ|^2$ hardly contributes and is therefore not included in the respective plots. In the 900 cm^{-1} mode, moreover, the resonance behavior is similar to the one in NaV_2O_5, i.e. $|d\epsilon_{zz}/dQ|^2$ increases rather linearly with increasing laser energy.

Concerning $|d\epsilon_{xx}/dQ|^2$, in the calcium compound most of the eigenmodes show the strongest resonances for low laser energies, i.e. $\omega_L = 2$ eV, in contrast to the situation in NaV_2O_5. Only for the 307 cm^{-1} mode the behavior is opposite, and higher laser energies lead to a stronger Raman intensity. The situation for the yy component is more complex than in NaV_2O_5. While in the latter $|d\epsilon_{yy}/dQ|^2$ shows a rather clear trend of resonances for low laser energies, in the calcium structure strong resonances of all eigenmodes can be distinguished at about 2.75 eV. Moreover, the eigenmodes with 307 cm^{-1}, 265 cm^{-1}, 412 cm^{-1} and 516 cm^{-1} show less pronounced maxima of $|d\epsilon_{yy}/dQ|^2$ somewhat below or above 2.75 eV.

9.3. MgV_2O_5

The calculated Raman spectra for the A_g modes of MgV_2O_5 at a laser energy of 2.41 eV (514 nm) are presented in Fig. 9.8, while unpolarized measurements for the same laser frequency (Ref. [39]) are shown in Fig. 9.9. Another time, in the theoretical Raman spectra with zz polarization the eigenmode highest in frequency predominates strongly, even though also the other eigenmodes can, at least, be distinguished. In yy polarization the 310 cm^{-1} mode, representing a Mg_z+O1–V–O3 bending, shows the largest intensity, followed by the chain rotation mode at 104 cm^{-1}, the leg↔leg oscillation at 546 cm^{-1}, and a second bending mode at 250 cm^{-1}. However, also the modes at 353 cm^{-1}, 395 cm^{-1}, and 419 cm^{-1} contribute considerably. On the other hand, the V–O3 stretching mode at 1018 cm^{-1} is not present in this polarization, which is similar to the situation in CaV_2O_5, but in contrast to NaV_2O_5.

The xx polarized Raman spectra appear to be rather balanced in terms of

the individual peak heights, i.e. all eight A_g modes can clearly be distinguished. Only the 546 cm^{-1} mode gives a rather weak contribution, while the intensities of the 104 cm^{-1} mode, the 1019 cm^{-1} vibration and the modes between 350 cm^{-1} and 450 cm^{-1} are very similar. Only the two Mg_z+O–V–O bending modes at 250 cm^{-1} and 310 cm^{-1}, respectively, stick out of the rest.

On the experimental side, to the best of our knowledge only measurements with unpolarized laser light exist, i.e. the ones presented in Ref. [93] and Ref. [39]. In both of them, the Raman spectra were obtained using an Ar^+ laser with an energy of 2.41 eV (514 nm), which corresponds to the laser frequency of the theoretical spectra. While in Ref. [93] no symmetry is assigned to the peaks, the assignment in Ref. [39] is again done by relating each MgV_2O_5 peak to the polarized NaV_2O_5 peak closest in frequency. Thus, theory one more time allows an improvement in the interpretation of the experimental spectra. In this context, theory indicates that the measured peaks at 220 cm^{-1}, 278 cm^{-1}, 315 cm^{-1}, and 374 cm^{-1} are due to A_g phonon modes, while the weak peaks at 233 cm^{-1} and 478 cm^{-1} are likely to originate from oscillations with other symmetries. The assignment of the peaks located at 1002 cm^{-1}, 536 cm^{-1}, 414 cm^{-1}, and 98 cm^{-1} is again consistent with our findings.

The derivative of the dielectric function with respect to phonon distortions corresponding to A_g eigenmodes, $|d\epsilon_{ii}/dQ|^2$, is presented in Fig. 9.10. As it is the case for NaV_2O_5 and CaV_2O_5, also in MgV_2O_5 ϵ_{zz} is considerably affected only by the V–O3 stretching mode at about 1000 cm^{-1}, and is therefore omitted in the other plots. Moreover, also the linear increase of $|d\epsilon_{zz}/dQ|^2$ with the laser energy, encountered as well in the other two vanadates, is found in MgV_2O_5.

The xx component of the Raman spectra in general tends to exhibit resonance at low laser energies, i.e. $\omega_L < 2.25$ eV. Nevertheless, the 419 cm^{-1} mode deviates from this tendency, having large values of $|d\epsilon_{xx}/dQ|^2$ for the whole energy range from 2.2 eV to 2.8 eV. Moreover, the bending modes at 250 cm^{-1} and 353 cm^{-1} show a second resonance at a laser energy of about 2.6 eV, which is even more pronounced in the leg↔leg oscillation with 546 cm^{-1}.

The yy component, finally, responds rather weakly to laser energies in the considered range, i.e. the maxima of $|d\epsilon_{xx}/dQ|^2$ are by a factor of five smaller than the ones in xx polarization. Moreover, a general trend for all A_g modes can hardly be identified. While the eigenmodes with 353 cm^{-1}, 419 cm^{-1}, and 546 cm^{-1} show resonances at energies greater than 2.75 eV, the largest values of $|d\epsilon_{yy}/dQ|^2$ in the 104 cm^{-1}, the 310 cm^{-1}, and the 1019 cm^{-1} vibrations are found at low laser frequencies, respectively, while the modes with 250 cm^{-1} and 395 cm^{-1} do not significantly alter ϵ_{yy} in the whole energy range between 2 eV and 3 eV. In the 546 cm^{-1} oscillation, one more noticeable feature is present, namely a broad maximum of $|d\epsilon_{yy}/dQ|^2$ centered at a laser energy of about 2.55 eV, with a shoulder at 2.3 eV.

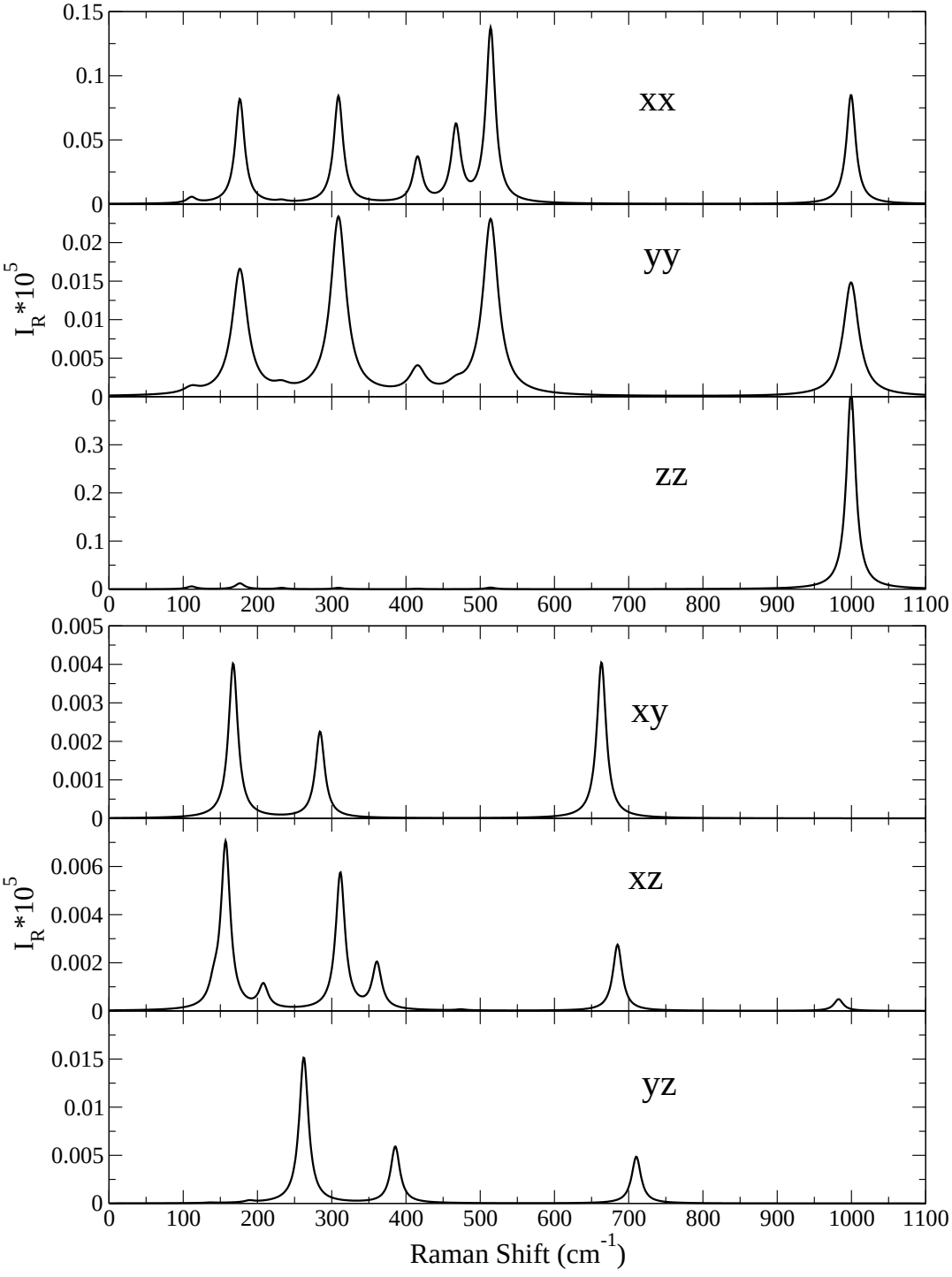

Figure 9.1.: Theoretical Raman spectra (sr^{-1} cm^{-1}) of the A_g modes (upper panel) and B_{ng} modes (lower panel) of NaV_2O_5. The spectra are calculated for a laser frequency of 2.54 eV (514 nm).

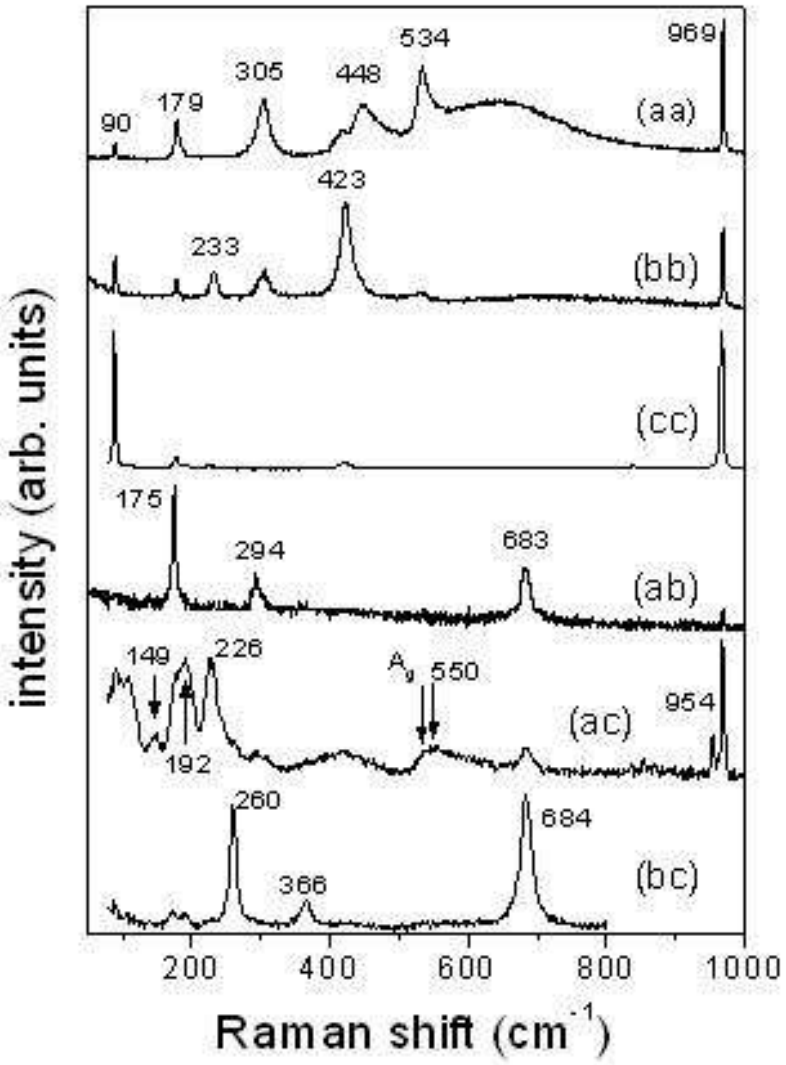

Figure 9.2.: Experimental Raman spectra of NaV_2O_5, measured with polarized laser light, as presented in Ref. [37]. The laser frequency is 2.54 eV (488 nm) .

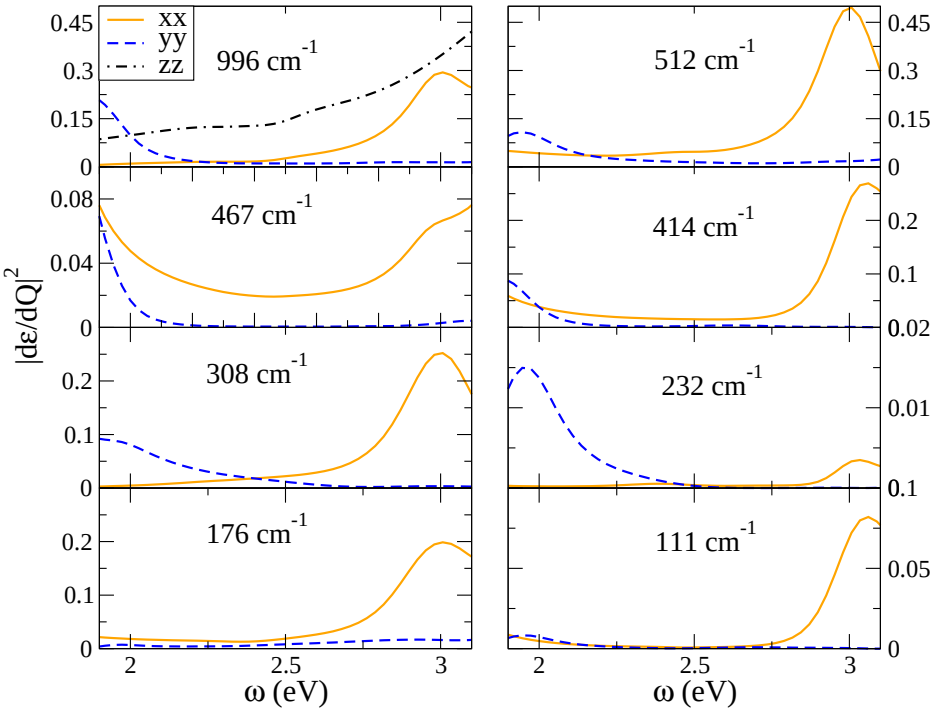

Figure 9.3.: Change of the dielectric function with respect to displacements along the eigenvectors, $|d\epsilon/dQ|^2$, for the A_g eigenmodes of NaV_2O_5.

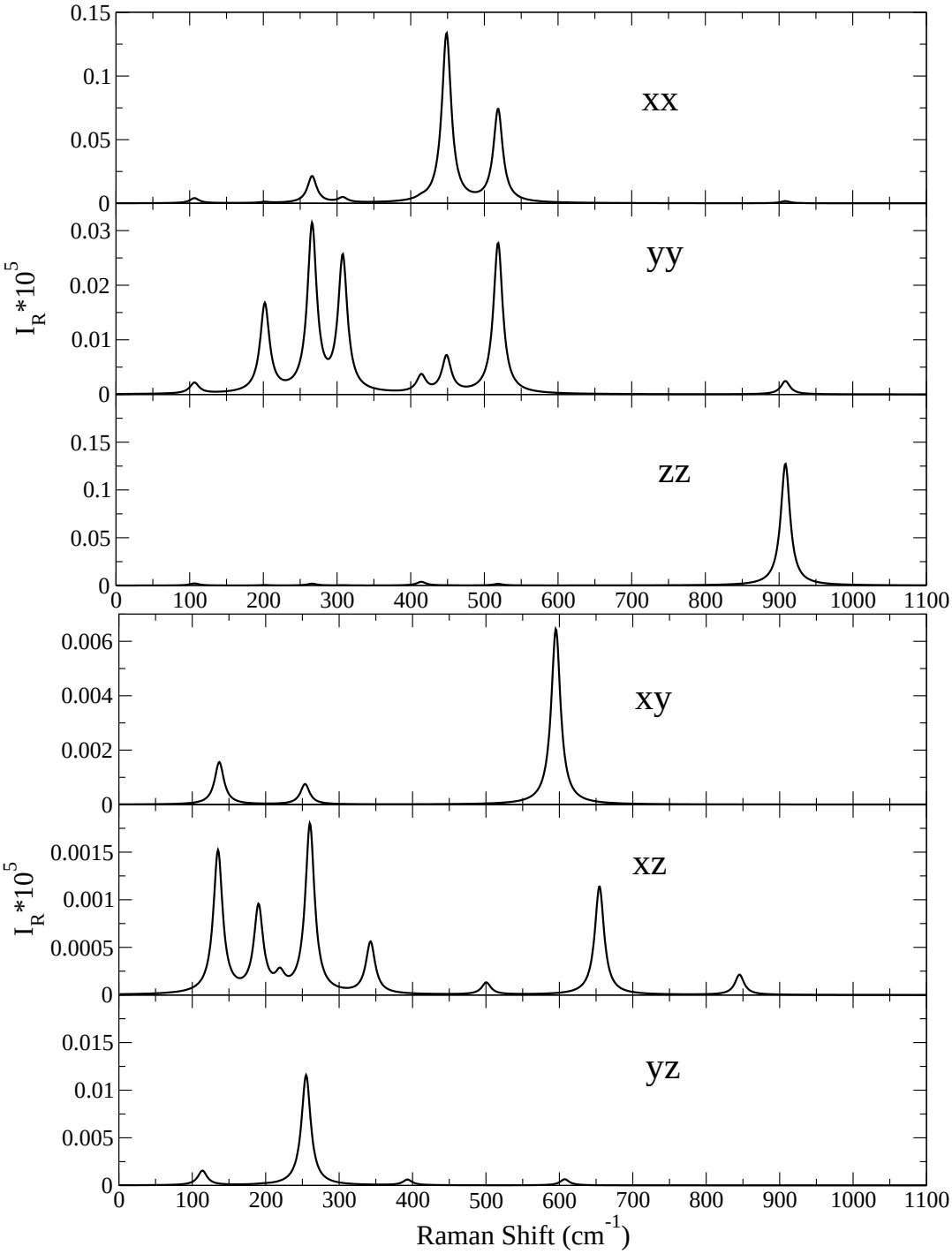

Figure 9.4.: Theoretical Raman spectra (sr^{-1} cm^{-1}) of the A_g modes (upper panel) and B_{ng} modes (lower panel) of CaV_2O_5. The spectra are calculated for a laser frequency of 2.41 eV (514 nm).

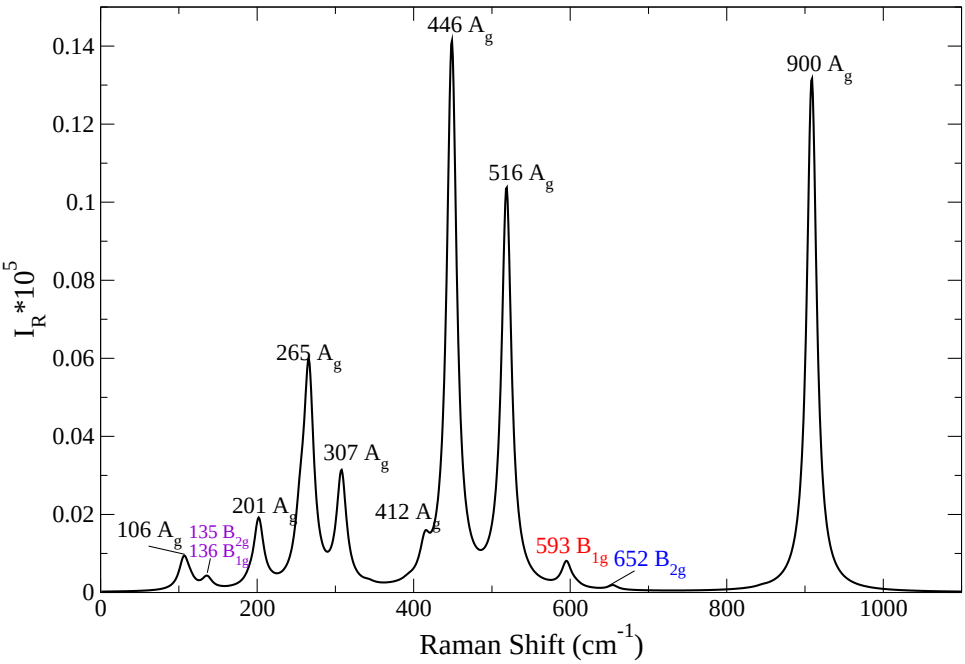

Figure 9.5.: Theoretical Raman spectra (sr^{-1} cm^{-1}) of CaV_2O_5: Superposition of all A_g and B_{ng} spectra. (Laser frequency: 2.41 eV = 514 nm).

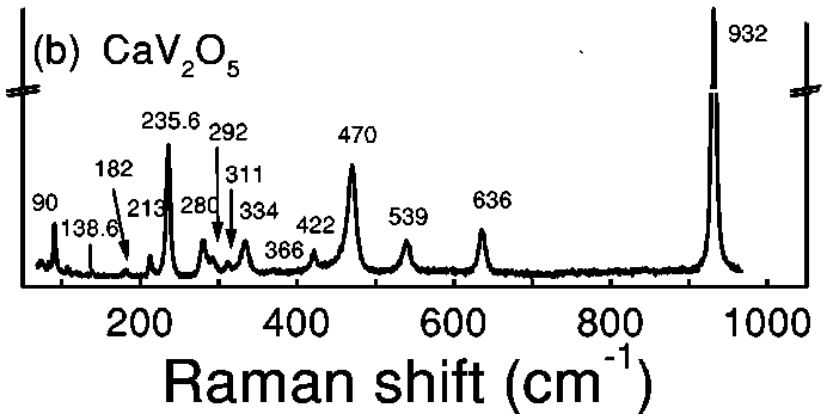

Figure 9.6.: Unpolarized experimental Raman spectra of CaV_2O_5 as presented in Ref. [39]. The laser frequency is 2.41 eV (514 nm) .

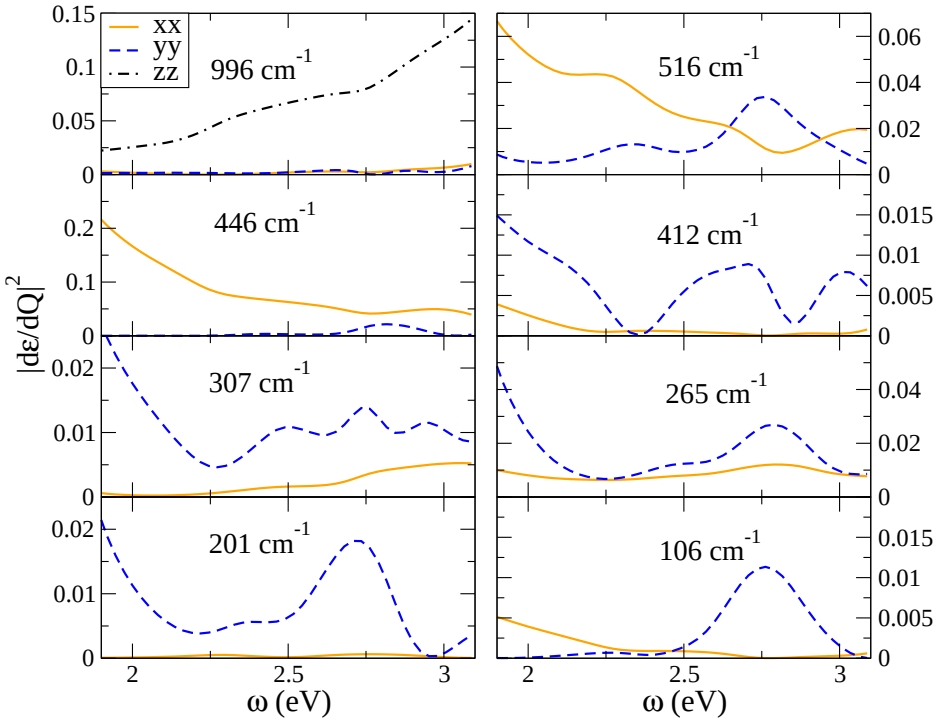

Figure 9.7.: Change of the dielectric function with respect to displacements along the eigenmodes, $|d\epsilon/dQ|^2$, for the A_g eigenvectors of CaV_2O_5.

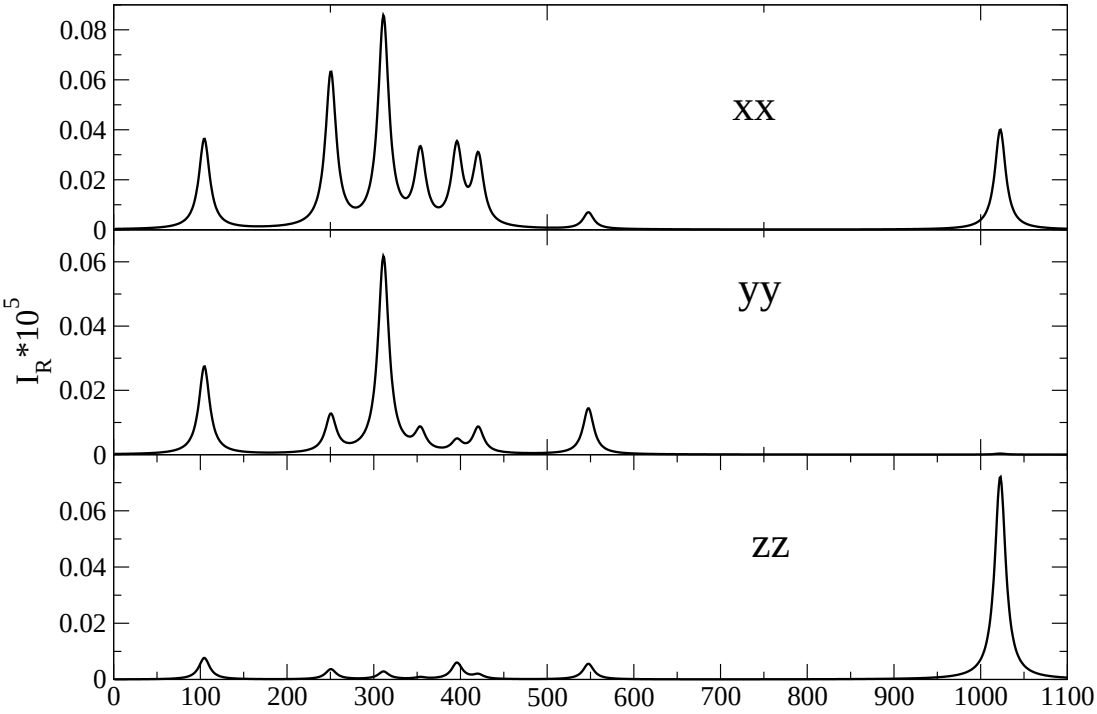

Figure 9.8.: Theoretical Raman spectra (sr^{-1} cm^{-1}) of the A_g modes of MgV_2O_5 for xx, yy, and zz polarization. The spectra are calculated for a laser frequency of 2.41 eV (488 nm).

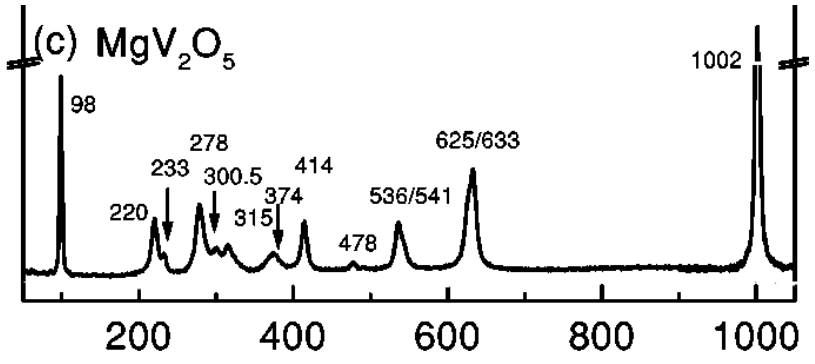

Figure 9.9.: Unpolarized experimental Raman spectra of MgV_2O_5 as presented in Ref. [39]. The laser frequency is 2.41 eV (514 nm) .

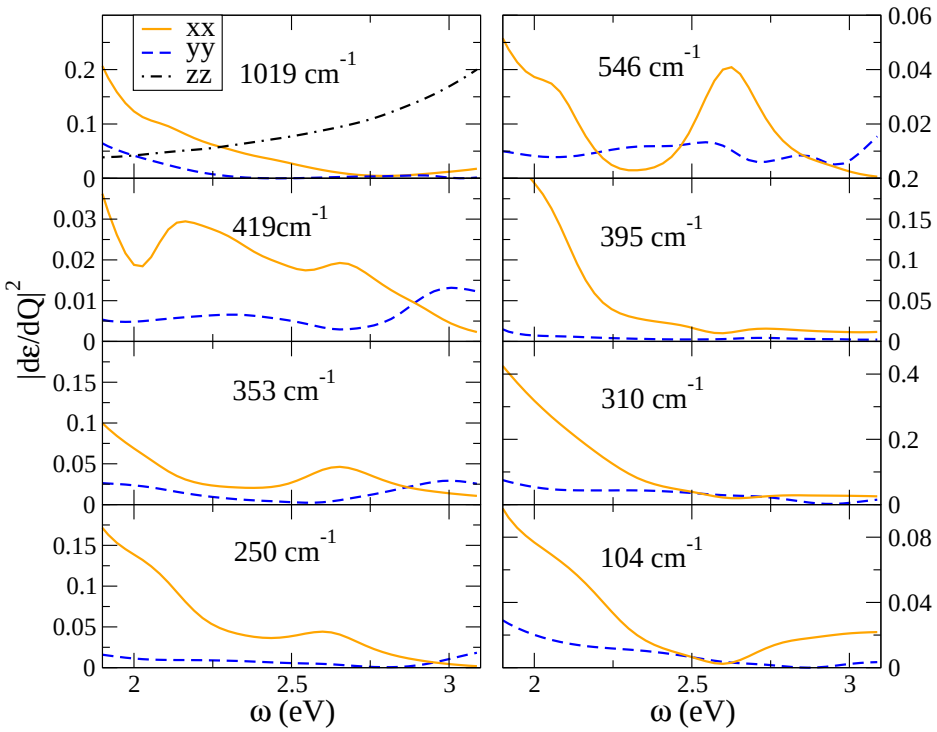

Figure 9.10.: Change of the dielectric function with respect to displacements along the eigenvectors, $|d\epsilon/dQ|^2$, for the A_g eigenmodes of MgV_2O_5.

10. Electron-Phonon and Spin-Phonon Coupling

This chapter is organized as follows: The results for the two iso-structural vanadates NaV_2O_5 and CaV_2O_5 are presented in two separate sections. For each section, in a first subsection the theoretical results for the hopping parameters $t_\parallel$, $t_\perp$, and t_i, the charge transfer gap E_g, and the on-site Coulomb repulsion U of the undistorted structures are presented and compared to literature. In the second part of each section, the calculated parameters of electron-phonon and spin-phonon parameters are discussed.

10.1. NaV_2O_5

10.1.1. Hopping parameters, charge transfer gap, Hubbard U

	Theory	References							
		[32]	[106]	[111]	[100]	[11]	[40]	[112]	[97]
$\lvert t_\parallel \rvert$	0.175	0.17	0.15	0.1158–0.1765	0.085	0.049	0.2	0.140	0.17
$\lvert t_\perp \rvert$	0.387	0.38	0.35	0.4206–0.5427	–	0.172	0.3	0.298	0.38
$\lvert t_i \rvert$	0.117	0.012	0.3	0.0287–0.0442	0.085	0.062	–	0.05	0.012
E_g	2.565	0.71	–	–	–	–	1	–	–
U	2.45	2.8	–	6.8	4.1	–	–	–	–

Table 10.1.: Hopping matrix elements, charge transfer gap and on-site Hubbard repulsion U (in eV) extracted from the ab initio band structure of NaV_2O_5 compared to literature.

The calculating hopping matrix elements, the charge transfer gap, and the on-site Coulomb interaction compared with results from literature are presented in Tab. 10.1. Refs. [6] and [31] obtain exchange integrals along the leg by fitting the high T part of the measured magnetic susceptibility to a spin 1/2 chain. The obtained values of 0.024 and 0.046 eV, respectively, differ by a factor of two from each other, and are much larger than the theoretically obtained parameter of 0.009 eV.

The results in Ref. [32] are obtained by a mapping of a LAPW band structure to a tight binding model, while Refs. [100] and [97] are based on Linearized Muffin-Tin-Orbital (LMTO) calculations. Reference [32] reports $|t_{\parallel}| = 0.17$ eV and $|t_{\perp}| = 0.38$ eV, which excellently agree with our findings. In contrast, the inter-ladder hopping probability of $t_i = 0.012$ eV of the same reference, which is the same as the one presented in Ref. [97], differ by one order of magnitude from our value ($t_i = 0.117$ eV). Ref. [100] presents hopping matrix elements of 0.085 eV for both, $t_{\parallel}$ and $t_{\perp}$. The charge transfer gap E_g is computed in a different way compared to our procedure: Instead of extracting it directly from the band structure, it is calculated from $t_{\perp}$ and $J_{\perp}$, $E_g = 2t_{\perp} - J_{\perp}$, yielding $E_g = 0.71$ eV, which is by about a factor of four lower than our E_g (2.565 eV).

Ref. [106] uses band energies from a LMTO calculation to estimate the hopping probabilities by means of a semi-empirical law presented in Ref. [113]. The agreement with our findings is very good for $t_{\parallel}$ (0.15 eV) and $t_{\perp}$ (0.35 eV), but is much higher for t_i (0.3 eV).

In Ref. [111] hopping and magnetic exchange integrals for a nearest neighbor t-J model are obtained by ab-initio calculations of embedded crystal fragments by means of three different methods: First, using a so-called "iterative difference dedicated configuration interaction level 1 method" (IDDCI1), which accounts for dynamical polarization, second, diagonalizing the complete active space defined on the set of orbitals optimized within the IDDCI1 procedure (CASCI), and finally by means of a "difference dedicated configuration interaction level 2" (DDCI2) method, which in addition includes correlation effects. For $t_{\parallel}$, the results are between 0.116 eV (CASCI) and 0.177 eV(IDDCI1), which is in good agreement with our results. The values for $t_{\perp}$, in turn, which lie between 0.421 eV (CASCI) and 0.5427 eV (IDDCI1) are somewhat increased with respect to our findings. The reported values for t_i differ considerably comparing the different methods: CASCI gives 0.038 eV, while IDDCI1 leads to an 25% lower value of 0.29 eV, and the DDCI2 result is almost twice as large (0.044 eV). However, all results are below the t_i we find.

Ref. [11] determines the hopping probabilities by a Slater-Koster type of treatment as presented in Refs. [114, 113]. The calculated results for the hopping matrix elements are all much smaller than ours, namely $t_{\parallel} = 0.049$ eV, $t_{\perp} = 0.172$ eV, $t_i = 0.062$ eV.

The results presented in Ref. [40] are based on the analysis of optical absorption measurements in terms of a model Hamiltonian. This model Hamiltonian includes in a first step only one rung, where hoppings, charge displacements within the rung, and on-site Hubbard repulsion are considered, and in a second step two rungs of one ladder, in order to account for hoppings and spin exchange along the ladder. Moreover, the charge transfer gap is obtained as the splitting between the bonding and anti-bonding eigenstate of a system with one electron per rung. The resulting hopping parameters $t_{\perp}$ and $t_{\parallel}$ of 0.2 and 0.3 eV, respectively, are in good agreement with our findings. In turn, the charge transfer gap of $E_g =$

1 eV deviates considerably from ours, which may be attributed to the different derivations.

In addition to hopping and exchange matrix elements, the on-site Hubbard repulsion U is calculated by two different ways as explained in Sect. 5.4. When putting the positive charge on the Na sites, the resulting U for NaV_2O_5 of 2.8 eV (averaged over the Brillouin zone (BZ)) is in good agreement with Ref. [32], where the same method is used. We preferred, however, to provide the positive charge in terms of a uniform background, which leads to a U value of 2.45 eV. Compared to our result for the on-site Hubbard repulsion, the U value of 6.0 eV reported in Ref. [111] is considerably higher. In this reference, U was calculated as $U_d = 4(t_\parallel)^2/(2K_\parallel - J \parallel)$, where $K_\parallel$ is the direct exchange integral along the ladder and has a value of 0.002 eV. On the other hand, Ref. [100] presents an intermediate value of 4.1 eV, resulting from a supercell calculation as proposed in Ref. [115].

10.1.2. Coupling parameters

The parameters of electron-phonon and spin-phonon coupling for the Raman and infrared active phonon modes of NaV_2O_5 are presented in Tables 10.2 and 10.3, respectively.

The hopping parameter along the ladder, $t_\parallel$, is most affected by changes of the V–O2 distance due to displacements of the respective atoms. Accordingly, the greatest values for $\delta t_\parallel/\delta Q$ are found for the V–O2 stretching modes with B_{1g} symmetry at 661 cm^{-1} ($\delta t_\parallel/\delta Q = 0.042$ eV) and A_g symmetry at 512 cm^{-1} ($\delta t_\parallel/\delta Q = 0.021$ eV), respectively. These modes are followed by an antisymmetric V–O2 stretching mode, i.e. the B_{1u} mode with 554 cm^{-1}, where a corresponding parameter of 0.016 eV is obtained.

The A_g mode at 512 cm^{-1} is also important with respect to changes in the hopping perpendicular to the ladder: It shows the largest corresponding electron-phonon coupling of all modes, namely $\delta t_\perp/\delta Q = 0.021$ eV. In contrast, the second highest value of $\delta t_\perp/\delta Q$, i.e. 0.016 eV, is encountered for the A_g mode at 308 cm^{-1}, which does not influence $t_\parallel$ at all. Strong electron-phonon coupling with regard to in-rung hoppings is also found for the A_g V–O1–V bending mode with 467 cm^{-1} ($\delta t_\perp/\delta Q = 0.011$ eV), the V–O2 stretching mode with B_{1g} symmetry at 661 cm^{-1} ($\delta t_\perp/\delta Q = 0.010$ eV), which was also responsible for the largest $\delta t_\parallel/\delta Q$, and the highest energy A_g mode at 996 cm^{-1} ($\delta t_\perp/\delta Q = 0.010$ eV). The latter two phonon modes indicate that $\delta t_\perp/\delta Q$ is not only determined by changes with respect to the rung, but also by shifts of the neighboring atoms of V, such as the apex oxygen O3, and the in-leg oxygen O2.

A different scenario is found for the inter-ladder hopping parameter t_i. Comparing its change with respect to distortions along the eigenvectors of different phonon modes, it turns out that $\delta t_i/\delta Q$ is by far largest for the B_{1g} mode at 167 cm^{-1}, with a result of 0.069 eV. In fact, in this eigenmode the adjacent legs

Irrep	ω	Assignment	$\frac{\delta t_\parallel}{\delta Q}$	$\frac{\delta t_\perp}{\delta Q}$	$\frac{\delta t_i}{\delta Q}$	$\frac{\delta E_g}{\delta Q}$	$\frac{\delta J_\parallel/J_\parallel}{\delta Q}$	$\frac{\delta J_\perp/J_\perp}{\delta Q}$
A_g	996	V-O3 stretching	0.0021	0.0098	0.0053	0.0924	0.0187	0.0443
	512	V-O2 stretching	0.0209	0.0212	0.0440	0.0900	0.2935	0.0768
	467	V-O1-V bending	0.0016	0.0114	0.0106	0.0037	0.0052	0.0478
	414	$O1_z$ + O3-V-O2 b.	0.0110	0.0069	0.0142	0.0010	0.1277	0.0292
	308	O3-V-O2 bending	0.0000	0.0162	0.0251	0.0540	0.0003	0.0942
	232	O3-V-O2 bending	0.0012	0.0012	0.0277	0.0334	0.0083	0.0013
	176	Na ∥ c	0.0018	0.0060	0.0207	0.0181	0.0128	0.0221
	111	chain rot.	0.0007	0.0023	0.0137	0.0096	0.0045	0.0088
B_{1g}	661	V-O2 stretching	0.0421	0.0099	0.0002	0.0022	0.5259	0.0322
	283	O3-V-O2 bending	0.0007	0.0009	0.0019	0.0050	0.0154	0.0279
	167	antipar. leg-shift	0.0032	0.0059	0.0693	0.0043	0.0196	0.0129
B_{2g}	979	V-O3 stretch.	0.0010	0.0008	0.0089	0.0123	0.0143	0.0010
	683	V-O1 stretch.	0.0006	0.0010	0.0037	0.0044	0.0087	0.0038
	472	O2-V-O1 bend.	0.0006	0.0005	0.0002	0.0031	0.0058	0.0033
	360	O2-V-O3 bend.	0.0001	0.0012	0.006	0.0084	0.0026	0.0072
	286	O2-V-O3 bend.	0.0022	0.0015	0.0022	0.0052	0.0233	0.0094
	206	Na-ladder shear	0.0009	0.0002	0.0085	0.0025	0.0117	0.0002
	157	Na ∥ a + chain rot.	0.0002	0.0033	0.0064	0.0054	0.0006	0.0153
	141	chain rotation	0.0010	0.0024	0.0051	0.0048	0.0122	0.0117
B_{3g}	708	V-O2 stretching	0.0045	0.0001	0.0008	0.0002	0.0433	0.0096
	384	O1-V-O3 bending	0.0086	0.0074	0.0006	0.0095	0.0939	0.0295
	262	rung *vs* O3 shear	0.0124	0.0004	0.0008	0.0056	0.1524	0.0044
	188	(ladder *vs* Na) ∥ b	0.0075	0.0008	0.0019	0.0001	0.0898	0.0008
	136	antipar. ladder shift	0.0067	0.0003	0.0014	0.0011	0.0813	0.0013

Table 10.2.: Parameters of electron-phonon (eV) and spin-phonon coupling for the Raman active phonon modes of NaV_2O_5 (frequency ω in cm^{-1}) as obtained from theory.

of neighboring ladders are shifted antisymmetrically with respect to each other, which explains its strong influence on the inter-ladder hopping. Other modes with large values for $\delta t_i/\delta Q$ are again the A_g V–O2 stretching with 512 cm^{-1} (0.044 eV), as well as the A_g modes at 232 cm^{-1} (0.028 eV) and 308 cm^{-1} (0.025 eV), which both comprise a O3–V–O2 bending. A considerable electron-phonon coupling regarding inter-ladder hoppings is also found in the A_g mode at 176 cm^{-1}, where Na oscillates against the the V–O ladders.

The change in the charge transfer gap, E_g, for the Γ point phonons of NaV_2O_5 represents the next parameter shown in Tables 10.2 and 10.3. Apparently, the shifts of E_g caused by phonon distortions are noticeably larger than the ones of the

Irrep	ω	Assignment	$\frac{\delta t_\parallel}{\delta Q}$	$\frac{\delta t_\perp}{\delta Q}$	$\frac{\delta t_i}{\delta Q}$	$\frac{\delta E_g}{\delta Q}$	$\frac{\delta J_\parallel/J_\parallel}{\delta Q}$	$\frac{\delta J_\perp/J_\perp}{\delta Q}$
B_{1u}	971	V-O3 stretch.	0.0008	0.0015	0.0005	0.0013	0.0000	0.0114
	554	V-O2 stretch.	0.0160	0.0008	0.0010	0.0006	0.1468	0.0489
	478	O1-V-O2 bend.	0.0090	0.0001	0.0004	0.0003	0.1012	0.0036
	352	O1-V-O2 b. + $O3_x$	0.0046	0.0001	0.0004	0.0017	0.0421	0.0122
	292	rung stretching	0.0013	0.0001	0.0010	0.0003	0.0133	0.0022
	190	O1-V-O3 b. + Na ∥ c	0.0023	0.0002	0.0001	0.0062	0.0240	0.0021
	154	Na ∥ c	0.0012	0.0002	0.0000	0.0013	0.0077	0.005
B_{2u}	562	V-O2 stretching	0.0000	0.0001	0.0018	0.0082	0.0009	0.0012
	386	O1-V-O3 bending	0.0004	0.0052	0.0002	0.0042	0.0028	0.0259
	231	O3 *vs* ladder shear	0.0003	0.0003	0.0000	0.0051	0.0025	0.0007
	174	Na ∥ b	0.0000	0.0001	0.0000	0.0007	0.0003	0.0004
B_{3u}	944	V-O3 stretching	0.0010	0.0014	0.0003	0.0025	0.0093	0.0050
	675	O1 ∥ a	0.0000	0.0007	0.0006	0.0010	0.0006	0.0027
	445	O2-V-O1 bend. ∥ a	0.0016	0.0002	0.0016	0.0037	0.0214	0.0038
	409	V-O2 bend. ∥ c	0.0008	0.0004	0.0019	0.0022	0.0089	0.0012
	255	V-O3 bending	0.0005	0.0007	0.0002	0.0083	0.0041	0.0021
	145	Na ∥ a	0.0000	0.0001	0.0002	0.0004	0.0001	0.0001
	92	chain rotation	0.0001	0.0007	0.0003	0.0008	0.0000	0.0032

Table 10.3.: Parameters of electron-phonon (eV) and spin-phonon coupling for the infrared active phonon modes of NaV_2O_5 (frequency ω in cm^{-1}) as obtained from theory.

hopping matrix elements. The largest $\delta E_g/\delta Q$ is found for the V–O3 stretching mode with A_g symmetry, with a corresponding value of 0.092 eV, while a result of 0.090 eV is obtained for the A_g mode with 512 cm^{-1}. Also the phonon modes with $\delta E_g/\delta Q$ values next lower in energy turn out to be A_g modes, i.e. the O3–V–O2 bending modes at 308 cm^{-1} ($\delta E_g/\delta Q = 0.054$) and 232 cm^{-1} ($\delta E_g/\delta Q = 0.033$), respectively. The phonon mode with the highest change in E_g not having A_g symmetry is the B_{2g} V–O3 stretching mode with 979 cm^{-1}, where a corresponding coupling parameter of 0.012 eV is obtained.

The variation of the exchange parameters $\delta J_\parallel/\delta Q$ (along the ladders) and $\delta J_\perp/\delta Q$ (within the rungs) weighted by their ground state values are presented in the last two columns of Tabs. 10.2 and 10.3. Within the exchange parameters parallel to the ladder, the largest spin-phonon coupling ($\delta J_\parallel/J_\parallel = 0.526$ for $\delta Q = 1$) is found for the B_{1g} mode with 661 cm^{-1}, reflecting the large $\delta t_\parallel/\delta Q$ for the same mode. In fact, the two quantities are connected by the relation $J_\parallel = t_\parallel^2/E_{VO}$, as it is discussed in Sect. 5.2. This also explains why the three modes with the next lower values of $\delta J_\parallel/J/\delta Q$ are analogous to their counter-

parts of $\delta t_\parallel/\delta Q$. The corresponding results are 0.294 (A_g mode at 512 cm^{-1}), 0.152 (B_{3g} mode at 262cm^{-1}), and 0.147 (B_{1u} mode at 554 cm^{-1}). This means, however, that the results for the B_{3g} mode at 262 cm^{-1} and the B_{1u} mode at 554 cm^{-1} are swapped compared to the findings for $\delta t_\parallel/\delta Q$.

A similar situation is found for the exchange parameter within the rungs. The largest values for $\delta J_\perp/J/\delta Q$ are found for the A_g O3–V–O2 bending mode with 308 cm^{-1} (0.094) and the A_g V–O2 stretching with a frequency of 512 cm^{-1} (0.077). The same modes are also responsible for the greatest impacts on $t_\perp$, even though in swapped order. With a change of $\delta J_\perp/J = 0.049$ and 0.048 for $Q = 1$, respectively, a strong spin-phonon interaction is also found for the B_{1u} mode at 554 cm^{-1} and the A_g mode at 467 cm^{-1}.

10.2. CaV_2O_5

10.2.1. Hopping parameters, charge transfer gap, Hubbard U

	Theory	References	
		[116, 26]	[117]
$\|t_\parallel\|$	0.143	0.101	0.087
$\|t_\perp\|$	0.321	0.252	0.143
$\|t_i\|$	0.244	0.076	0.029
E_g	2.882	–	–
U	2.45	3.6	–

Table 10.4.: Hopping matrix elements, charge transfer gap, and on-site Hubbard repulsion U (in eV) extracted from the ab initio band structure of CaV_2O_5 compared to literature.

Table 10.4 shows our theoretical hopping parameters, charge transfer gap and Hubbard U compared to the data of Refs. [116] and [26]. In these complementary references, which are written by the same authors, the exchange integrals are obtained as the second derivatives of the ground-state energy with respect to the magnetic moment rotation angle, on the basis of the Green-function method (Refs. [118, 119]). The hopping parameters are extracted from the LDA band structure using a systematic downfolding scheme to obtain an effective few band Hamiltonian reproducing the LDA bands close to the Fermi level. The reported values for $t_\parallel$ and $t_\perp$, 0.101 eV and 0.252 eV, are about 40% lower than the results we obtained ($t_\parallel = 0.143$ eV, $t_\perp = 0.321$ eV), while t_i differs by a factor of three (0.076 eV compared to 0.244 eV in our calculations).

Ref. [117], which presents results from molecular orbital calculations, estimates hopping parameters $t \approx \Delta e/2$ from the energy separations Δe between the bonding and anti-bonding state of spin-dimers, which are formed by the V^{4+} ions on (i) either side of one rung, (ii) on two neighboring rungs of one leg, and (iii) by the nearest neighbors of adjacent ladders. This way, the matrix elements presented in the last column of Tab. 10.4 result. They are still smaller than the ones presented in Refs. [116, 26], thus being decreased by a factor of two ($t_\parallel$ and $t_\perp$) to eight (t_i) with respect to our findings.

Comparing our results for the relaxed structures of CaV_2O_5 and NaV_2O_5, the matrix elements for a hopping along the ladder (0.143 eV) and within the rungs (0.321 eV), respectively, are about 20% lower for the former. In terms of band structure, the reason for this decrease are a smaller gap between the valence and conduction band in CaV_2O_5 on the one hand, and a smaller dispersion of the upper V d_{xy} states in Δ direction, on the other hand. In turn, the parameter for the inter-ladder hopping t_i is more than twice as large in CaV_2O_5, namely 0.244 eV. This finding is connected to a strongly increased splitting of the V d_{xy} states at the Γ point. Moreover it shows, that the inter-ladder interaction is considerably larger in CaV_2O_5 compared to NaV_2O_5. This is also the reason for the smaller inter-ladder distance in the former. It is also important to explain the frequency of the chain rotation mode with A_g symmetry (Sect. 6.1.2). An increase of 12% with respect to NaV_2O_5 also results for the charge transfer gap E_g in CaV_2O_5, where a value of 2.882 eV is obtained. This implies, that the V d_{xy} states and O p_y states are more separated in the calcium compound.

Concerning the on-site Hubbard repulsion U, the method is used where the additional electronic charge is compensated by a uniform positive background. This procedure leads to the same result as for NaV_2O_5, i.e. $U = 2.45$ eV, demonstrating that U is only weakly influenced by the ion's surrounding.

10.2.2. Coupling parameters

Tables 10.5 and 10.6 show the parameters of electron-phonon and spin-phonon coupling for the Raman and infrared-active phonon modes of CaV_2O_5. Comparing the coupling of $t_\parallel$ to lattice distortions corresponding to the different Γ point phonon modes, similarly to NaV_2O_5 the strongest effect is related to the V–O2 stretching modes. Again, the largest value ($\delta t_\parallel/\delta Q = 0.42$) is found for the B_{1g} mode highest in frequency. This vibration is followed by the B_{3g} V–O2 stretching with 605 cm^{-1}, with a $\delta t_\parallel/\delta Q$ of 0.016 eV, while the corresponding parameter is much less significant in the respective mode of NaV_2O_5. In turn, the phonon mode with the next smaller change of $t_\parallel$ coincides which its counterpart in NaV_2O_5 again, i.e. it is the B_{1u} mode second highest in energy. This vibration, which has a frequency of 559 cm^{-1} in CaV_2O_5, exhibits a $\delta t_\parallel/\delta Q$ of 0.013 cm^{-1}. The A_g V–O2 stretching mode with 516 cm^{-1} is a further oscillation which significantly affects the hopping along the ladder, resulting in $\delta t_\parallel/\delta Q = 0.011$ eV

Irrep	ω	Assignment	$\frac{\delta t_\parallel}{\delta Q}$	$\frac{\delta t_\perp}{\delta Q}$	$\frac{\delta t_i}{\delta Q}$	$\frac{\delta E_g}{\delta Q}$	$\frac{\delta J_\parallel/J_\parallel}{\delta Q}$	$\frac{\delta J_\perp/J_\perp}{\delta Q}$
A_g	900	V-O3 stretch.	0.0027	0.0083	0.0078	0.1286	0.0316	0.0470
	516	V-O2 stretch.	0.0107	0.0114	0.0253	0.0503	0.1863	0.0565
	446	V-O1-V bend.	0.0014	0.0248	0.0139	0.0228	0.0052	0.1399
	412	$O1_z$+O3-V-O2 b.	0.0056	0.0094	0.0223	0.0239	0.0815	0.0540
	307	O3-V-O2 bend.	0.0015	0.0016	0.0035	0.0054	0.0141	0.0185
	265	O3-V-O2 bend.	0.0070	0.0049	0.0337	0.0048	0.0895	0.0285
	201	Ca$\parallel$ c	0.0020	0.0038	0.0278	0.0080	0.0269	0.0217
	106	chain rot.	0.0014	0.0060	0.0110	0.0009	0.0227	0.0317
B_{1g}	593	V-O2 stretching	0.0402	0.0028	0.0000	0.0033	0.6006	0.119
	253	O3-V-O2 bending	0.0009	0.0024	0.0008	0.0072	0.0162	0.0434
	136	antiparallel leg-shift	0.0050	0.0033	0.0057	0.0113	0.0505	0.0448
B_{2g}	842	V-O3 stretch.	0.0002	0.0016	0.0012	0.0027	0.0032	0.0102
	652	V-O1 stretch.	0.0003	0.0010	0.0006	0.0031	0.0050	0.0067
	499	O2-V-O1 bend.	0.0002	0.0006	0.0014	0.0003	0.0027	0.0029
	342	O2-V-O3 bend.	0.0002	0.0023	0.0004	0.0044	0.0001	0.0118
	259	O2-V-O3 bend.	0.0016	0.0006	0.0015	0.0012	0.0226	0.0036
	219	Ca-ladder shear	0.0006	0.0014	0.0016	0.0001	0.0071	0.0095
	190	Ca $\parallel$ a + chain rot.	0.0003	0.0019	0.0004	0.0055	0.0084	0.0082
	135	chain rotation	0.0002	0.0005	0.0004	0.0016	0.0052	0.0000
B_{3g}	605	V-O2 stretching	0.0159	0.0003	0.0012	0.0220	0.2104	0.0225
	392	O1-V-O3 bending	0.0015	0.0071	0.0004	0.0038	0.0146	0.0382
	254	rung *vs* O3 shear	0.0092	0.0038	0.0008	0.0060	0.1393	0.0181
	195	(ladder *vs* Ca) $\parallel$ b	0.0034	0.0033	0.0005	0.0026	0.0450	0.0152
	113	antipar. ladder shift	0.0084	0.0047	0.0049	0.0030	0.1338	0.0271

Table 10.5.: Parameters of electron-phonon (eV) and spin-phonon coupling for the Raman active phonon modes of CaV_2O_5 (frequency ω in cm^{-1}) as obtained from theory.

.

Proceeding to the matrix element for hoppings within one rung, the A_g modes appear to have the largest impact, which resembles the situation in NaV_2O_5. The largest value for $\delta t_\perp/\delta Q$ (0.025 eV) is found for the A_g mode with 512 cm^{-1}, which was identified as V–O1–V bending. But also the V–O2 stretching mode with A_g symmetry influences $t_\perp$ noticeably, i.e. $\delta t_\perp/\delta Q = 0.011\ eV$. Furthermore, a considerably coupling of the in-rung hopping to lattice distortions is also detected for the A_g modes at 412 cm^{-1} (0.009 eV) and 900 cm^{-1} (0.008 eV), which represent a O3–V–O2 bending with some $O1_z$ contribution and a V–O3 stretching, respectively. For both, the O1–V–O3 bending modes with B_{2u} sym-

Irrep	ω	Assignment	$\frac{\delta t_\parallel}{\delta Q}$	$\frac{\delta t_\perp}{\delta Q}$	$\frac{\delta t_i}{\delta Q}$	$\frac{\delta E_g}{\delta Q}$	$\frac{\delta J_\parallel/J_\parallel}{\delta Q}$	$\frac{\delta J_\perp/J_\perp}{\delta Q}$
B_{1u}	903	V-O3 stretch.	0.0079	0.0018	0.0013	0.0020	0.1036	0.0032
	559	V-O2 stretch.	0.0131	0.0008	0.0012	0.0015	0.1550	0.0319
	483	O1-V-O2 bend.	0.0081	0.0038	0.0005	0.0005	0.1060	0.0126
	348	O1-V-O2 b. + $O3_x$	0.0064	0.0013	0.0001	0.0020	0.0903	0.0049
	282	rung stretching	0.0041	0.0020	0.0006	0.0004	0.0518	0.0043
	235	O1-V-O3 b.+ Ca ∥ c	0.0006	0.0017	0.0001	0.0059	0.0071	0.0086
	195	Ca ∥ c	0.0021	0.0011	0.0000	0.0008	0.0219	0.0013
B_{2u}	550	V-O2 stretching	0.0004	0.0020	0.0027	0.0108	0.0053	0.0124
	401	O1-V-O3 bending	0.0004	0.0074	0.0001	0.0017	0.0043	0.0454
	229	O3 *vs* ladder shear	0.0005	0.0010	0.0006	0.0052	0.0061	0.0052
	196	Ca ∥ b	0.0003	0.0015	0.0004	0.0017	0.0030	0.0087
B_{3u}	845	V-O3 stretching	0.0003	0.0025	0.0014	0.0077	0.0087	0.0163
	658	O1 ∥ a	0.0004	0.0013	0.0001	0.0054	0.0055	0.0085
	479	O2-V-O1 bend. ∥ a	0.0006	0.0013	0.0001	0.0028	0.0077	0.0077
	367	V-O2 bend. ∥ c	0.0014	0.0017	0.0020	0.0019	0.0170	0.0074
	229	V-O3 bending	0.0007	0.0015	0.0010	0.0098	0.0056	0.0048
	174	Ca ∥ a	0.0002	0.0002	0.0004	0.0008	0.0024	0.0003
	114	chain rotation	0.0003	0.0004	0.0006	0.0007	0.0026	0.0013

Table 10.6.: Parameters of electron-phonon (eV) and spin-phonon coupling for the infrared active phonon modes of CaV_2O_5 (frequency ω in cm^{-1}) as obtained from theory.

metry at 401 cm^{-1} and B_{3g} symmetry at 392 cm^{-1}, coupling parameters of about 0.007 eV are obtained by theory.

The predominance of the A_g modes is even stronger looking at the inter-ladder hopping t_i. While in NaV_2O_5 the highest respective coupling is found for the B_{1g} mode lowest in energy, in CaV_2O_5 this mode plays a rather subordinate role. Instead, the seven Γ point vibrations with the highest values of $\delta t_\perp/\delta Q$ all have A_g symmetry, headed by the O3–V–O2 bending mode at 265 cm^{-1} with a value of 0.033 eV, the Ca ∥ c oscillation at 201 cm^{-1} ($\delta t_\perp/\delta Q = 0.028\ eV$), the V–O2 stretching at 516 cm^{-1} ($\delta t_\perp/\delta Q = 0.025\ eV$), and the O3–V–O2 bending combined with an O1z displacement at 412 cm^{-1} (0.022 eV). This means, that the fully symmetric phonon modes cause the largest change in the splitting of the V d_{xy} states at the Γ point, since t_i is directly proportional to the latter quantity (c.f. Sect. 5.1).

Analyzing the change of the charge transfer gap E_g as a function of phonon displacement Q, the A_g modes one more time show the largest effect. With $\delta E_g/\delta Q = 0.1286\ eV$ a huge electron-phonon coupling is found for the one at

900 cm^{-1} comprising a V–O3 stretching. Actually, this value is 30% higher than its counterpart in NaV_2O_5. The corresponding parameter for the V–O2 stretching mode of CaV_2O_5 with 516 cm^{-1} is already much smaller, namely 0.050 eV, while the next smaller value of $\delta E_g/\delta Q = 0.1286\ eV$ is detected in the 446 cm^{-1} A_g mode (0.024 eV). The large diversity in the electron-phonon coupling in CaV_2O_5 is in some contrast to the situation in NaV_2O_5, where the results for the two modes with the largest $\delta E_g/\delta Q$, the A_g modes with 996 cm^{-1} and 512 cm^{-1}, respectively, differ only very little.

The spin-phonon coupling parameters expressed in terms of relative changes of $J_\parallel$ and $J_\perp$ induced by phonon distortions are presented in the last two columns of Table 10.5 and 10.6, respectively. In CaV_2O_5, the highest values for $\delta J_\parallel/J/\delta Q$ are found for the V–O2 stretching modes with B_{1g} symmetry (0.601), B_{3g} symmetry (0.210), A_g symmetry (0.186) and B_{1u} symmetry (0.155). In fact, the mentioned oscillations are also the ones dominating the electron-phonon coupling of hoppings along the ladder, which seems reasonable due to the interrelation of both quantities (see Sect. 5.1). Besides, V–O2 stretching modes turn out to give also the largest respective parameters in NaV_2O_5, as shown in Sect. 10.1. All other phonon modes lead to changes of $\delta J_\parallel/J$ per δQ smaller than 0.1.

Investigating the change of $J_\perp$, the exchange parameters within one rung, finally, one finds that it is not completely analogous to the change of the in-rung hopping matrix element $t_\perp$. In detail, the largest value for $\delta J_\perp/J/\delta Q$ (0.1340) is encountered in the A_g V–O1–V bending mode with 446 cm^{-1}, which also accounts for the largest $\delta t_\perp/\delta Q$, while another phonon mode strongly affecting $\delta J_\perp$, the B_{3g} V–O2 stretching with 593 cm^{-1}, did not exhibit a big influence on $t_\perp$. Other oscillations strongly altering the in-rung spin exchange include the A_g V–O2 stretching at 516 cm^{-1} ($\delta J_\perp/J/\delta Q = 0.057$) and the A_g O3-V-O2 bending combined with an $O1_z$ movement at 412 cm^{-1} ($\delta J_\perp/J/\delta Q = 0.054$).

11. Low-Temperature Phase of NaV_2O_5

In this chapter, calculations for different candidates of the low-temperature structure of NaV_2O_5 as proposed in literature are presented. Moreover, for both space groups suggested in literature ($Fmm2$ and $A112$) the atomic positions have been relaxed. The theoretical results are compared to experimental data with respect to the EFG. In addition, the stability of the computed phases is discussed in terms of the total energies.

11.1. Electric Field Gradients

In this section, theoretical results for the electric field gradients (EFG) are presented and compared to experimental values obtained from ^{51}V NMR and ^{23}Na NMR, respectively. In order to convert values for quadrupole frequencies into electric field gradients, the relations explained in Sect. 2.5.5 are used.

11.1.1. ^{51}V NMR

Table 11.1 shows EFGs corresponding to NMR results available in literature, while Tab. 11.2 presents the theoretically obtained EFG on the vanadium sites of the relaxed high temperature structure and the low-temperature structures of NaV_2O_5, respectively. In the high-temperature phase, the main component of the EFG (V_{zz} = 4.20 V/m^2) is found parallel to the stacking direction c, while the components parallel to the legs (V_{yy}) and to the rungs(V_{xx}) equal -2.54 V/m^2 and -1.66 V/m^2, respectively, thus implying an η value of 0.21. This is in fairly good agreement with experiment [46, 48], where at T = 100 K $V_{zz} = 6.12$ V/m^2 and $\eta = 0.26$ are obtained. In this context, the difference to theory may partially be due to structure relaxation effects.

Experimentally, in the low-T regime rather few ^{51}V NMR results are available. In detail, only Ref. [47] report explicit values for $V_{\alpha\alpha}$ at T<T$_c$. Two V sites are detected, where at V1 an EFG of V_{zz}= 4.45 V/m^2 and $\eta = 0.48$ is found, while for V2 only one component is presented, namely V_{zz}= 1.89 V/m^2. This findings are in agreement with the ones of Ref. [48], where ^{51}V NMR using a sample of $Na_{0.996}V_2O_5$ was performed. This reference also reports two V sites, where for the first one an EFG of 4.45 V/m^2 with $\eta = 0.5$ is presented, while for V2 no

Experiment						
Ref.	T	Site	V_{zz} ($\parallel c$)	V_{yy} ($\parallel a$)	V_{xx} ($\parallel b$)	η
[46]	100 K	V1	6.12	-3.86	-2.27	0.26
[47]	10 K	V1	4.45	-3.30	-1.16	0.48
		V2	1.89	–	–	–
[48]*	100 K	V1	6.15	-3.81	-2.34	0.24
[48]*	10 K	V1	4.44	-3.33	-1.11	0.5
		V2	–	–	–	–
[49]	30 K	V1	–	–	–	–
		V2	–	–	–	–
		V3	–	–	–	–

Table 11.1.: EFGs for the V sites (in V/m^2) from ^{51}V NMR measurements as reported in literature. The atoms are sorted with respect to the magnitude of V_{zz}. In Ref. [48] (marked with *) a slightly Na deficient sample was used.

explicit results are given. In the third reference [49] the $-\frac{1}{2} \rightarrow -\frac{3}{2}$ transition for V is presented. In contrast to the former results, three independent V sites are reported.

On the theoretical side, depending on the space group (SG) a maximum number of six (SG $Fmm2$) or eight (SG $A112$) independent V sites is possible. In this context it is important to explain that in order to investigate the structure proposed in Ref. [14] the structural data presented in Ref. [13] have been used, but the layers are arranged as proposed in the former reference.

Analyzing the theoretical results, it turns out that not all V sites differ significantly with respect to their EFG. Thus, for the structure taken from Ref. [11] three groups of values for V_{zz} are obtained. The first two sites have a V_{zz} of about 4.4 V/m^2, the second pair of sites (V1b and V21b) shows an EFG of about 4.0 V/m^2, and for V21a and V1a, respectively, $V_{zz} \approx$ 3.7 V/m^2 is obtained. In terms of the asymmetry parameter η, for the first two V sites a similar value (≈ 0.6) is found, while η differs considerably for V1b and V21b (0.39 and 0.14, respectively) as well as for V21a and V1a (0.29 and 0.52, respectively). Relaxing the atomic positions in the same space group, the differences with regard to $V_{\alpha\alpha}$ and η virtually disappear, where for the former a value of about 4.35 V/m^2 and for the latter 0.25 is found for all sites.

The situation is different when relaxing the structure in the monoclinic space group $A112$ (no. 5) proposed by Refs. [13, 14]. In this case, V_{zz} is still very similar for all sites ($V_{zz} \approx 4.20$), but V_{xx} and—consequently—η differ noticeably, yielding two different types of V sites. While η is about 0.35 for V5, V6, V7 and V8, a value of 0.1 is found for the remaining V sites. For the structure taken

Theory					
Structure	Site	V_{zz} ($\parallel c$)	V_{yy} ($\parallel a$)	V_{xx} ($\parallel b$)	η
high T, relaxed	V	4.20	-2.54	-1.66	0.208
Bernert01	V22a	4.44	-3.63	-0.81	0.64
(SG Fmm2)	V22b	4.33	-3.47	-0.86	0.60
	V1b	4.01	-2.79	-1.23	0.39
	V21b	3.97	-2.26	-1.71	0.14
	V21a	3.73	-2.40	-1.33	0.29
	V1a	3.64	-2.76	-0.88	0.52
Fmm2, relaxed	V21a	4.38	-2.75	-1.63	0.26
	V1b	4.38	-2.75	-1.63	0.26
	V1a	4.37	-2.72	-1.65	0.25
	V21b	4.37	-2.73	-1.64	0.25
	V22b	4.36	-2.73	-1.63	0.25
	V22a	4.35	-2.71	-1.64	0.24
Ohwada05	V3	4.81	-3.48	-1.33	0.45
(SG A112)	V4	4.78	-3.47	-1.31	0.45
	V2	3.92	-2.63	-1.29	0.34
	V1	3.92	-2.64	-1.28	0.35
	V8	3.90	-2.75	-1.16	0.41
	V7	3.85	-2.73	-1.12	0.42
	V6	3.54	-1.95	-1.59	0.10
	V5	3.52	-1.95	-1.57	0.11
SG A112, relaxed	V7	4.25	-2.33	-1.92	0.10
	V3	4.25	-2.84	-1.41	0.34
	V4	4.24	-2.83	-1.41	0.34
	V8	4.23	-2.32	-1.91	0.10
	V6	4.21	-2.28	-1.93	0.08
	V5	4.21	-2.27	-1.94	0.08
	V1	4.19	-2.87	-1.32	0.37
	V2	4.19	-2.88	-1.31	0.38

Table 11.2.: Electric Field Gradients (EFG) at the V sites (in V/m^2) for the high temperature structure and several structural variants of the low temperature phase of NaV_2O_5. The V atoms are sorted with respect to the magnitude of V_{zz}.

from Ref. [14] without relaxation, on the other hand, three different V sites can be distinguished. While V3 and V4 have $V_{zz} = 4.8$ V/m^2 and $\eta = 0.45$, for V1 and V2, as well as for V7 and V8, a $V_{zz} \approx 3.90$ V/m^2 and $\eta \approx 0.40$ is obtained.

Finally, also sites V5 and V6 exhibit similar properties in terms of the EFG, both having $V_{zz} \approx 3.50$ V/m^2 and $\eta \approx 0.10$.

In summary, the theoretical results obtained from both the orthonormal structure taken from Ref. [11] and the monoclinic systems (Ref. [14] and the system with relaxed positions) yield *three* distinct V sites in terms of the electric field gradient, thus supporting the findings of Michalak *et al.* presented in Ref. [49].

11.1.2. ^{23}Na NMR

The experimental and theoretical results for the electric field gradients on the Na sites are presented in Tables 11.3 and 11.4, respectively. Compared to ^{51}V NMR, regarding ^{23}Na NMR much more data are found in literature. While values of $V_{\alpha\alpha}$ for the high-temperature phase are found in Refs. [50, 51, 48], Ref. [51] reports detailed ^{23}Na NMR measurements for all sites of the low-temperature structure, while Refs. [48] presents results for V_{yy} and V_{xx} for all Na, and [49] reports at least values for all V_{xx} components. On the theoretical side, the main component of the EFG is found in y direction for all Na sites, while V_{yy} corresponds to the z and V_{xx} to the rung direction.

For the high temperature phase, theory yields $V_{zz} = 0.65$ V/m^2 and $\eta = 0.52$. Thus, the agreement with experiments carried out at room temperature [51, 48], where $V_{zz} = 0.61$ V/m^2 and $\eta = 0.62$ is found, is relatively good. In addition to these measurements at T$\approx$ 290 K, experiments performed on the high temperature structure at T= 50 K are available in Refs. [50, 51, 48]. Latter measurements yield almost the same V_{zz} (0.54 V/m^2) and V_{xx}, but a considerably larger V_{yy}, thus changing η from 0.62 to about 0.70.

In the low-temperature phase, all three available experiments [51, 48, 49] consistently report eight different Na sites, where the ^{23}Na NMR spectra of the last reference, however, could as well be interpreted in a way that there are even ten Na positions. Quantitatively, the full ^{23}Na NMR results presented by Ohama *et al.* in Ref. [51] comprise the main component of the EFG between 0.50 V/m^2 (site H) and 0.60 V/m^2 (site A), while the corresponding values for η range from 0.96 to 0.49, i.e. they decrease with increasing V_{zz}. The large value of η is due to the fact that $|V_{yy}|$ is comparable in magnitude to $|V_{zz}|$ (about 0.45 V/m^2 for all sites), but $|V_{xx}|$ is much smaller, namely between 0.01 V/m^2 on site H and 0.15 V/m^2 on site A. Latter results are also confirmed by the findings of Ref. [48] (presenting V_{yy} and V_{xx}) and Ref. [49] (presenting V_{xx}). In general, the EFGs on the sodium sites are about one order of magnitude smaller than the ones on the vanadium sites.

Concerning the theoretical results, the relaxation using the orthorhombic space group $Fmm2$ again leads to six sites that hardly differ, while the same space group using the atomic position from Ref. [11] and the two calculations with space group $A112$ yield a more differentiated situation. In detail, in the calculation using the data from Ref. [11], Na3 ($V_{zz} = 0.48$ V/m^2, $\eta \approx 0.79$) and Na4 ($V_{zz} = 0.47$ V/m^2,

Experiment						
Ref.	T	Site	V_{zz} ($\parallel b$)	V_{yy} ($\parallel c$)	V_{xx} ($\parallel a$)	η
[50]	50 K	A	0.54	-0.46	-0.08	0.70
[51]	295 K	A	0.51	-0.41	-0.10	0.62
[51]	50 K	A	0.54	-0.46	-0.08	0.71
[51]	10 K	A	0.60	-0.45	-0.15	0.49
		B	0.58	-0.46	-0.12	0.58
		C	0.58	-0.45	-0.13	0.54
		D	0.58	-0.46	-0.14	0.57
		E	0.51	-0.46	-0.05	0.80
		F	0.51	-0.48	-0.03	0.89
		G	0.50	-0.46	-0.04	0.83
		H	0.50	-0.48	-0.01	0.96
[48]*	290 K	A	0.51	-0.42	-0.09	0.63
[48]*	50 K	A	0.54	-0.46	-0.08	0.71
[48]*†	8 K	A	–	-0.48	–	–
$H_0 \parallel c$		B	–	-0.46	–	–
		C	–	-0.45	–	–
[48]*†	8K	A'	–	–	-0.15	–
$H_0 \parallel a$		B'	–	–	-0.13	–
		C'	–	–	-0.12	–
		D'	–	–	-0.11	–
		E'	–	–	-0.05	–
		F'	–	–	-0.04	–
		G'	–	–	-0.03	–
		H'	–	–	-0.01	–
[49]*†	10 K	A	–	–	-0.15	–
		B	–	–	-0.14	–
		C	–	–	-0.11	–
		(C')	–	–	(-0.11)	–
		D	–	–	-0.10	–
		D	–	–	-0.85	–
		F	–	–	-0.52	–
		(F')	–	–	(-0.46)	–
		G	–	–	0.24	–
		H	–	–	0.13	–

Table 11.3.: Electric Field Gradients (EFG) for Na sites (V/m^2) from ^{23}Na NMR measurements as reported in literature. In Ref. [48] (marked with *) a slightly Na deficient sample is used. Data marked by † refer to values that we have extracted from the respective figures.

Theory					
Structure	Site	V_{zz} ($\parallel b$)	V_{yy} ($\parallel c$)	V_{xx} ($\parallel a$)	η
high T, relaxed	Na	0.65	-0.51	-0.16	0.52
Bernert01	Na1	0.64	-0.51	-0.13	0.60
(SG Fmm2)	Na2	0.63	-0.52	-0.11	0.65
	Na3	0.48	-0.43	-0.05	0.79
	Na4	0.47	0.47	0.00	1.00
	Na6	0.54	-0.43	-0.11	0.59
	Na5	0.53	-0.43	-0.11	0.60
Fmm2, relaxed	Na6	0.69	-0.52	-0.17	0.52
	Na3	0.69	-0.52	-0.17	0.52
	Na1	0.69	-0.52	-0.16	0.52
	Na5	0.69	-0.52	-0.16	0.52
	Na4	0.69	-0.52	-0.16	0.53
	Na2	0.69	-0.53	-0.16	0.53
Ohwada05	Na2	0.79	-0.53	-0.27	0.33
(SG A112)	Na1	0.79	-0.51	-0.28	0.28
	Na6	0.76	-0.53	-0.23	0.39
	Na5	0.75	-0.54	-0.21	0.44
	Na8	0.57	-0.42	-0.16	0.45
	Na7	0.56	-0.46	-0.11	0.61
	Na4	0.52	-0.48	-0.04	0.84
	Na3	0.51	-0.44	-0.07	0.71
SG A112, relaxed	Na8	0.70	-0.48	-0.22	0.38
	Na2	0.70	-0.52	-0.18	0.48
	Na7	0.70	-0.51	-0.19	0.45
	Na1	0.69	-0.50	-0.19	0.45
	Na6	0.66	-0.53	-0.14	0.59
	Na5	0.66	-0.55	-0.11	0.66
	Na4	0.66	-0.54	-0.12	0.64
	Na3	0.65	-0.52	-0.13	0.59

Table 11.4.: Electric Field Gradients (EFG) on the Na sites (in V/m^2) for the high temperature structure and several structural variants of the low temperature phase of NaV_2O_5. The V atoms are again sorted with respect to the magnitude of V_{zz}.

$\eta \approx 1.00$) represent individual sites, while the results for Na1 and Na2, and for Na5 and Na6 are quite similar, respectively.

In the calculation using the structure proposed by Ohwada *et al.* (Ref. [14]),

all eight inequivalent Na sites demonstrate quite distinct EFG values. While the magnitudes of V_{zz} are concentrated around 0.76 V/m^2 (Na1, Na2, Na5, and Na6)and 0.55 V/m^2 (Na3, Na4, Na7, and Na8), respectively, the asymmetry parameter η is different for each of the sites, ranging from 0.28 (Na1) to 0.84 (Na4). The situation for the monoclinic unit cell with relaxed positions is comparable. While the results for V_{zz} are even more uniform than in the previous case, V_{yy} (V_{xx}) show more differences comparing the several sites, yielding values of η between 0.38 and 0.64.

In general, the theoretical findings agree with experiment very well in terms of V_{zz} and are also similar regarding the variety of different values for η. While the quantitative agreement is slightly better for the orthorhombic structure with experimental positions, qualitatively the monoclinic calculations using space group $A112$ are closer to experiment regarding the diversity of the asymmetry parameter. Altogether, the experimental findings in combination with theory are in favor of a low-temperature structure with eight different Na sites, which is only compatible with a monoclinic unit cell and space group no. 5.

11.2. Total energies

space group	structure	k mesh	tot. energy (Ry)
Fmm2 (orthorh.)	relaxed, high T	(4 4 4)	-0.6547
	Ref. [11]	(4 4 4)	-0.6260
	relaxed, Fmm2	(6 6 6)	-0.7843
A112 (monoclinic)	Ref. [14]	(4 2 4)	-0.7529
	relaxed, A112	(4 2 4)	-0.7860

Table 11.5.: Relative total energies (Ry) for different variants of the low temperature structure of NaV_2O_5. The energy for the relaxed structure with space group $Fmm2$ was obtained using a $\vec{k}$ mesh of $6 \times 6 \times 6$, which corresponds to the density of $\vec{k}$ points used in the mononclinic case.

In addition to the electric field gradients, also the total energies resulting from the different structural variants can shed some light on the low temperature phase of NaV_2O_5. Table 11.5 shows the relative total energies, i.e. E_{tot} + 39002 Ry, for

- the structure with orthorhombic space group $Fmm2$, but the positions relaxed in the high temperature structure;
- the structure presented in Ref. [11];
- the structure with space group $Fmm2$, but positions relaxed *in this space group*;

- the structure with the monoclinic space group $A112$ (no. 5) as suggested by Ref. [14], i.e. using data about atomic position from Ref. [13], but arranging the x–y layers as described in Ref. [14];
- the *relaxed* structure within the latter space group.

Focusing at the two structures with experimental atomic positions, first, the variant suggested by Ohwada *et al.* [14] is clearly favorable regarding its total energy: The result is by about 100 mRy lower than the one for the structure with orthorhombic space group proposed by Bernert *et al.* [11]. An important point with respect to the latter system is that, when moving the atoms to their high-temperature positions, the energy is lowered. This means, that under normal experimental conditions such a state seems very unprobable. Thus we believe that such a structure can, at most, be realized under extraordinary conditions, such as very fast cooling-down of the sample.

Comparing the total energies of the two systems with relaxed atomic positions, the situation gets more interesting. Shifting the atoms to their energetic minimum, a much larger energy is gained in the orthorhombic structure, such that after relaxation of the forces the energies are very close to each other. Actually, the orthorhombic structure with a $\vec{k}$ mesh of $4 \times 4 \times 4$ has an energy, which is only 1.5 mRy higher than the one of the monoclinic counterpart.

At this point it is important to mention, that in order to draw final conclusions about the most favorable structural configuration an absolute convergence of the calculations would be necessary. While the convergence with repsect to $R \times K_{max}$ can be tested relatively well by convergence checks performed for the high-T structure, such a test for the $\vec{k}$ meshes is more challenging. It depends on factors, which are specific for each calculation, namely the lattice constants and the symmetry operations (related to the space group). The two compared cases, however, differ with respect to both criteria. Thus, in order to achieve a reliable basis for a direct comparison, the number of $\vec{k}$ points would have to be increased until the changes in energy are at lest one order of magnitude smaller than the energy differences investigated. Moreover, a perfect convergence would also include a relaxation with respect to the lattice parameters. This is, however, very difficult, due to the huge number of atoms per unit cell, and—consequently—the immense computer power needed.

Summarizing the theoretical results in terms of EFGs and total energies, the monoclinic system appears to be favored: This is indicated by the slightly lower total energy obtained in this case, and shown with clearer evidence by the EFGs for the Na sites.

Part III.

Appendix

A. Computational details

All calculations were performed with the APW+lo method [78] using the WIEN2k code [120]. The exchange-correlation effects were treated within the generalized gradient approximation (GGA) using the form of Perdew, Burke, and Ernzerhof [73].

The muffin tin radii (R_{MT}) were chosen in such a way that about 0.02 a.u. (0.01 Å) of tolerance were left between the spheres of V and the apical oxygen, in order to account for displacements during the relaxation procedure and in the context of phonon calculations. The values for the R_{MT} of V, O, Na, Ca, and Mg, together with other calculational and convergence parameters, are listed in Table A.1.

The plane wave cut-offs were chosen to be 14 a.u.$^{-1}$ for expanding the density and potentials, and 4.62 a.u.$^{-1}$ for expanding the wave functions. The latter corresponds to an $R_{mt} \times K_{\max}$ value of 6.5 for oxygen and sodium, 6.96 for magnesium, 7.53 for vanadium and 8.35 for calcium. A convergence test with different meshes of $\vec{k}$ points showed that 70 points ($2 \times 7 \times 5$) in the whole Brillouin zone (BZ), corresponding to 12 points in its irreducible wedge (IBZ), are enough to achieve convergence in the self-consistent field (SCF) calculations in NaV_2O_5, CaV_2O_5, and MgV_2O_5. In the calculations of the density of states (DOS), 960 $\vec{k}$ points ($5 \times 16 \times 12$, 144 points in the IBZ) were used, while for the calculation of the optical properties a $\vec{k}$ mesh with 3800 points ($8 \times 25 \times 19$, 520 points in the IBZ) was applied.

The convergence criterion for the SCF calculations was the change in forces between two iterations, with a convergence tolerance of 0.2 mRy/a.u. The integration of the $\vec{k}$ space and the calculation of the Fermi energy in both, the SCF and the DOS case, was done by the modified tetrahedron-method [121].

To obtain the phonon frequencies of NaV_2O_5, CaV_2O_5, and MgV_2O_5, four displacements (two in positive direction and two in negative direction) with respect to all symmetry coordinates of each irreducible representation (see Sect. 2.4) were performed. The amplitudes were chosen in such a way that the resulting forces were between 5 and 20 mRy/a.u. The related displacements were between 0.2 Å (Na (Ca,Mg) in x direction) and 0.0075 Å (O3 in z direction), which turned out to lie in the harmonic regime. The so-obtained forces were used to calculate the dynamical matrix, the eigenvectors and the eigenfrequencies by means of a *Mathematica* program, following the procedure described in Sect. 4.3.

In order to calculate phonon modes with symmetries other than A_g, structures

R_{MT}	V	1.6 a.u.
	O	1.4 a.u.
	Na	1.4 a.u.
	Ca	1.8 a.u.
	Mg	1.5 a.u.
	$\vec{k}$ meshes	
Calculation	no. of points ($k_x \times k_y \times k_z$)	no. of points, IBZ
SCF	$2 \times 7 \times 5$	12
DOS	$5 \times 16 \times 12$	144
Optics	$8 \times 25 \times 19$	512
SCF, phonon displacements:		
B_{1g}, B_{3g}	$4 \times 14 \times 10$	140
B_{2g}	$4 \times 11 \times 14$	152
B_{1u}, B_{2u}, B_{3u}	$4 \times 13 \times 10$	70
NaV_2O_5, low T structures:		
Space group $Fmm2$	$4 \times 4 \times 4$	18
Space group $A112$	$4 \times 2 \times 4$	10
K_{max} (wave functions)		4.64 a.u.$^{-1}$
G_{max} (charge dens. and potential)		14 a.u.$^{-1}$
Convergence tolerance for the forces		0.2 mRy/a.u.

Table A.1.: List of calculational parameters used for the APW+lo calculations. Details are given in the text.

with displaced atoms were created where the symmetry operations are different from those of the ground-state structures. The size of the $\vec{k}$ point meshes had to be increased not only due to the lower symmetry, but also to achieve the above mentioned accuracy. The highest number of $\vec{k}$ points was needed for the calculation of the B_{2g} phonons, with a $\vec{k}$ mesh of $4 \times 11 \times 14$ points (152 in the IBZ), followed by the B_{1g} and B_{3g} structures ($\vec{k}$ mesh $4 \times 14 \times 10$ points, 140 in the IBZ) and the B_{nu} calculations ($4 \times 13 \times 10$ points in the whole BZ, 70 in the IBZ). In case of the low temperature supercells of NaV_2O_5, a $\vec{k}$ mesh of $4 \times 4 \times 4$ points was applied for the structures with space group $Fmm2$ (no.42), and a $4 \times 2 \times 4$ mesh for space group $A112$ (no. 5).

The EFGs have been calculated within the Wien2k package as described in Ref. [122]. The optical properties are calculated in the Random Phase Approximation (see, e.g., Ref. [123]), where details of its implementation into Wien2k can be found in Ref. [124].

Acknowledgments

Many people have accompanied my life and work during my PhD studies, supporting me scientifically or as friends (or in both ways), and it is not possible to mention all of them. Yet, I would like to mention some of them explicitly. I am specially grateful to:

My supervisor Claudia Ambrosch-Draxl: For accompanying me as a scientist, for the nice atmosphere in her group, for her friendliness and for giving me the possibility to work as a physicist.

Eugene Sherman: He was my second supervisor, and very important for me in theoretical affairs and in entering the subject of the vanadium ladders. I thank him for very fruitful discussions, patient explanations, his support in many things, and for treating me as a friend rather than as a student.

Prof. Hans-Gerd Evertz and Prof. Peter Knoll, for interesting scientific discussions and support.

My wife Elisabeth: She continuously encourages me, accompanies me, she is the best friend and the greatest motivation at the same time. And she is the one I love!

My parents, my brothers and sisters: They always supported and encouraged me; I am just glad of them.

Stephan, Kerstin, Asier, Markus, Peter, Flo: They have been my colleagues at the institute, and are an important reason why I have been enjoying going to work almost every day.

Veronika and Herbert, my "family in-law": For the nice days spent in Waldneukirchen and for treating me like a *full* member of their family.

Flo, Flip, Maria, Kathi, Christoph, Pedro, and all my friends — just for being friends, which is invaluable.

Finally, I kindly acknowledge support from the following institutions:

- Fonds zur Förderung der wissenschaftlichen Forschung (FWF),
  Projects P 15520, P 15834, and P 16277, Vienna, Austria
- European Union
  EU Research and Training Network *EXCITING*
  contract no. HPRN-CT-2002-00317, Brussels, Belgium
- Karl-Franzens-University of Graz, Austria
- Österreichische Forschungsgemeinschaft, Vienna, Austria

List of Figures

List of Tables

Bibliography

[1] E. Dagotto, *Science* **309**, 257 (2005).

[2] L. Hozoi, S. Nishimoto, A. Yamasaki1, *Phys. Rev. B* **72**, 195117 (2005).

[3] P. Lemmens, *et al.*, *in: Advances in Solid State Physics (edited by R. Helbig)*, vol. 39 (Vieweg Verlag, Wiesbaden, Germany, 1999). 181.

[4] P. Lemmens, G. Güntherodt, C. Gros, *Phys. Rep.* **375**, 1 (2003).

[5] E. Dagotto, T. M. Rice, *Science* **271**, 618 (1996).

[6] M. Isobe, Y. Ueda, *J. Phys. Soc. Jpn.* **65**, 1178 (1996).

[7] M. Weiden, *et al.*, *Z. Phys. B* **103**, 1 (1997).

[8] M. Hase, I. Terasaki, K. Uchinokura, *Phys. Rev. Lett.* **70**, 3651 (1993).

[9] J. Luedecke, *et al.*, *Phys. Rev. Lett.* **82**, 3633 (1999).

[10] H. Nakao, *et al.*, *Phys. Rev. Lett.* **85**, 4349 (2000).

[11] A. Bernert, T. Chatterji, P. Thalmeier, P. Fulde, *Eur. Phys. J. B* **21**, 535 (2001).

[12] S. v. Smaalen, P. Daniels, L. Palatinus, R. K. Kremer, *Phys. Rev. B* **65**, 060101(R) (2002).

[13] H. Sawa, *et al.*, *J. Phys. Soc. Jpn.* **71**, 385 (2002).

[14] K. Ohwada, Y. Fujiiand, *et al.*, *Phys. Rev. Lett.* **94**, 106401 ((2005).

[15] M. N. Popova, *et al.*, *Phys. Rev. B* **65**, 144303 (2002).

[16] M. Fischer, *et al.*, *Phys. Rev. B* **60**, 7284 (1999).

[17] H. Seo, H. Fukuyama, *J. Phys. Soc. Jpn.* **67**, 2602 (1998).

[18] M. V. Mostovoy, D. I. Khomski, *Solid State Commun.* **113**, 159 (2000).

[19] M. J. Konstantinović, Z. V. Popović, V. N. Vasil'ev, Y. Ueda, V. V. Moshchalkov, *Solid State Commun.* **112**, 397 (1999).

[20] S. Grenier, *et al.*, *Phys. Rev. B* **65**, 180101 (2002).

[21] E. Y. Sherman, M. Fischer, P. Lemmens, P. H. M. van Loosdrecht, G. Güntherodt, *Europhys. Lett.* **48**, 648 (1999).

[22] H. Nojiri, S. Luther, M. Motokawa, M. Isobe, Y. Ueda, *J. Phys. Soc. Jpn.* **69**, 2291 (2000).

[23] C. Presura, D. van der Marel, A. Damascelli, R. K. Kremer, *Phys. Rev. B* **61**, 15762 (2000).

[24] M. Onoda, N. Nishiguchi, *J. Solid State Chem.* **127**, 359 (1996).

[25] H. Iwase, M. Isobe, Y. Ueda, H. Yasuoka, *J. Phys. Soc. Jpn.* **65**, 2397 (1996).

[26] M. A. Korotin, V. I. Nisimov, T. Saha-Dasgupta, I. Dasgupta, *J. Phys.:Cond. Matter* **12**, 113 (2000).

[27] T. Ohama, M. Isobe, Y. Ueda, *J. Phys. Soc. Jpn* **70**, 1801 (2001).

[28] M. Onoda, A. Ohyama, *J. Phys.:Cond. Matter* **10**, 1229 (1998).

[29] P. Millet, *et al.*, *Phys. Rev. B* **57**, 5005 (1998).

[30] M. Isobe, Y. Ueda, K. Takizawa, T. Goto, *J. Phys. Soc. Jpn.* **67**, 755 (1998).

[31] F. Mila, P. Millet, J. Bonvoisin, *Phys. Rev. B* **54**, 11925 (1996).

[32] H. Smolinski, *et al.*, *Phys. Rev. Lett.* **80**, 5164 (1998).

[33] Y. Fujii, *et al.*, *J. Phys. Soc. Jpn.* **66**, 326 (1997).

[34] T. Yosihama, *et al.*, *J. Phys. Soc. Jpn.* **67**, 744 (1998).

[35] B. Grenier, *et al.*, *Phys. Rev. Lett.* **86**, 5966 (2001).

[36] M. N. Popova, A. B. Sushkov, S. A. Golubchik, B. Mavrin, V. N. Denisov, *JETP* **88**, 1186 (1999).

[37] Z. V. Popović, *et al.*, *Solid State Commun.* **110**, 381 (1999).

[38] D. Smirnov, J. Leotin, P. Millet, J. Jegoudez, A. Revcolevschi, *Physica B* **259**, 992 (1999).

[39] Z. V. Popović, *et al.*, *Phys. Rev. B* **65**, 184303 (2002).

[40] A. Damascelli, *et al.*, *Phys. Rev. Lett.* **81**, 918 (1998).

[41] V. C. Long, *et al.*, *Phys. Rev. B 60,* **15**, 721 (1999).

[42] A. Damascelli, C. Presura, D. van der Marel, J. Jegoudez, A. Revcolevschi, *Phys. Rev. B* **61**, 2535 (2000).

[43] M. J. Konstantinović, *et al.*, *Phys. Rev. B* **63**, 121102 (2001).

[44] A. B. Sushkov, J. L. Musfeldt, S. A. Crooker, J. Jegoudez, A. Revcolevschi, *Phys. Rev. B* **63**, 22040 (2001).

[45] M. V. Mostovoy, *Phys. Rev. B* **65**, 064412 (2002).

[46] T. Ohama, H. Yasuoka, M. Isobe, Y. Ueda, *J. Phys. Soc. Jpn.* **66**, 3008 (1997).

[47] T. Ohama, H. Yasuoka, M. Isobe, Y. Ueda, *Phys. Rev. B* **59**, 3299 (1999).

[48] Y. Fagot-Revurat, M. Mehring, R. K. Kremer, *Phys. Rev. Lett.* **84**, 4176 (2000).

[49] R. Michalak, H. Mohammad, M. Dischner, C. Geibel, *Physica B* **312**, 624 (2002).

[50] T. Ohama, M. Isobe, H. Yasuoka, Y. Ueda, *J. Phys. Soc. Jpn.* **66**, 545 (1997).

[51] T. Ohama, *et al.*, *J. Phys. Soc. Jpn.* **69**, 2751 (2000).

[52] M. . Weiden, *et al.*, *Journ. Magn. Magn.Mat* **177**, 743 (1998).

[53] J. Hemberger, *et al.*, *Europhys. Lett.* **42**, 661 (1998).

[54] S. Luther, *et al.*, *J. Phys. Soc. Jpn.* **67**, 3715 (1998).

[55] M. Lohmann, *et al.*, *Phys. Rev. Lett.* **85**, 1742 (2000).

[56] A. N. Vasil'ev, *Phys. Rev. Lett.* **81**, 1949 (1998).

[57] H. G. v. Schnering, *et al.*, *Z. Kristallogr. - New Crystal Structures* **213(2)**, 246 (1998).

[58] A. Meetsma, *et al.*, *Acta Crystallogr. C* **54**, 1558 (1998).

[59] B. Kohler, S. Wilke, M. Scheffler, R. Kouba, C. Ambrosch-Draxl, *Comp. Phys. Commun.* **94**, 31 (1996).

[60] P. M. A. Sherwood, *Vibrational spectroscopy of solids* (Cambridge University Press, London, UK, 1972). ISBN 0-521-08482-2.

[61] J. L. de Boer, A. Meetsma, J. Baas, T. T. M. Palstra, *Phys. Rev. Lett.* **84**, 3962 (2000).

[62] webelements. *http* : *//www.webelements.com/*.

[63] L. H. Thomas, *Proc. Camb. Phil. Soc.* **23**, 542 (1926).

[64] E. Fermi, *Z. Phys.* **48**, 73 (1928).

[65] W. Kohn, *Rev. Mod. Phys.* **71**, 1253 (1998).

[66] P. Hohenberg, W. Kohn, *Phys. Rev.* **136**, B864 (1964).

[67] W. Kohn, *Reprint from Highlights of Condensed- Matter Theory, Soc. Italiana di Fisica* **Course LXXXIX**, 4 (1985).

[68] M. Levy, *Phys. Rev. A* **26**, 1200 (1982).

[69] W. Kohn, L. J. Sham, *Phys. Rev.* **140**, A1133 (1965).

[70] D. Ceperley, B. L. Alder, *Phys. Rev. Lett.* **45**, 566 (1980).

[71] J. Perdew, Y. Wang, *Phys. Rev. B* **45**, 13244 (1992).

[72] J. Perdew, M. Levy, *Phys. Rev. Lett.* **51**, 1884 (1983).

[73] J. P. Perdew, K. Burke, M. Ernzerhof, *Phys. Rev. Lett.* **77**, 3865 (1996).

[74] D. Singh, *Planewaves, Pseudopotentials and the LAPW Method* (Kluwer Academic Publishers, Boston/Dordrecht/London, 1994). ISBN 0–7923–9412–7.

[75] P. R. B. O. K. Anderson, *Phys. Rev. B* **12**, 3060 (1975).

[76] D. Singh, *Physical Review B* **43**, 6388 (1991).

[77] J. C. Slater, *Phys. Rev.* **51**, 846 (1937).

[78] E. Sjöstedt, L. Nordström, D. J. Singh, *Solid State Comm.* **114**, 15 (2000).

[79] M. Born, R. Oppenheimer, *Ann. Physik* **84**, 457 (1927).

[80] M. Born, K. Huang, *Dynamical Theory of Crystal Lattices* (Oxford University Press, Oxford, UK, 1954).

[81] P. Puschnig, First-Principles Investigation of Poly(*para*-phenylene) and its Oligomers: Electronic, Optical and Structural Porperties, Diploma thesis, Universität Graz, Graz (1999).

[82] E. Schachinger, H. Sormann, *Theoretische Festkörperphysik I,II* (Skriptum TU Graz, Graz, Austria, 2003).

[83] M. Cardona, *Light Scattering in Solids II* (Springer, Berlin, Germany, 1981).

[84] ed. J. Tang, S. C. Albrecht, *Raman Spectroscopy*, vol. 2 (Plenum Press, New York, USA, 1970).

[85] W. Hayes, R. Loudon, *Scattering of Light by Crystals* (Wiley, New York, USA, 1978).

[86] P. Knoll, C. Ambrosch-Draxl, *Proceedings of the International Workshop on anharmonic properties of high T_c Super Conductors* p. 220 (1995).

[87] H. Auer, Electronic Properties and Raman Spectra of High-T_c Materials, Ph. D. thesis, Universität Graz, Graz (2001).

[88] C. Ambrosch-Draxl, *et al.*, *Phys. Rev. B* **65**, 064501 (2002).

[89] P. Fulde, *Electron Correlations in Molecules and Solids* (Springer, Berlin, Germany, 2002). Corr. 2^{nd} printing of the 3^{rd} enlarged ed. 1995.

[90] S. A. Golubchik, *et al.*, *J. Phys. Soc. Jpn.* **66**, 4042 (1997).

[91] Z. V. Popović, *et al.*, *J. Phys.: Condens. Matter* **10**, L513 (1998).

[92] W. S. Bacsa, R. Lewandowska, A. Zwickn, P. Millet, *Phys. Rev. B* **61**, R14885 (2000).

[93] M. J. Konstantinović, Z. V. Popovic, M. Isobe, Y. Ueda, *Phys. Rev. B* **61**, 15185 (2000).

[94] Z. V. Popović, *et al.*, *J. Phys.: Condens. Matter* **14**, L583 (2002).

[95] M. J. Konstantinović, Z. V. Popovic, A. N. Vasil'ev, M. Isobe, Y. Ueda, *J. Phys.:Cond. Matter* **11**, 2103 (1999).

[96] Bilbao Crystallographic Server. *http* : *//www.cryst.ehu.es/*.

[97] S. Atzkern, *et al.*, *Phys. Rev. B* **63**, 165113 (2001).

[98] N. Katoh, T. Miyazaki, T. Ohno, *Phys. Rev. B* **59**, R12723 (1999).

[99] H. Wu, Q. Zheng, *Phys. Rev. B* **59**, 15027 (1999).

[100] A. N. Yaresko, V. N. Antonov, H. Eschrig, P. Thalmeier, P. Fulde, *Phys. Rev. B* **62**, 15538 (2000).

[101] Z. V. Popovic, F. R. Vukajlovic, *Phys. Rev. B* **59**, 5333 (1999).

[102] L. F. Mattheiss, *Phys. Rev. B* **49**, 14050 (1994).

[103] R. Valentí, T. Saha-Dasgupta, J. V. Alvarez, H. Požgajčić, C. Gros, *Phys. Rev. Lett.* **86**, 5381 (2001).

[104] M. Cuoco, P. Horsch, F. Mack, *Phys. Rev. B* **60**, R8438 (1999).

[105] C. Presura, D. van der Marel, M. Dischner, C. Geibel, R. K. Kremer, *Phys. Rev. B* **62**, 16522 (2000).

[106] P. Horsch, F. Mack, *Eur. Phys. J. B* **5**, 367 (1998).

[107] K. Kobayashi, T. Mizokawa, A. Fujimori, M. Isobe, Y. Ueda, *Phys. Rev. Lett.* **82**, 803 (1999).

[108] A. Damascelli, *private communication* (2004).

[109] M. J. Konstantinović, *et al.*, *Phys. Status Solidi(b)* **211**, R3 (1999).

[110] M. J. Konstantinović, *et al.*, *Phys. Status Solidi(b)* **215**, 661 (1999).

[111] N. Suaud, M.-B. Lepetit, *Phys. Rev. B* **62**, 402 (2000).

[112] S. Nishimoto, Y. Ohta, *J. Phys. Soc. Jpn.* **67**, 4010 (1998).

[113] W. A. Harrison, *Electronic Structure and Properties of Solids* (W. H. Freeman and Company (San Francisco), New York, USA, 1980).

[114] J. C. Slater, G. F. Koster, *Phys. Rev.* **94**, 1498 (1954).

[115] V. I. Anisimov, O. Gunnarson, *Phys. Rev. B* **43**, 7570 (1991).

[116] M. A. Korotin, I. S. Elfimov, V. I. Anisimov, M. Troyer, D. I. Khomskii, *Phys. Rev. Lett.* **83**, 1387 (1999).

[117] H.-J. Koo, M.-H. Whangbo, *Solid State Commun.* **111**, 353 (1999).

[118] A. I. Liechtenstein, M. I. Katsnelson, V. P. Antropov, V. A. Gubanov, *J. Magn. Magn. Mat.* **67**, 65 (1987).

[119] A. I. Liechtenstein, V. I. Anisimov, J. Zaanen, *Phys. Rev. B* **52**, R5467 (1995).

[120] P. Blaha, K. Schwarz, J. Luitz (1997). [Improved and updated Unix version of the original copyright WIEN code, which was published by P. Blaha, K. Schwarz, P. Sorantin and S. B. Trickey, Comp. Phys. Commun. 59, 399 (1990)].

[121] P. E. Blöchl, O. Jepsen, O. K. Anderson, *Phys. Rev. B* **49**, 16223 (1994).

[122] P. Blaha, K. Schwarz, P. Herzig, *Phys. Rev. Lett.* **52**, 1192 (1985).

[123] F. Wooten, *Optical Properties of Solids* (Academic Press, New York and London, 1972).

[124] R. Abt, Berechnung Optischer Eigenschaften von Hochtemperatursupraleitern in der LAPW-Methode, Ph. D. thesis, Universität Graz, Graz (1997).